Separation and Purification Technology 352 (2025) 128269

Contents lists available at ScienceDirect

Separation and Purification Technology

journal homepage: www.elsevier.com/locate/seppur

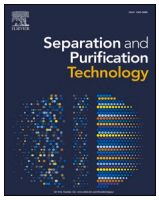

Elucidating the failure of the Ideal Adsorbed Solution Theory for CO_2/H_2O mixture adsorption in CALF-20

Rajamani Krishna *, Jasper M. van Baten

Van 't Hoff Institute for Molecular Sciences University of Amsterdam, Science Park 904, 1098 XH Amsterdam, the Netherlands

ARTICLE INFO

Editor: Z Bao

Keywords:
CO_2 capture
Thermodynamic non-idealities
Segregated adsorption
Hydrogen bonding
Activity coefficients
Transient breakthrough
Fixed bed adsorber

ABSTRACT

The use of CALF-20 for CO_2 capture from humid flue gases has attracted a vast amount of attention from both academia and industry. The focus of this article is on CO_2/H_2O mixture adsorption for which published experimental data demonstrate the severe limitations of the Ideal Adsorbed Solution Theory (IAST) in providing a quantitative estimation of the component loadings. We use Configurational-Bias Monte Carlo (CBMC) simulations for elucidating the origins of thermodynamic non-idealities. The CBMC simulations reveal that two distinct regimes prevail during mixture adsorption. For low relative humidities less than say 20 %, the CO_2 loadings in the adsorbed phase is significantly higher than anticipated by the IAST. CBMC simulations of intermolecular distances for guest pairs reveal that failure of the IAST can be traced to the phenomenon of segregated adsorption. The H_2O-H_2O pairs are close together at typical distances of about 3 Å. The CO_2-H_2O pairs are typically 8 Å apart, occupying adjacent adsorption sites corresponding to the O atoms of the oxalate group. This implies that the CO_2 molecules face a less severe competitive adsorption with H_2O than is anticipated by the IAST, whose applicability mandates a uniform and homogeneous distribution of adsorbates in pore space. The situation changes dramatically at high values of relative humidities, typically larger than about 50 %; in this scenario, the adsorbed phase is significantly richer in H_2O. The CO_2 molecules are compelled to share same adsorption site with pairs of H_2O molecules that are hydrogen-bonded with each other. Consequently, the competition faced by CO_2 is significantly higher than anticipated by the IAST, resulting in significantly lower CO_2 uptakes.

The important message that emerges from this investigation is the need to incorporate the Real Adsorbed Solution Theory (RAST) for quantitative modelling of fixed-bed adsorbers in CO_2 capture with CALF-20.

1. Introduction

In current industrial practice, amine absorption technologies, that are energy intensive, are used for capture of CO_2 from a variety of gaseous mixtures. Potential reduction in the energy consumption is achievable by adsorption separations using fixed-bed adsorption devices [1–7]. For post-combustion CO_2 capture, 13X zeolite is considered to be the benchmark adsorbent, with the ability to meet the U.S. Department of Energy (US-DOE) targets for CO_2 purity and recovery [2].

Following the publication of Lin et al.[8], demonstrating the efficacy of Zinc-based Calgary Framework 20 (CALF-20) for CO_2 capture from humid flue gases, a number of complementary publications have explored a number of related and ancillary aspects [9–17]. Two publications [13,14] have presented comparisons of the experimental data on CO_2/H_2O mixture adsorption with the estimations of the Ideal Adsorbed Solution Theory (IAST). To set the scene, and define the objectives of this article, Fig. 1a presents the experimental data on component loadings for CO_2(1)/H_2O(2) mixture adsorption in structured CALF-20 (80 % MOF:20 % polysulfone) at 295 K; these data have been backed-out from

* Corresponding author.
E-mail address: r.krishna@uva.nl (R. Krishna).

https://doi.org/10.1016/j.seppur.2024.128269
Received 14 April 2024; Received in revised form 23 May 2024; Accepted 2 June 2024
Available online 4 June 2024

Nomenclature

Latin alphabet

A	surface area per kg of framework, $m^2\ kg^{-1}$
c_i	molar concentration of species i, mol m^{-3}
c_{i0}	molar concentration of species i in fluid mixture at inlet to adsorber, mol m^{-3}
C	constant used in Eq. (7), kg mol^{-1}
f_i	partial fugacity of species i, Pa
L	length of packed bed adsorber, m
p_2^{sat}	saturation vapor pressure of water, Pa
P_i^0	sorption pressure, Pa
q_i	component molar loading of species i, mol kg^{-1}
$q_{sat,mix}$	saturation capacity of mixture, mol kg^{-1}
R	gas constant, 8.314 J mol^{-1} K^{-1}
$\%RH$	% relative humidity, dimensionless
t	time, s
T	absolute temperature, K
v	interstitial gas velocity in packed bed, m/s
x_i	mole fraction of species i in adsorbed phase, dimensionless
y_i	mole fraction of species i in the bulk gas mixture, dimensionless

Greek alphabet

γ_i	activity coefficient of component i in adsorbed phase, dimensionless
Λ_{ij}	Wilson parameters, dimensionless
θ	fractional pore occupancy, dimensionless
π	spreading pressure, N m
τ	dimensionless time $\tau \equiv vt/L$, dimensionless
Φ	surface potential, mol kg^{-1}

transient breakthrough experiments [8,12,13]. The dashed lines in Fig. 1a are estimations based on the Ideal Adsorbed Solution Theory (IAST) of Myers and Prausnitz [18]. The IAST estimates are in poor agreement with the experimental data. For $0 < \%RH < 40$, it is noteworthy that the H_2O loadings in the $CO_2(1)/H_2O(2)$ mixture are lower than both the unary H_2O loadings (indicated by solid blue line) and IAST estimates, prompting Lin et al.[8] to postulate the "suppression" of water sorption by CO_2.

Another way to demonstrate the non-idealities is to plot the mole fraction of CO_2 in the adsorbed phase mixture, x_1, as a function of the relative humidity; see Fig. 1b. We note that for $\%RH < 40; x_1 > 0.5$, the adsorbed phase mixture is richer in CO_2, i.e. significantly poorer in H_2O, than is anticipated by the IAST. On the other hand, for $\%RH > 40; x_1 < 0.5$, the adsorbed phase mixture is poorer in CO_2, i.e. richer in H_2O, than is anticipated by the IAST. None of the publications on CALF-20 have underscored the two different scenarios for failure of the IAST, nor offered any explanation for the possible reasons for its failure.

The IAST description of mixture adsorption equilibrium relies on a number of basic tenets [19–25]: (a) homogeneous distribution of guest adsorbates, (b) no preferential locations of any guest species within the pore landscape, and (c) adsorption enthalpies and surface areas of the adsorbed molecules do not change upon mixing with other guests. The occurrence of molecular clustering and hydrogen bonding should be expected to invalidate tenet (c) because the surface area occupied by a molecular cluster is different from that of each of the un-clustered guest molecules in the adsorbed phase. In a number of publications on CO_2 capture from mixtures containing N_2, CH_4, C_2H_4, C_2H_6, C_3H_8, and H_2O using cation-exchanged zeolites [2,19,21,23–29], the IAST has been shown to fail due to non-compliance with one or more of the aforementioned tenets.

The primary objective of this article is to elucidate the reasons for the distinct failure of the IAST, as evidenced in Fig. 1 for $CO_2(1)/H_2O(2)$ mixture adsorption in structured CALF-20.

Towards this end, Configurational-Bias Monte Carlo (CBMC) simulations for adsorption of CO_2/H_2O mixture adsorption in pristine CALF-20 crystals were undertaken. The simulation methodologies are the same as detailed in earlier publications [30–36]. The CALF-20 structure was considered to be rigid in the simulations. Recent works have included considerations of framework flexibility [16] and polymorphism [17]; both these aspects are ignored in the present work. The unit cell dimensions of CALF-20 crystals are $a = 8.9138$ Å; $b = 9.6935$ Å; $c = 9.4836$ Å with angles $\alpha = 90°$; $\beta = 115.895°$; $\gamma = 90°$; see pore landscape in Figure S3. The simulation box for conducting CBMC simulations consisted of $5 \times 3 \times 5 = 75$ unit cells. The interactions between adsorbed molecules are described with Lennard-Jones terms together with electrostatic interactions. For the atoms in the host metal organic framework (see Figure S4), the generic DREIDING [37] force fields were used. The framework atomic charges are from Gopalsamy et al.[9]; see Tables S2 and S3. CO_2 was described by a 3-site charged Lennard-Jones model as described by Garcia-Sánchez et al.[38]. Water is modeled using the four-site TIP4P-Ew potential [39]; TIP4P = 4-site transferable intermolecular potential (TIP4P) and Ew = Ewald technique. Further simulation details are provided in the Supplementary Material.

2. CBMC simulations

Fig. 2a presents the CBMC simulations conducted in this work for unary isotherms for $CO_2(1)$ and $H_2O(2)$ at 298 K. Fig. 2b shows CBMC simulations of component loadings, q_i, for $CO_2(1)/H_2O(2)$ mixture adsorption in CALF-20 at 298 K at a total fugacity = 15 kPa. The mole fraction of H_2O in the bulk gas mixture, y_2, is varied. In Fig. 2b, the loadings are plotted against $\%RH = \frac{f_2}{p_2^{sat}} \times 100$ where f_2 is the partial fugacity of water in the bulk gas phase, and p_2^{sat} is the saturation vapor pressure of water. At 298 K, p_2^{sat} is determined from the Antoine equation: $p_2^{sat} = 3150$ Pa. The dashed lines are the IAST estimations using the dual-site Langmuir-Freundlich model fits of the unary isotherms in Fig. 2a; the fit parameters as specified in Table S4. We note that the CO_2/H_2O binary mixture adsorption exhibits significant departures from thermodynamic idealities. For $\%RH < 25\%$, it is noteworthy is that the H_2O loading for mixture adsorption are lower than the corresponding IAST estimates, prompting Lin et al.[8] to postulate "suppression" of H_2O sorption by CO_2.

Another way to demonstrate the non-idealities is to plot the mole fraction of CO_2 in the adsorbed phase mixture, x_1, defined by

$$x_1 = \frac{q_i}{q_1 + q_2}; \quad x_2 = (1 - x_1) \tag{1}$$

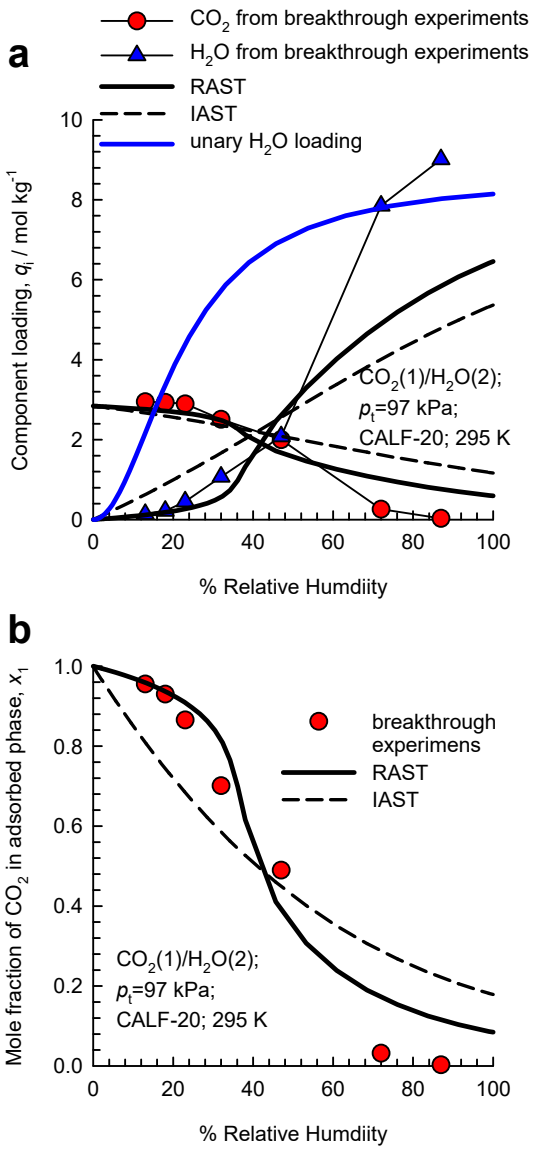

Fig. 1. (a) Experimental data of Lin et al.[8] (indicated by symbols) on component loadings for $CO_2(1)/H_2O(2)$ mixture adsorption in structured CALF-20 (80 % MOF:20 % polysulfone) at 295 K. The total pressure in the bulk gas phase is 97 kPa. In (a) the loadings are plotted against % relative humidity. (b) Plot of the mole fraction of CO_2 in the adsorbed phase mixture, x_1, as a function of the % relative humidity. The unary isotherm fits are provided in Table S1. The dashed and continuous lines are the IAST and RAST estimations, respectively. All calculation details, and input data are provided in the Supplementary Material accompanying this publication.

as a function of the relative humidity (Fig. 2c) and the mole fraction of H_2O in the bulk gas mixture (Fig. 2d). We also note that for $\%RH < 25\%$; $y_2 < 0.05$; $x_1 > 0.3$, the adsorbed phase mixture is richer in CO_2, i.e. poorer in H_2O, than is anticipated by the IAST. On the other hand, for $\%RH > 25\%$; $y_2 > 0.05$; $x_1 < 0.3$, the adsorbed phase mixture is poorer in CO_2 than is anticipated by the IAST. These two scenarios are precisely analogous to those witnessed in the experiments with the structured CALF-20 composite in Fig. 1b.

Additionally, CBMC simulations of component loadings, q_i, for $CO_2(1)/H_2O(2)$ mixture adsorption in CALF-20 at 298 K were determined for varying total fugacity f_t, maintaining the mole fraction of H_2O in the bulk gas mixture at a constant value $y_2 = f_2/f_t = 0.05$; see Fig. 3a. The dashed lines are the IAST estimations. Fig. 3b plots the mole fraction of CO_2 in the adsorbed phase mixture, x_1, as a function of $\%RH$. We again note that for this set of CBMC simulations, two different scenarios hold. For $\%RH < 10\%$; $x_1 > 0.5$, the adsorbed phase mixture is richer in CO_2 than is anticipated by the IAST. On the other hand, for $\%RH > 10\%$ $x_1 < 0.5$, the adsorbed phase mixture is poorer in CO_2, i.e. richer in H_2O, than is anticipated by the IAST.

To investigate the possibility of non-homogeneous distribution of adsorbate guests, CBMC simulation data on the spatial locations of the guest molecules were sampled to determine the inter-molecular distances; these distances are determined from the center of gravity of each guest molecule. By sampling a total of 10^6 simulation steps, the radial distribution function (RDF) were determined for CO_2-CO_2, CO_2-H_2O, and H_2O-H_2O separation distances. Fig. 4a,b presents the RDF data for guest pairs determined from CBMC simulations for $CO_2(1)/H_2O(2)$ mixture adsorption in CALF-20 at 298 K. The total fugacity in the bulk gas phase is 15 kPa with $y_2 = 0.04$; these conditions correspond to the first scenario in Fig. 2c,d: $\%RH < 25\%$; $y_2 < 0.05$; $x_1 > 0.3$. If we compare the first peaks, it is noteworthy that H_2O-H_2O pairs are close together at typical distances of about 3 Å. The CO_2-CO_2 pairs are typically 6.5 Å apart, occupying adjacent adsorption sites of CALF-20; these preferred sites correspond to the O atoms of the oxalate group; see also Figures S4 and S8. The CO_2-H_2O pairs are typically 8 Å apart, occupying adjacent adsorption sites. This implies that the CO_2 molecules face a less severe competitive adsorption with H_2O than is anticipated by the IAST. The segregated nature of adsorbate locations are visually observed in the computational snapshots in Fig. 4 and Figure S9. This explains the finding in Fig. 2c,d that for $y_2 < 0.05$, the adsorbed phase mixture is richer in CO_2 than is anticipated by the IAST; this is a direct consequence of the fact that CO_2 faces negligible competition with partner H_2O molecules.

Fig. 5a presents the data on RDF for center-to-center distances of CO_2-H_2O, and H_2O-H_2O pairs determined from CBMC simulations for adsorption of $CO_2(1)/H_2O(2)$ mixture adsorption in CALF-20 at 298 K; the total fugacity in the bulk gas phase is 15 kPa with $y_2 = 0.06$; these conditions correspond to the second scenario in Fig. 2c,d: $\%RH > 25\%$; $y_2 > 0.05$; $x_1 < 0.3$.We note that the first peaks for both CO_2-H_2O, and H_2O-H_2O pairs occurs at distances of about 3 Å. This implies that CO_2 faces stiffer competitive adsorption with partner H_2O molecules because of the preponderance of H_2O within the framework. Fig. 5b presents the data on RDF for O···H distances of CO_2-H_2O, and H_2O-H_2O pairs; strong hydrogen bonding manifests for H_2O-H_2O pairs. We note the first peak in the RDFs for H_2O-H_2O pairs occurs at a distance that is slightly less than 2 Å, that is characteristic of hydrogen bonding [40,41]. The computational snapshots in Fig. 5 and Figure S10 show that one CO_2 molecule is surrounded by two neighboring H_2O molecules that are hydrogen-bonded to each other. This implies that CO_2 faces enhanced competition with partner H_2O molecules that are H-bonded; such enhanced competition is not anticipated by the IAST that does not cater for formation of H-bonded molecular clusters.

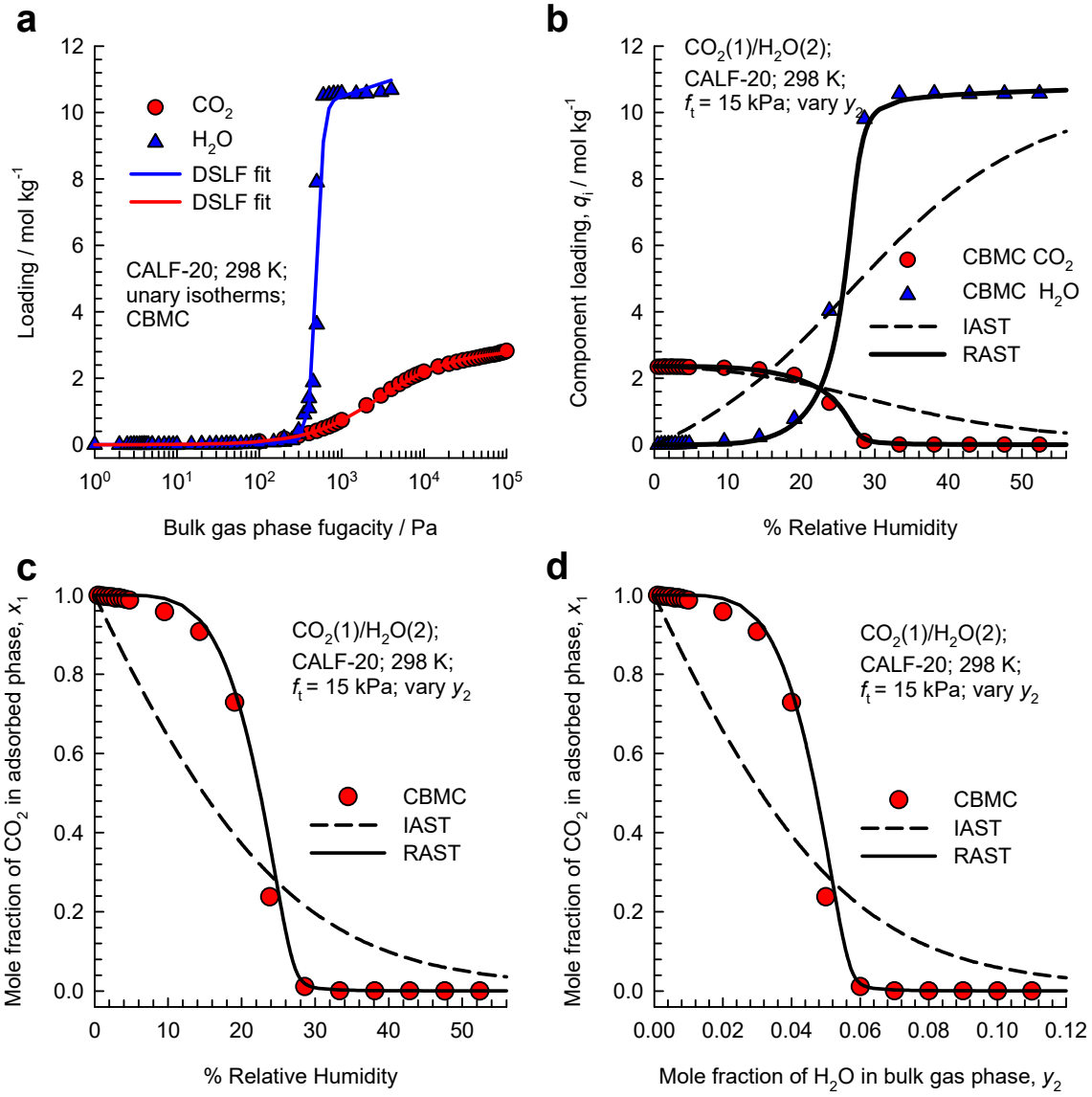

Fig. 2. (a) CBMC simulations for unary isotherms at 298 K, along with Dual-site Langmuir-Freundlich (DSLF) fits whose parameter values are provided in Table S4. (b) CBMC simulations of component loadings, q_i, for $CO_2(1)/H_2O(2)$ mixture adsorption in CALF-20 at 298 K at a total fugacity $f_t = 15$ kPa, plotted as a function of $\%RH = \frac{f_2}{p_2^{sat}} \times 100$. The mole fraction of H_2O in the bulk gas mixture, $y_2 = f_2/f_t$, is varied. (c, d) Plot of the mole fraction of CO_2 in the adsorbed phase mixture, x_1, as a function of (c) $\%RH$, and (d) the mole fraction of H_2O in the bulk gas mixture. The dashed and continuous lines are the IAST and RAST estimations, respectively. All calculation details, and input data are provided in the Supplementary Material accompanying this publication.

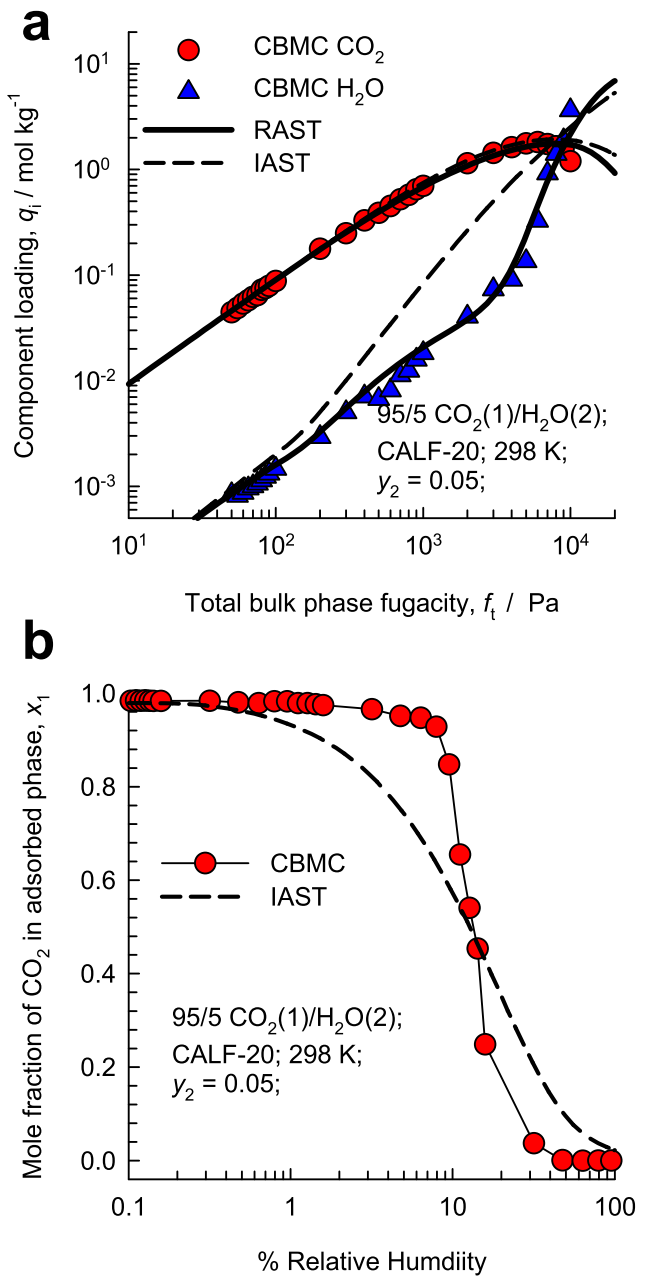

Fig. 3. (a) CBMC simulations of component loadings, q_i, for $CO_2(1)/H_2O(2)$ mixture adsorption in CALF-20 at 298 K with varying total fugacity f_t, maintaining the mole fraction of H_2O in the bulk gas mixture at a constant value $y_2 = f_2/f_t = 0.05$. (b) Plot of the mole fraction of CO_2 in the adsorbed phase mixture, x_1, as a function of $\%RH$. The dashed and continuous lines are the IAST and RAST estimations, respectively. All calculation details, and input data are provided in the Supplementary Material accompanying this publication.

3. The RAST for mixture adsorption equilibrium

For quantifying deviations from the IAST, we need to introduce activity coefficients [18,20,21,42–44]

$$f_i = P_i^0 \gamma_i x_i; \quad i = 1, 2 \tag{2}$$

In eq (2), P_i^0 is the pressure for sorption of component i, which yields the same spreading pressure, π for each of the pure components, as that for the n-component mixture:

$$\frac{\pi A}{RT} \equiv \Phi = \int_0^{P_1^0} \frac{q_1^0(f)}{f} df = \int_0^{P_2^0} \frac{q_2^0(f)}{f} df \tag{3}$$

In eq (3), $q_i^0(f)$ is the *pure* component adsorption isotherm. The quantity A is the surface area per kg of framework, with units of m^2 per kg of the framework of the crystalline material; since the surface area A is not directly accessible from experimental data, the surface potential $\pi A/RT \equiv \Phi$, with the units mol kg^{-1}, serves as a convenient and practical proxy for the spreading pressure π [42,44–46].

The surface potential Φ is a measure of the pore occupancy. As derived in detail in Chapter 1 of the Supplementary Material, the fractional pore occupancy, θ, is related to the surface potential by

$$\theta = 1 - \exp\left(-\frac{\Phi}{q_{sat,mix}}\right) \tag{4}$$

where $q_{sat,mix}$ is the saturation capacity for mixture adsorption. Eq (4) implies that Φ may also be interpreted as a proxy for the pore occupancy. For values of Φ larger than about 30, the pores are nearly saturated, i.e. $\theta \approx 1$.

From the CBMC simulations of mixture adsorption, the activity coefficients in the adsorbed phase, can be calculated as detailed in Section 4.3 of the Supplementary Material. For the two sets of CBMC simulation data (presented in Fig. 2 and Fig. 3), the corresponding activity coefficients are plotted in Fig. 6a,b. Fig. 6a plots the activity coefficients as a function of the mole fraction of CO_2 in the adsorbed phase, x_1. The limiting values are

$$\gamma_i \to 1; \quad x_i \to 1 \tag{5}$$

Fig. 6b shows that the activity coefficients are also dependent on the surface potential, and must conform to the limiting behavior that both activity coefficients tend to unity at vanishingly small values of surface potential Φ

$$\Phi \to 0; \quad \gamma_1 \to 1; \quad \gamma_2 \to 1 \tag{6}$$

In view of Eq. (4), we may interpret Eq. (6) as requiring non-idealities to be of negligible importance at vanish pore occupancies, $\theta \to 0$. Models such as those of Wilson, Margules, and NRTL may be used for quantifying the dependence of the activity coefficients on the composition of the adsorbed mixture and the pore occupancy θ.

The continuous solid lines in Fig. 6 are calculations using the Wilson model

$$\begin{aligned} \ln(\gamma_1) &= \left(1 - \ln(x_1\Lambda_{11} + x_2\Lambda_{12}) - \frac{x_1\Lambda_{11}}{x_1\Lambda_{11} + x_2\Lambda_{12}} - \frac{x_2\Lambda_{21}}{x_2 + x_1\Lambda_{21}}\right)(1 - \exp(-C\Phi)) \\ \ln(\gamma_2) &= \left(1 - \ln(x_1\Lambda_{21} + x_2\Lambda_{22}) - \frac{x_1\Lambda_{12}}{x_1\Lambda_{11} + x_2\Lambda_{12}} - \frac{x_2\Lambda_{22}}{x_1\Lambda_{21} + x_2\Lambda_{22}}\right)(1 - \exp(-C\Phi)) \end{aligned} \tag{7}$$

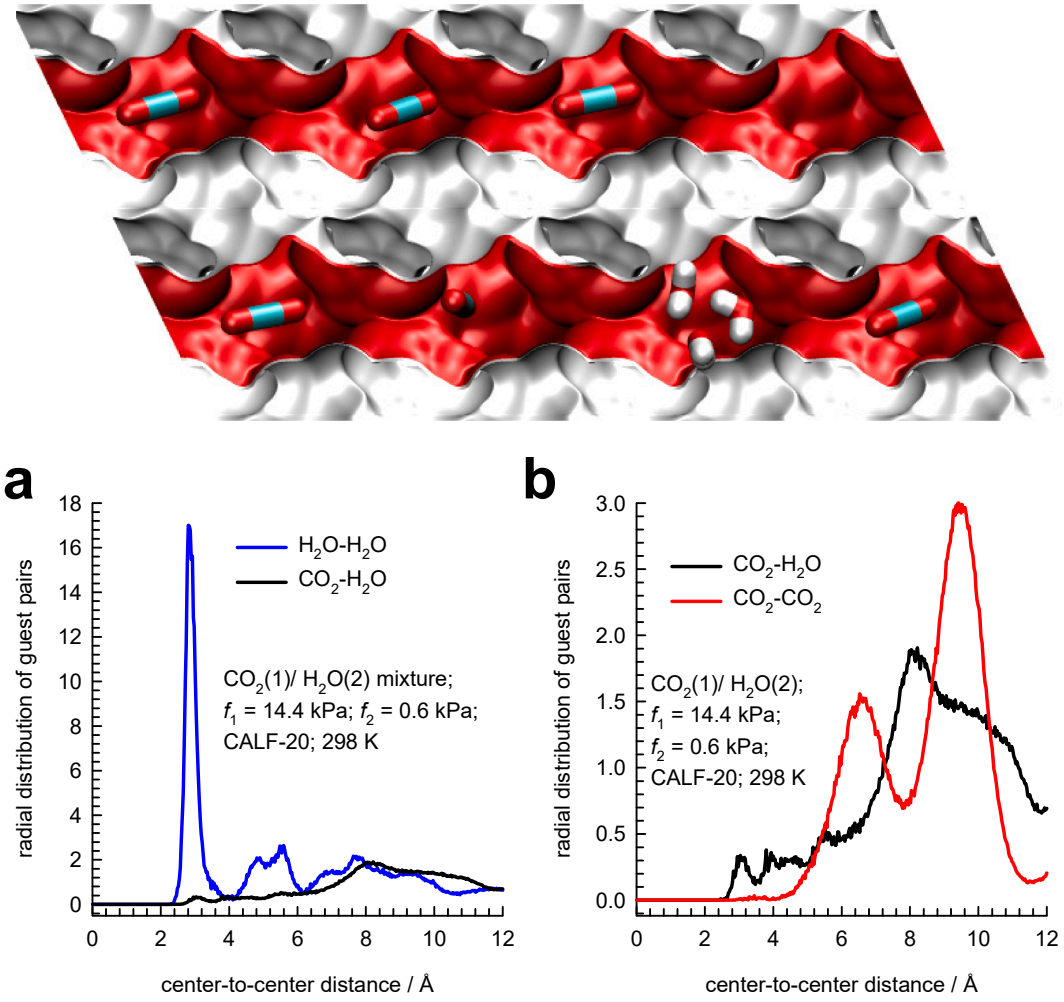

Fig. 4. (a, b) Radial Distribution Function (RDF) of center-to-center distances of CO_2-CO_2, CO_2-H_2O, and H_2O-H_2O pairs determined from CBMC simulations for adsorption of $CO_2(1)/H_2O(2)$ mixture adsorption in CALF-20 at 298 K. The total fugacity in the bulk gas phase is 15 kPa with partial fugacities $f_1 = 14.4$ kPa, and $f_2 = 0.6$ kPa. The plotted RDF data has been normalized such that the area under each of the curves is identical to one another.

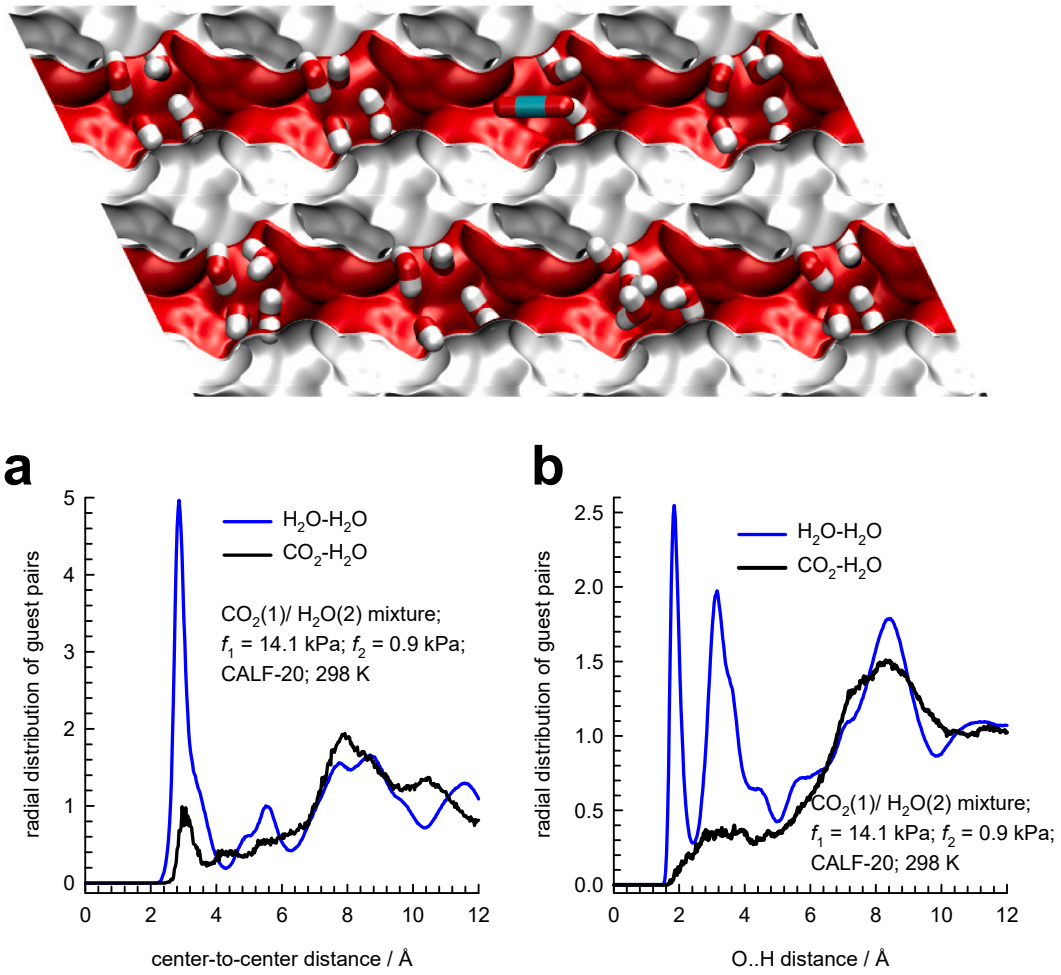

Fig. 5. Radial Distribution Function (RDF) of (a) center-to-center distances, and (b) O···H of CO_2-H_2O, and H_2O-H_2O pairs determined from CBMC simulations for adsorption of CO_2(1)/H_2O(2) mixture adsorption in CALF-20 at 298 K. The total fugacity in the bulk gas phase is 15 kPa with partial fugacities f_1 = 14.1 kPa, and f_2 = 0.9 kPa. The plotted RDF data has been normalized such that the area under each of the curves is identical to one another.

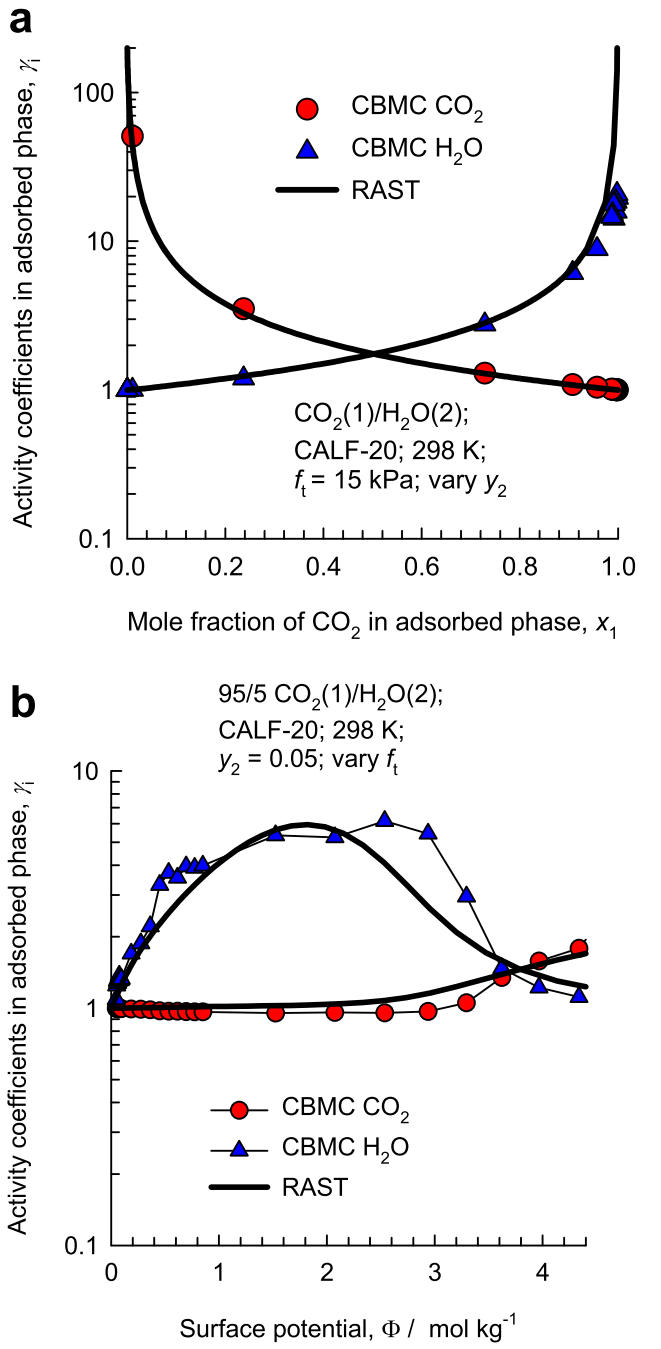

Fig. 6. (a) For the CBMC campaign in Fig. 2, plot of the activity coefficients in the adsorbed phase mixture, γ_i, as a function of the mole fraction of CO_2 in the adsorbed phase mixture, x_1, (b) For the CBMC campaign in Fig. 3, plot of the activity coefficients in the adsorbed phase mixture, γ_i, as a function of the surface potential Φ. The continuous solid lines are the RAST calculations; all calculation details, and input data are provided in the Supplementary Material accompanying this publication.

where in the values of the fitted Wilson parameters C; Λ_{12}; Λ_{21} are tabulated in Table S4. The inclusion of the correction factor $(1-\exp(-C\Phi))$ imparts the correct limiting behaviors for the activity coefficients in the Henry regime, as demanded by Eq. (6). We note, in passing, that this correction factor is often ignored in the RAST implementations in some published works [14,47–49]. The RAST calculations of the component loadings for the two sets of CBMC campaigns are indicated by the continuous solid lines in Fig. 2 and Fig. 3.

The RAST calculations for the component loadings for CO_2/H_2O mixture adsorption in structured CALF-20, determined from breakthrough experiments, are indicated by the continuous solid lines in Fig. 1a,b. For %RH = 73 %, and 87 %, the experimental H_2O loadings for mixture adsorption are in excess of the unary loadings; this characteristic cannot be modeled using the RAST. Noteworthily, RAST implementations of Kaur and Marshall [14], using either the NRTL or Margules models also experience similar limitations at the two highest values of %RH.

4. Transient breakthroughs in fixed-bed adsorber

Nguyen et al.[12] have presented experimental data on the influence of %RH on transient $CO_2(1)/H_2O(2)$ mixture breakthroughs in a laboratory scale fixed bed packed with structured CALF-20. We undertake modeling of these experiments using the simulation methodology as described in earlier works [4,50–52]. Fig. 7 compares breakthrough simulations using RAST (continuous colored lines) and IAST (dashed lines) for CO_2/H_2O mixtures with seven different values of %RH; the dimensionless concentrations, c_i/c_{i0} are plotted as function of the dimensionless time, $\tau \equiv vt/L$ where v is the interstitial gas velocity, and L is the length of the packed bed. Even a visual inspection reveals that there are two scenarios prevalent: (i) 32 % > %RH > 13 %, and (ii) 87 % > %RH > 32 %, corresponding to the two distinct scenarios as also underscored earlier in relation to Fig. 1b.

Fig. 8a,b present calculations of mole fraction of CO_2, and %RH of the gas mixture exiting the fixed bed determined from the breakthrough simulations with the RAST implementation. The comparisons with the corresponding experimental data presented in Figure 9a,b of Nguyen et al. [12] are provided in Figure S18. The agreement between simulations and experiment is good for %RH = 13, 18, 23, 32, 47. For %RH = 73 and 87, the agreement is poorer because at these high humidity values, the RAST fails to match equilibrated uptakes and adsorbed compositions; cf. Fig. 1a,b. In particular, the experimental H_2O uptakes for mixtures exceeds the unary uptake; this phenomenon cannot be modeled using the RAST.

The comparisons with the corresponding experimental data presented in Figure 9a,b of Nguyen et al. [12] are provided in Figure S18. The agreement between simulations and experiment is good for %RH = 13, 18, 23, 32, 47. For %RH = 73 and 87, the agreement is poorer because at these high humidity values, the RAST fails to match equilibrated uptakes and adsorbed compositions; cf. Fig. 1a,b. In particular, the experimental H_2O uptakes for mixtures exceeds the unary uptake; this phenomenon cannot be modeled using the RAST.

Fig. 8c,d present the corresponding calculations of mole fraction of CO_2, and %RH of the gas mixture exiting the fixed bed determined from the breakthrough simulations with the IAST implementation. Even a visual inspection of the IAST simulation results will lead us to conclude that these simulations do not reflect the experimental breakthroughs even in a qualitative manner.

5. Conclusions

Published experimental data [8,13] on $CO_2(1/H_2O(2)$ mixture adsorption in CALF-20 reveal strong thermodynamic non-idealities. The deviations from the IAST estimations follow two different scenarios, depending on the values of %RH. For low %RH values, the CO_2 adsorption is significantly stronger than anticipated by the IAST. For high %RH values, the CO_2 loadings in the adsorbed phase are significantly lower than anticipated by the IAST. CBMC simulations of $CO_2(1/H_2O(2)$ mixture adsorption in CALF-20 are used to elucidate the origins of thermodynamic non-idealities for these two different scenarios. Radial Distribution Functions (RDFs) of intermolecular distances of CO_2-CO_2, H_2O-H_2O, and CO_2-H_2O pairs reveal that failure of the IAST can be traced to the phenomenon of segregated adsorption prevails at low values of %RH. CO_2 locates at sites that are distant from H_2O; consequently, CO_2 faces less severe competition from H_2O than anticipated by the IAST, that mandates a homogeneous distribution of adsorbates within CALF-20 pores. For high values of %RH, the CO_2 molecules are compelled to share same

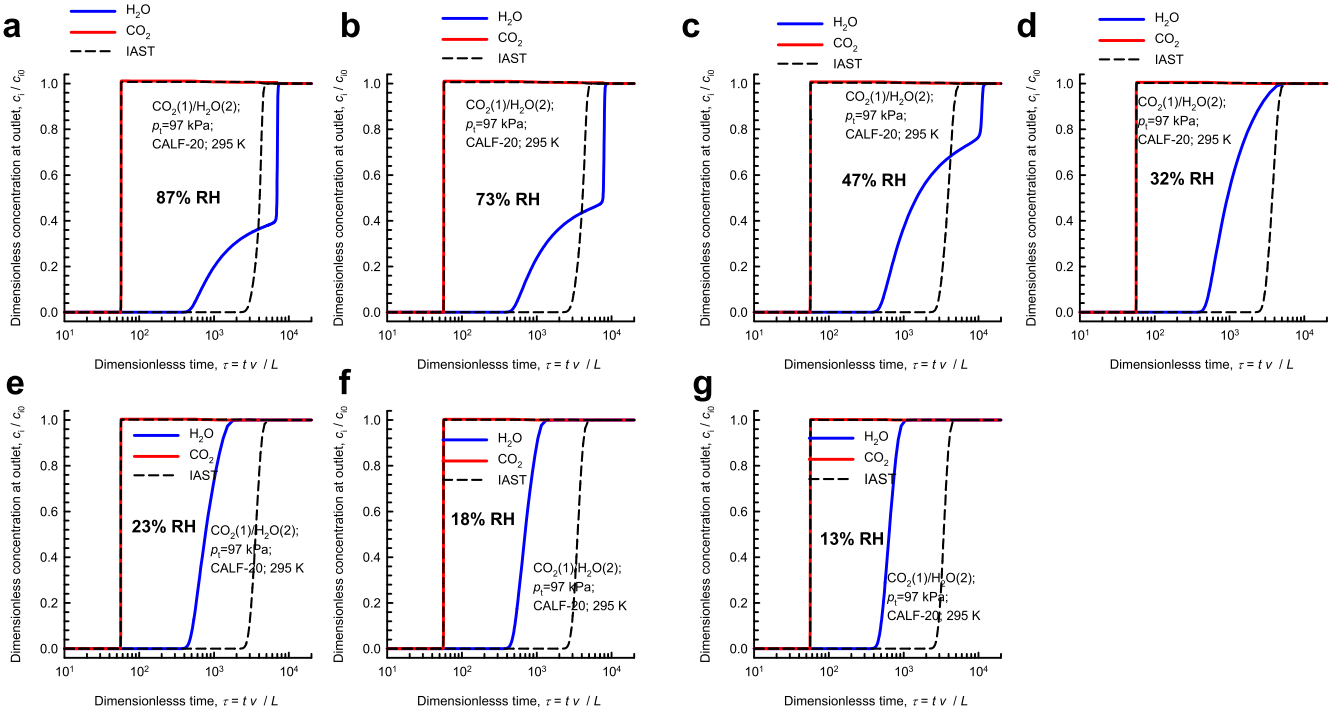

Fig. 7. Comparison of breakthrough simulations using RAST (continuous colored lines) and IAST (dashed lines) for CO_2/H_2O mixtures at a total pressure = 97 kPa, and temperature 295 K. Seven different values of %*RH* are considered. All calculation details, and input data are provided in the Supplementary Material accompanying this publication.

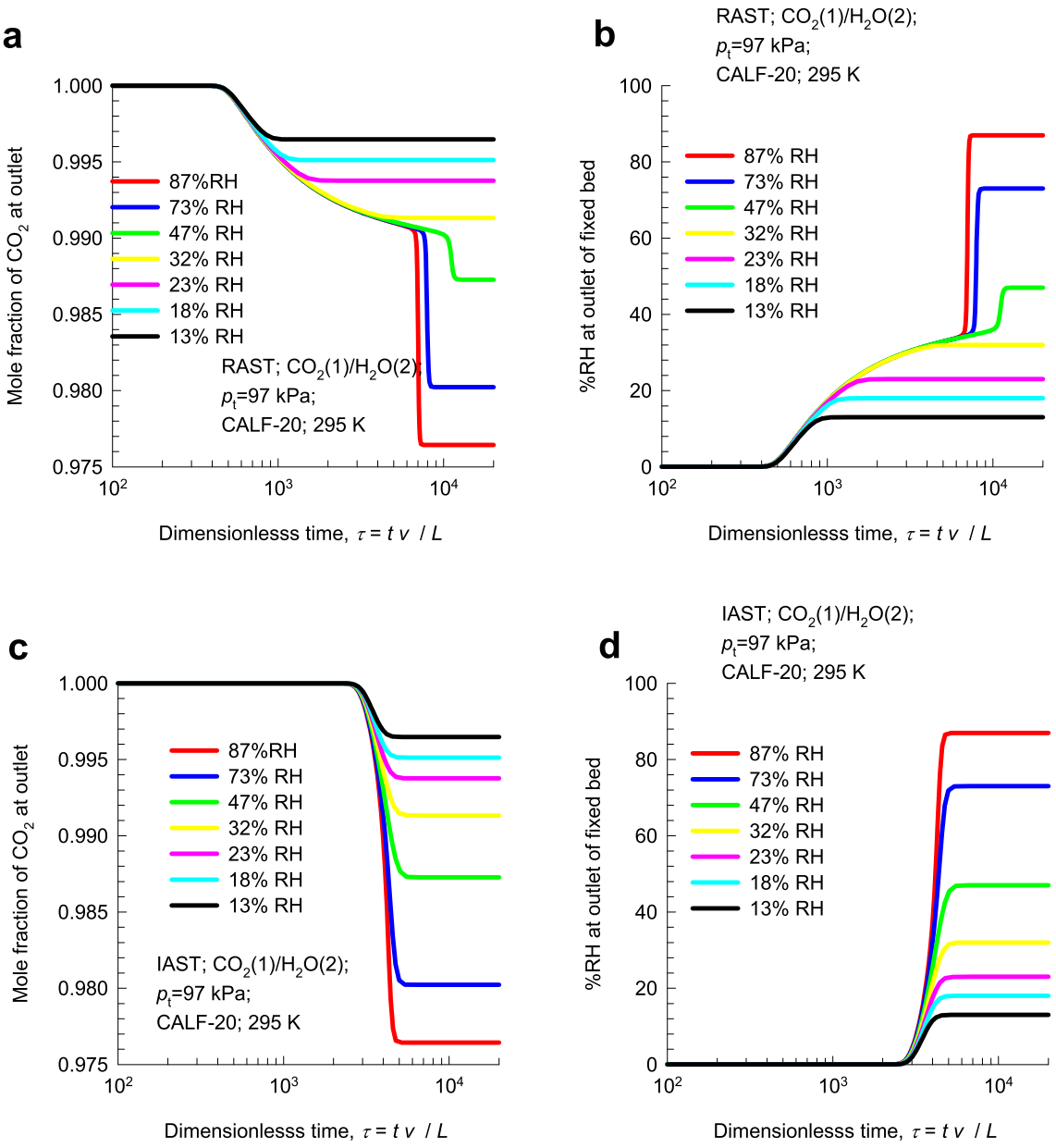

Fig. 8. Comparison of (a, c) mole fraction of CO_2, and (b, d) %*RH* of the gas mixture exiting the fixed bed determined from the breakthrough simulations using (a, b) RAST and (c, d) IAST. All calculation details, and input data are provided in the Supplementary Material accompanying this publication.

adsorption site with pairs of H_2O molecules that are hydrogen-bonded with each other. Consequently, the competition faced by CO_2 is significantly higher than anticipated by the IAST, resulting in significantly lower CO_2 uptakes. The IAST does not cater for molecular clustering resulting from hydrogen bonding between pairs of water molecules.

The modeling of thermodynamic non-idealities by introduction of activity coefficients needs to include the correction factor $(1-\exp(-C\Phi))$ in models such as the Wilson, Margules, or NRTL; this correction is of vital importance in order to ensure the proper limiting characteristics $\Phi \to 0$; $\gamma_1 \to 1$; $\gamma_2 \to 1$. Transient breakthrough simulations of CO_2/H_2O mixtures in fixed beds packed with CALF-20 are in good agreement with published breakthrough experimental data [12] provided the mixture adsorption equilibrium is appropriately described with the RAST model for mixture adsorption equilibrium.

CRediT authorship contribution statement

Rajamani Krishna: Writing – review & editing, Writing – original draft, Validation, Supervision, Methodology, Investigation, Conceptualization. **Jasper M. van Baten:** Molecular simulations, code development.

Declaration of competing interest

The authors declare that they have no known competing financial interests or personal relationships that could have appeared to influence the work reported in this paper.

Data availability

All data are provided in the Supplementary Material

Acknowledgement

The authors grateful acknowledge Dr. K. Gopalsamy and Prof G. Maurin for providing the atomic charges in CALF-20.

Appendix A. Supplementary material

Supplementary material to this article can be found online at https://doi.org/10.1016/j.seppur.2024.128269.

References

[1] G.D. Pirngruber, V. Carlier, D. Leinekugel-le-Cocq, Post-combustion CO_2 capture by vacuum swing adsorption using zeolites – a feasibility study, Oil Gas Sci. Technol. 69 (2014) 989–1003.

[2] N.S. Wilkins, A. Rajendran, Measurement of competitive CO_2 and N_2 adsorption on Zeolite 13X for post-combustion CO_2 capture, Adsorption 25 (2019) 115–133, https://doi.org/10.1007/s10450-018-00004-2.

[3] R. Krishna, J.M. van Baten, A comparison of the CO_2 capture characteristics of zeolites and metal-organic frameworks, Sep. Purif. Technol. 87 (2012) 120–126, https://doi.org/10.1016/j.seppur.2011.11.031.

[4] R. Krishna, Metrics for evaluation and screening of metal-organic frameworks for applications in mixture separations, ACS Omega 5 (2020) 16987–17004, https://doi.org/10.1021/acsomega.0c02218.

[5] D.M. Ruthven, S. Farooq, K.S. Knaebel, Pressure swing adsorption, VCH Publishers, New York, 1994.

[6] R. Krishna, Screening metal-organic frameworks for mixture separations in fixed-bed adsorbers using a combined selectivity/capacity metric, RSC Adv. 7 (2017) 35724–35737, https://doi.org/10.1039/C7RA07363A.

[7] R.T. Yang, Gas separation by adsorption processes, Butterworth, Boston, 1987.

[8] J.-B. Lin, T.T.T. Nguyen, R. Vaidhyanathan, J. Burner, J.M. Taylor, H. Durekova, F. Akhtar, R.K. Mah, O. Ghaffari-Nik, S. Marx, N. Fylstra, S.S. Iremonger, K. W. Dawson, P. Sarkar, P. Hovington, A. Rajendran, T.K. Woo, G.K.H. Shimizu, A scalable metal-organic framework as a durable physisorbent for carbon dioxide capture, Science 374 (2021) 1464–1469, https://doi.org/10.1126/science.abi7281.

[9] K. Gopalsamy, D. Fan, N. S, Y. Magnin, G. Maurin, Engineering of an Iso-reticular Series of CALF-20 MOF for CO_2 capture, ACS Appl. Eng. Mater. 2 (2024) 96–103, https://doi.org/10.1021/acsaenm.3c00622.

[10] C.-H. Ho, F. Paesani, Elucidating the competitive adsorption of H_2O and CO_2 in CALF-20: new insights for enhanced carbon capture metal−organic frameworks, ACS Appl. Mater. Interf. 15 (2023) 48287–48295, https://doi.org/10.1021/acsami.3c11092.

[11] Y. Magnin, E. Dirand, G. Maurin, P.L. Llewellyn, Abnormal CO_2 and H_2O diffusion in CALF-20(Zn) metal-organic framework: fundamental understanding of CO_2 capture, ACS Appl. Nano Mater. 6 (2023) 19963–19971, https://doi.org/10.1021/acsanm.3c03752.

[12] T.T.T. Nguyen, B.M. Balasubramaniam, N. Fylstra, R.P.S. Huynh, G.K.H. Shimizu, A. Rajendran, Competitive CO_2/H_2O adsorption on CALF-20, Ind. Eng. Chem. Res. 63 (2024) 3265–3281, https://doi.org/10.1021/acs.iecr.3c04266.

[13] T.T.T. Nguyen, Humid Post-Combustion CO_2 capture By Vacuum Swing Adsorption Using CALF-20, University of Alberta, Alberta, 2021. Ph.D. Thesis, Ph.D. Thesis,.

[14] H. Kaur, B.D. Marshall, Real adsorbed solution theory model for the adsorption of CO_2 from humid gas on CALF-20, ChemRxiv (2023) 1–18, https://doi.org/10.26434/chemrxiv-2023-2cp2c.

[15] A. Rajendran, G.K.H. Shimizu, T.K. Woo, The Challenge of water competition in physical adsorption of CO_2 by porous solids for carbon capture applications – a short perspective, Adv. Mater. 36 (2024) 2301730, https://doi.org/10.1002/adma.202301730.

[16] R. Oktavian, R. Goeminne, L.T. Glasby, P. Song, R. Huynh, O.T. Qazvini, O. Ghaffari-Nik, N. Masoumifard, J.L. Cordiner, P. Hovington, V. Van Speybroeck, P.Z. Moghadam, Gas adsorption and framework flexibility of CALF-20 explored via experiments and simulations, Nat. Commun. 15 (2024) 3898, https://doi.org/10.1038/s41467-024-48136-0.

[17] Z. Chen, C.-H. Ho, X. Wang, S.M. Vornholt, T.M. Rayder, T. Islamoglu, O.K. Farha, F. Paesani, K.W. Chapman, Humidity-responsive polymorphism in CALF-20: a resilient MOF physisorbent for CO_2 capture, ACS Mater. Lett. 5 (2023) 2942–2947, https://doi.org/10.1021/acsmaterialslett.3c00930.

[18] A.L. Myers, J.M. Prausnitz, Thermodynamics of mixed gas adsorption, A.I.Ch.E.J. 11 (1965) 121–130, https://doi.org/10.1002/aic.690110125.

[19] R. Krishna, J.M. van Baten, R. Baur, Highlighting the origins and consequences of thermodynamic nonidealities in mixture separations using zeolites and metal-organic frameworks, Microporous Mesoporous Mater. 267 (2018) 274–292, https://doi.org/10.1016/j.micromeso.2018.03.013.

[20] R. Krishna, J.M. van Baten, Fundamental Insights into the variety of factors that influence water/alcohol membrane permeation selectivity, J. Membr. Sci. 698 (2024) 122635, https://doi.org/10.1016/j.memsci.2024.122635.

[21] R. Krishna, J.M. Van Baten, How reliable is the ideal adsorbed solution theory for estimation of mixture separation selectivities in microporous crystalline adsorbents? ACS Omega 6 (2021) 15499–15513, https://doi.org/10.1021/acsomega.1c02136.

[22] R. Krishna, J.M. Van Baten, Water/alcohol mixture adsorption in hydrophobic materials: enhanced water ingress caused by hydrogen bonding, ACS Omega 5 (2020) 28393–28402, https://doi.org/10.1021/acsomega.0c04491.

[23] R. Krishna, J.M. Van Baten, Using molecular simulations for elucidation of thermodynamic non-idealities in adsorption of CO_2-containing mixtures in NaX zeolite, ACS Omega 5 (2020) 20535–20542, https://doi.org/10.1021/acsomega.0c02730.

[24] R. Krishna, J.M. Van Baten, Elucidation of selectivity reversals for binary mixture adsorption in microporous adsorbents, ACS Omega 5 (2020) 9031–9040, https://doi.org/10.1021/acsomega.0c01051.

[25] R. Krishna, J.M. Van Baten, Investigating the non-idealities in adsorption of CO_2-bearing mixtures in cation-exchanged zeolites, Sep. Purif. Technol. 206 (2018) 208–217, https://doi.org/10.1016/j.seppur.2018.06.009.

[26] M. Hefti, D. Marx, L. Joss, M. Mazzotti, Adsorption equilibrium of binary mixtures of carbon dioxide and nitrogen on zeolites ZSM-5 and 13X, Microporous Mesoporous Mater. 215 (2015) 215–228.

[27] I. van Zandvoort, E.-J. Ras, R. de Graaf, R. Krishna, Using transient breakthrough experiments for screening of adsorbents for separation of C_2H_4/CO_2 mixtures, Sep. Purif. Technol. 241 (2020) 116706, https://doi.org/10.1016/j.seppur.2020.116706.

[28] I. van Zandvoort, J.K. van der Waal, E.-J. Ras, R. de Graaf, R. Krishna, Highlighting non-idealities in C_2H_4/CO_2 mixture adsorption in 5A zeolite, Sep. Purif. Technol. 227 (2019) 115730, https://doi.org/10.1016/j.seppur.2019.115730.

[29] Y. Wang, M.D. LeVan, Adsorption equilibrium of binary mixtures of carbon dioxide and water vapor on zeolites 5A and 13X, J. Chem. Eng. Data 55 (2010) 3189–3195, https://doi.org/10.1021/je100053g.

[30] R. Krishna, J.M. van Baten, In silico screening of metal-organic frameworks in separation applications, Phys. Chem. Chem. Phys. 13 (2011) 10593–10616, https://doi.org/10.1039/C1CP20282K.

[31] R. Krishna, J.M. van Baten, In silico screening of zeolite membranes for CO_2 capture, J. Membr. Sci. 360 (2010) 323–333, https://doi.org/10.1016/j.memsci.2010.05.032.

[32] R. Krishna, J.M. van Baten, Describing mixture diffusion in microporous materials under conditions of pore saturation, J. Phys. Chem. C 114 (2010) 11557–11563.

[33] R. Krishna, J.M. van Baten, Diffusion of alkane mixtures in zeolites. validating the maxwell-stefan formulation using MD simulations, J. Phys. Chem. B 109 (2005) 6386–6396.

[34] R. Krishna, J.M. van Baten, Insights into diffusion of gases in zeolites gained from molecular dynamics simulations, Microporous Mesoporous Mater. 109 (2008) 91–108.

[35] R. Krishna, Describing the diffusion of guest molecules inside porous structures, J. Phys. Chem. C 113 (2009) 19756–19781, https://doi.org/10.1021/jp906879d.

[36] R. Krishna, Diffusion in porous crystalline materials, Chem. Soc. Rev. 41 (2012) 3099–3118, https://doi.org/10.1039/C2CS15284C.

[37] S.L. Mayo, B.D. Olafson, W.A. Goddard, DREIDING: a generic force field for molecular simulations, J. Phys. Chem. 94 (1990) 8897–8909.

[38] A. García-Sánchez, C.O. Ania, J.B. Parra, D. Dubbeldam, T.J.H. Vlugt, R. Krishna, S. Calero, Development of a transferable force field for carbon dioxide adsorption in zeolites, J. Phys. Chem. C 113 (2009) 8814–8820, https://doi.org/10.1021/jp810871f.

[39] H.W. Horn, W.C. Swope, J.W. Pitera, J.D. Madura, T.J. Dick, G.L. Hura, T. Head-Gordon, Development of an improved four-site water model for biomolecular simulations: TIP4P-Ew, J. Chem. Phys. 120 (2004) 9665, https://doi.org/10.1063/1.1683075.

[40] C. Zhang, X. Yang, Molecular dynamics simulation of ethanol/water mixtures for structure and diffusion properties, Fluid Phase Equilib. 231 (2005) 1–10.

[41] R. Krishna, J.M. van Baten, Hydrogen bonding effects in adsorption of water-alcohol mixtures in zeolites and the consequences for the characteristics of the maxwell-stefan diffusivities, Langmuir 26 (2010) 10854–10867, https://doi.org/10.1021/la100737c.

[42] O. Talu, A.L. Myers, Rigorous thermodynamic treatment of gas-adsorption, A.I.Ch.E.J. 34 (1988) 1887–1893.

[43] O. Talu, I. Zwiebel, Multicomponent adsorption equilibria of nonideal mixtures, A.I.Ch.E.J. 32 (1986) 1263–1276.

[44] F.R. Siperstein, A.L. Myers, Mixed-gas adsorption, A.I.Ch.E.J. 47 (2001) 1141–1159.

[45] R. Krishna, Thermodynamic insights into the characteristics of unary and mixture permeances in microporous membranes, ACS Omega 4 (2019) 9512–9521, https://doi.org/10.1021/acsomega.9b00907.

[46] R. Krishna, J.M. Van Baten, Using molecular simulations to unravel the benefits of characterizing mixture permeation in microporous membranes in terms of the spreading pressure, ACS Omega 5 (2020) 32769–32780, https://doi.org/10.1021/acsomega.0c05269.

[47] S. Sochard, N. Fernandes, J.-M. Reneaume, Modeling of adsorption isotherm of a binary mixture with real adsorbed solution theory and nonrandom two-liquid model, A.I.Ch.E.J. 56 (2010) 3109–3119.

[48] N. Mittal, P. Bai, I. Siepmann, P. Daoutidis, M. Tsapatsis, Bioethanol enrichment using zeolite membranes: molecular modeling, conceptual process design and techno-economic analysis, J. Membr. Sci. 540 (2017) 464–476.

[49] G. Calleja, A. Jimenez, J. Pau, L. Domínguez, P. Pérez, Multicomponent adsorption equilibrium of ethylene, propane, propylene and CO_2 on 13X zeolite, Gas Sep. Purif. 8 (1994) 247–256.

[50] R. Krishna, Highlighting the influence of thermodynamic coupling on kinetic separations with microporous crystalline materials, ACS Omega 4 (2019) 3409–3419, https://doi.org/10.1021/acsomega.8b03480.

[51] R. Krishna, Synergistic and antisynergistic intracrystalline diffusional influences on mixture separations in fixed bed adsorbers, Precis. Chem. 1 (2023) 83–93, https://doi.org/10.1021/prechem.2c00003.

[52] R. Krishna, Fundamental insights into intra-crystalline diffusional influences on mixture separations in fixed bed adsorbers, Chem. Bio. Eng. 1 (2024) 53–66, https://doi.org/10.1021/cbe.3c00057.

Supplementary Material

Elucidating the Failure of the Ideal Adsorbed Solution Theory for CO_2/H_2O Mixture Adsorption in CALF-20

Rajamani Krishna* and Jasper M. van Baten

Van 't Hoff Institute for Molecular Sciences

University of Amsterdam

Science Park 904

1098 XH Amsterdam, The Netherlands

email: r.krishna@uva.nl; r.krishna@contact.uva.nl

ORCID 0000-0002-4784-8530

Contents

1 The Ideal Adsorbed Solution Theory

We provide a brief outline of the Ideal Adsorbed Solution Theory for calculation of mixture adsorption equilibrium.

1.1 Gibbsian thermodynamics of mixture adsorption

The Gibbs adsorption equation[1] in differential form is

$$Ad\pi = \sum_{i=1}^{n} q_i d\mu_i \tag{S1}$$

The quantity A is the surface area per kg of framework, with units of m^2 per kg of the framework of the crystalline material; q_i is the molar loading of component i in the adsorbed phase with units moles per kg of framework; μ_i is the molar chemical potential of component i. The spreading pressure π has the same units as surface tension, i.e. N m^{-1}.

The chemical potential of any component in the adsorbed phase, μ_i, equals that in the bulk fluid phase. If the partial fugacities in the bulk fluid phase are f_i, we have

$$d\mu_i = RTd\ln f_i \tag{S2}$$

where R is the gas constant (= 8.314 J mol^{-1} K^{-1}).

Briefly, the basic equation of Ideal Adsorbed Solution Theory (IAST) theory of Myers and Prausnitz[2] is the analogue of Raoult's law for vapor-liquid equilibrium, i.e.

$$f_i = P_i^0 x_i; \quad i = 1, 2, ...n \tag{S3}$$

where x_i is the mole fraction in the adsorbed phase

$$x_i = \frac{q_i}{q_1 + q_2 + ...q_n} \tag{S4}$$

and P_i^0 is the pressure for sorption of every component *i*, which yields the same spreading pressure, π for each of the pure components, as that for the mixture:

$$\frac{\pi A}{RT} \equiv \Phi = \int_0^{P_1^0} \frac{q_1^0(f)}{f} df = \int_0^{P_2^0} \frac{q_2^0(f)}{f} df = \int_0^{P_3^0} \frac{q_3^0(f)}{f} df = ... \tag{S5}$$

where $q_i^0(f)$ is the *pure* component adsorption isotherm. The units of $\Phi \equiv \frac{\pi A}{RT}$, also called the surface potential, [3-7] are mol kg^{-1}.

The unary isotherm may be described by say the 1-site Langmuir isotherm

$$q^0(f) = q_{sat} \frac{bf}{1+bf}; \quad \theta = \frac{bf}{1+bf} \tag{S6}$$

where we define the fractional *occupancy* of the adsorbate molecules, $\theta = q^0(f)/q_{sat}$. The superscript 0 is used to emphasize that $q^0(f)$ relates the *pure component* loading to the bulk fluid fugacity. For unary isotherms described by the dual-site Langmuir-Freundlich (DSLF) model

$$q^0(f) = q_{A,sat} \frac{b_A f^{\nu A}}{1+b_A f^{\nu A}} + q_{B,sat} \frac{b_B f^{\nu B}}{1+b_B f^{\nu B}} \tag{S7}$$

each of the integrals in eq (S5) can be evaluated analytically. The integration yields for component *i*,

$$\begin{aligned} \Phi \equiv \frac{\pi A}{RT} &= \int_{f=0}^{P_i^0} \frac{q_i^0(f)}{f} df = \frac{q_{A,sat}}{\nu_A} \ln\left(1+b_A\left(P_i^0\right)^{\nu_A}\right) + \frac{q_{B,sat}}{\nu_B} \ln\left(1+b_B\left(P_i^0\right)^{\nu_B}\right); \\ \Phi \equiv \frac{\pi A}{RT} &= \int_{f=0}^{P_i^0} \frac{q_i^0(f)}{f} df = \frac{q_{A,sat}}{\nu_A} \ln\left(1+b_A\left(\frac{f_i}{x_i}\right)^{\nu_A}\right) + \frac{q_{B,sat}}{\nu_B} \ln\left(1+b_B\left(\frac{f_i}{x_i}\right)^{\nu_B}\right) \end{aligned} \tag{S8}$$

The right hand side of eq (S8) is a function of P_i^0. For multicomponent mixture adsorption, each of the equalities on the right hand side of Eq (S5) must be satisfied. These constraints may be solved using a suitable equation solver, to yield the set of values of , P_2^0, P_3^0 ,.. P_n^0, each of which satisfy eq (S5). The corresponding values of the integrals using these as upper limits of integration must yield the same value of Φ for each component; this ensures that the obtained solution is the correct one.

In the IAST, the adsorbed phase mole fractions x_i are then determined from

$$x_i = \frac{f_i}{P_i^0}; \quad i = 1, 2, ...n \tag{S9}$$

The applicability of eqs (S3) and (S9) mandates that all of the adsorption sites within the microporous material are equally accessible to each of the guest molecules, implying a homogeneous distribution of guest adsorbates within the pore landscape, with no preferential locations of any guest species. The circumstances in which this mandate is not fulfilled are highlighted in recent works.[5, 6, 8, 9]

A further key assumption of the IAST is that the adsorption enthalpies and surface areas of the adsorbed molecules do not change upon mixing.[10] If the total mixture loading is q_t, the area covered by the adsorbed mixture is $\frac{A}{q_t}$ with units of m^2 (mol mixture)$^{-1}$. Therefore, the assumption of no surface area change due to mixture adsorption translates as $\frac{A}{q_t} = \frac{Ax_1}{q_1^0\left(P_1^0\right)} + \frac{Ax_2}{q_2^0\left(P_2^0\right)} + \cdots \frac{Ax_n}{q_n^0\left(P_n^0\right)}$; the total mixture loading is q_t is calculated from

$$q_t = q_1 + q_2 ... + q_n = \frac{1}{\frac{x_1}{q_1^0(P_1^0)} + \frac{x_2}{q_2^0(P_2^0)} + ... + \frac{x_n}{q_n^0(P_n^0)}} \tag{S10}$$

in which $q_1^0(P_1^0)$, $q_2^0(P_2^0)$,… $q_n^0(P_n^0)$ are determined from the unary isotherm fits, using the sorption pressures for each component P_1^0, P_2^0, P_3^0,.. P_n^0 that are available from the solutions to equations Eqs (S5), and (S8).

The occurrence of molecular clustering and hydrogen bonding should be expected to applicability of eq (S10) because the surface area occupied by a molecular cluster is different from that of each of the un-clustered guest molecules in the adsorbed phase; see published literature for details.[7, 9, 11]

The entire set of eqs (S3) to (S10) need to be solved numerically to obtain the loadings, q_i of the individual components in the mixture.

In a number of publications on CO_2 capture from mixtures containing N_2, CH_4, C_2H_4, C_2H_6, C_3H_8, and H_2O using cation-exchanged zeolites,[5, 6, 8, 10, 12-17] the IAST has been shown to fail due to non-compliance with one or more of the afore-mentioned tenets.

For binary mixture adsorption, the selectivity of guest constituent *i* with respect to another guest constituent *j*, in that mixture, S_{ads}, is defined by

$$S_{ads} = \frac{q_1/q_2}{f_1/f_2} = \frac{x_1/f_1}{x_2/f_2} \tag{S11}$$

where q_i are the molar loadings of the constituents in the adsorbed phase in equilibrium with a bulk fluid phase mixture with partial fugacities f_i. In view of eqs (S9), and (S10), we may re-write eq (S11) as the ratio of the sorption pressures

$$S_{ads} = \frac{P_2^0}{P_1^0} \tag{S12}$$

Applying the restriction specified by eq (S5), it follows that $S_{ads,ij}$ is uniquely determined by the surface potential Φ.

For further explanation on the numerical techniques for solving the IAST, fitting of isotherms, the tenets of the IAST, the concept of the surface potential, watch the presentations titled **The IAST for Mixture Adsorption Equilibrium, Dependence of Adsorption Selectivity on Mixture Composition, Adsorption Selectivity vs Total Pressure, Significance of the Spreading Pressure Concept, Hydrogen Bonding Influences on Adsorption, Langmuir Model for Binary Mixture Adsorption, Reversals in Adsorption Selectivity, Competitive CO_2/H_2O Mixture Adsorption in CALF-20** on YouTube https://www.youtube.com/@rajamanikrishna250/videos

1.2 The fractional pore occupancy

From knowledge of the surface potential, Φ, the fractional pore occupancy θ for mixture adsorption is then calculated using

$$\theta = 1 - \exp\left(-\frac{\pi A}{q_{sat,mix} RT}\right) = 1 - \exp\left(-\frac{\Phi}{q_{sat,mix}}\right) \tag{S13}$$

For binary mixtures the saturation capacity $q_{sat,mix}$ is calculated from the saturation capacities of the constituent guests

$$\frac{1}{q_{sat,mix}} = \frac{x_1}{q_{1,sat}} + \frac{x_2}{q_{2,sat}}; \quad q_{i,sat} = q_{i,A,sat} + q_{i,B,sat}; \quad i = 1,2 \tag{S14}$$

Where x_i are the mole fractions in the adsorbed mixture. The fundamental justification of eq (S14) is provided by invoking eq (S10).

2 CO_2/H_2O adsorption in CALF-20 vs IAST

The unary isotherm data for structured CALF-20 (80% MOF:20% polysulfone) at 295 K are presented in Figure S1a, along with DSLF fits using the parameters in Table S1. Figure S1b presents the experimental data of Lin et al.[18] (indicated by symbols) on component loadings for CO_2(1)/H_2O(2) mixture adsorption in structured CALF-20 (80% MOF:20% polysulfone) at 295 K. The component loadings were determined from breakthrough experiments in CALF-20 structured composite (80% MOF:20% polysulfone).[18-21] The total pressure in the bulk gas phase, p_t = 97 kPa. In Figure S1b, the loadings are plotted against $\%\text{Relative Humidity} = \frac{p_2}{p_2^{sat}} \times 100$ where p_2 is the partial pressure of water in the bulk gas phase, and p_2^{sat} is the saturation vapor pressure of water. At 295 K, p_2^{sat} is determined from the Antoine equation: $p_2^{sat} = 10^{\left(A - \frac{B}{T - 273.15 + C}\right)} \times 10^5 = 2628$ Pa

$A = 5.11564; B = 1687.537; C = 230.17$.

The Antoine vapor pressure constants are taken from the NIST webbook: http://webbook.nist.gov/chemistry/.

Figure S1b presents the data for CO_2(1)/H_2O(2) mixture adsorption in structured CALF-20; these data have been backed-out from transient breakthrough experiments. [18, 20, 21] The dashed lines in Figure S1b are the IAST estimations; for this purpose the unary isotherm fits are as reported in Table S1. The IAST estimates are in poor agreement with the experimental data. For $0 < \%\text{RH} < 40$, it is noteworthy that the H_2O loading in the CO_2(1)/H_2O(2) mixture is lower than the IAST estimates of H_2O loading.

Another way to demonstrate the non-idealities is to plot the mole fraction of CO_2 in the adsorbed phase mixture, x_1, as a function of the $\%\text{Relative Humidity} = \frac{p_2}{p_2^{sat}} \times 100$; see Figure S1c. We note that for $\%\text{RH} < 40; x_1 > 0.5$, the adsorbed phase mixture is richer in CO_2 than is anticipated by the IAST. On the

other hand, for $\%RH > 40; x_1 < 0.5$, the adsorbed phase mixture is poorer in CO_2 than is anticipated by the IAST.

The Monte Carlo simulations reported by Gopalsamy et al.[22] for $CO_2(1)/H_2O(2)$ mixture adsorption in CALF-20 at 293 K are presented in Figure S2. The partial pressure of $CO_2(1)$ is held practically constant at the value of 20 kPa; the mole fraction of H_2O in the bulk gas mixture, y_2, is varied. The dashed lines are the IAST estimations; for this purpose, the unary isotherm fits used are those provided in Table S2. We note that the CO_2/H_2O binary mixture adsorption exhibits significant departures from thermodynamic idealities. Another way to demonstrate the non-idealities is to plot the mole fraction of CO_2 in the adsorbed phase mixture, x_1, as a function of the mole fraction of H_2O in the bulk gas mixture, y_2; see Figure S2c. We note that for $y_2 < 0.05; x_1 > 0.3$, the adsorbed phase mixture is richer in CO_2 than is anticipated by the IAST. On the other hand, for $y_2 > 0.05; x_1 < 0.3$, the adsorbed phase mixture is poorer in CO_2 than is anticipated by the IAST.

2.1 List of Tables for CO2/H2O adsorption in CALF-20 vs IAST

Table S1. Dual-site Langmuir-Freundlich parameters for CO_2 (1) and H_2O (2) determined from fitting unary isotherms determined at 295 K from breakthrough experiments in structured CALF-20 (80% MOF:20% polysulfone).[18-21] For calculation of the % Relative Humidity, the saturation vapor pressure of water, p_2^{sat}, at 295 K is determined from the Antoine equation; $p_2^{sat} = 2628$ Pa .

	Site A			Site B		
	$\frac{q_{A,sat}}{\text{mol kg}^{-1}}$	$\frac{b_A}{\text{Pa}^{-\nu_A}}$	ν_A	$\frac{q_{B,sat}}{\text{mol kg}^{-1}}$	$\frac{b_B}{\text{Pa}^{-\nu_B}}$	ν_B
CO_2 $R^2 = 0.99994$	2.7	2.94E-04	1	1	3.15E-06	1
H_2O $R^2 = 0.986488$	8.5583	2.89E-06	2			

Fitted Margules non-ideality parameters for binary CO_2/H_2O mixture adsorption at 295 K in CALF-20 (80% MOF:20% polysulfone).

	C / kg mol^{-1}	A_{12}	A_{21}
CO_2/H_2O at 295 K	0.050	1.962	4.836

Table S2. Dual-site Langmuir-Freundlich parameters for CO_2 (1) and H_2O (2) determined from fitting unary isotherms determined at 293K from molecular simulations in CALF-20.[22] For calculation of the % Relative Humidity, the saturation vapor pressure of water, p_2^{sat}, at 293 K is determined from the Antoine equation; $p_2^{sat} = 2330$ Pa.

	Site A			Site B		
	$\frac{q_{A,sat}}{\text{mol kg}^{-1}}$	$\frac{b_A}{\text{Pa}^{-\nu_A}}$	ν_A	$\frac{q_{B,sat}}{\text{mol kg}^{-1}}$	$\frac{b_B}{\text{Pa}^{-\nu_B}}$	ν_B
CO_2 $R^2 = 0.99966$	1.9	1.408E-11	2.15	3.3	3.194E-04	1
H_2O $R^2 = 0.997126$	10.8	2.095E-29	10.75	2.2	1.446E-04	1

Fitted Margules non-ideality parameters for binary CO_2/H_2O mixture adsorption at 293 K in CALF-20.

	C / kg mol^{-1}	A_{12}	A_{21}
CO_2/H_2O at 293 K	0.075	4.176	0.551

2.2 List of Figures for CO2/H2O adsorption in CALF-20 vs IAST

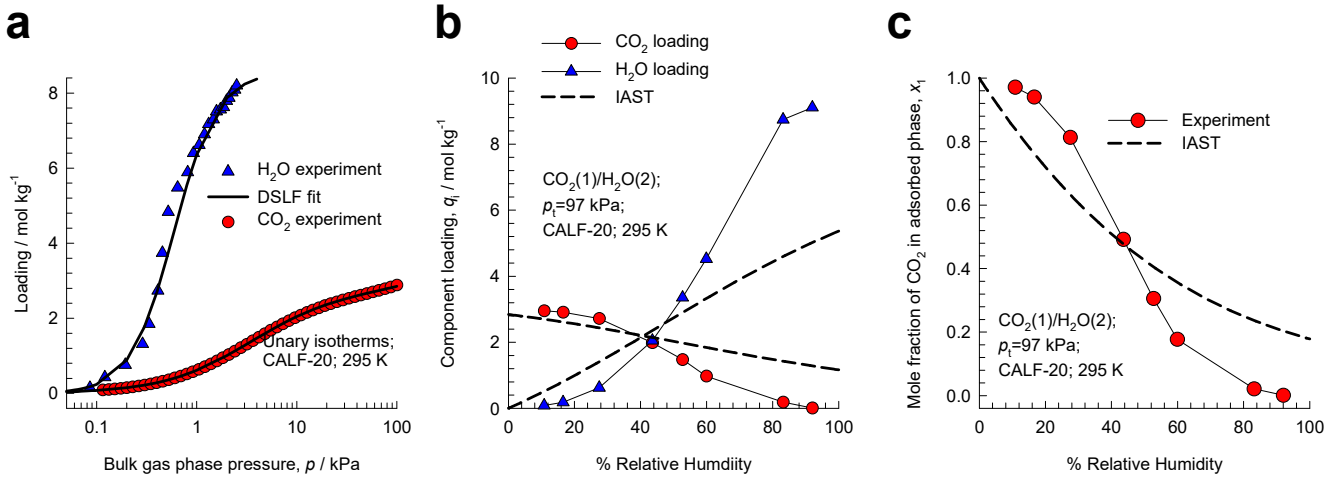

Figure S1. (a) Experimental data of Lin et al.[18] (indicated by symbols) on component loadings for $CO_2(1)/H_2O(2)$ mixture adsorption in structured CALF-20 (80% MOF:20% polysulfone) at 295 K. The total pressure in the bulk gas phase is 97 kPa. The unary isotherm DSLF fit parameters are provided in Table S1. In (b) the loadings are plotted against % relative humidity. (c) Plot of the mole fraction of CO_2 in the adsorbed phase mixture, x_1, as a function of the % relative humidity. The dashed lines are the IAST estimations.

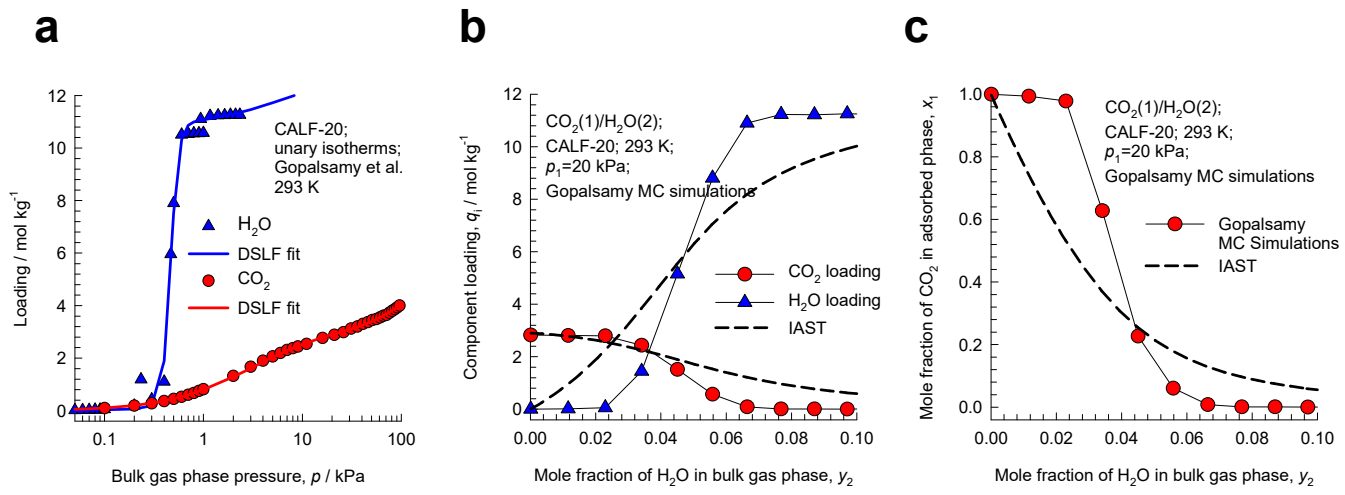

Figure S2. (a) Monte Carlo simulations reported by Gopalsamy et al.[22] for unary isotherms at 293 K. The unary isotherm DSLF fit parameters are provided in Table S2. (b) CBMC simulations of component loadings, q_i, for $CO_2(1)/H_2O(2)$ mixture adsorption in CALF-20 at 293 K; these are the Monte Carlo simulations reported by Gopalsamy et al.[22] The partial pressure of $CO_2(1)$ is held practically constant at the value of 20 kPa. The mole fraction of H_2O in the bulk gas mixture, y_2, is varied. (c) Plot of the mole fraction of CO_2 in the adsorbed phase mixture, x_1, as a function of the mole fraction of H_2O in the bulk gas mixture, y_2. The dashed lines are the IAST estimations/

3 Configurational-Bias Monte Carlo (CBMC) simulations

In order to rationalize and elucidate the failure of the IAST for the three different sets of data for CO_2(1)/H_2O(2) mixture adsorption data observed in Figure S1, and Figure S2, we undertook molecular simulations. Configurational-Bias Monte Carlo (CBMC) simulations were carried out to determine the adsorption isotherms for unary CO_2, unary H_2O, and CO_2/H_2O mixtures in CALF-20 at 298 K. The simulation methodologies are the same as detailed in earlier publications.[23-29] unit cell was constructed using the structural information obtainable from CCDC 2084733 at https://www.ccdc.cam.ac.uk/structures/Search?Ccdcid=CCDC%202084733&DatabaseToSearch=Published

Oktavian et al.[30] have undertaken molecular simulations, along with experiments, to explore the influence of framework flexibility of CALF-20 on adsorption separation performance. Our limited objective in this work is to provide a fundamental explanation for the failure of the IAST for description of mixture adsorption equilibrium; therefore, the CALF-20 structure was considered to be rigid in the simulations.

The unit cell dimensions of CALF-20 crystals are $a = 8.9138$ Å; $b = 9.6935$ Å; $c = 9.4836$ Å with angles $\alpha = 90°$; $\beta = 115.895°$; $\gamma = 90°$; see Figure S3. The crystal framework density $\rho = 1598.868$ kg m^{-3}. The simulation box for conducting CBMC simulations consisted of $5 \times 3 \times 5 = 75$ unit cells.

The interactions between adsorbed molecules are described with Lennard-Jones terms together with electrostatic interactions. For the atoms in the host metal organic framework (see Figure S4), the generic DREIDING[31] force fields were used; the Lennard-Jones parameters $\sigma_{host}, \frac{\varepsilon_{host}}{k_B}$ values are specified in

Table S3, along with the partial charges.[22] CO_2 was described by a 3-site charged Lennard-Jones model as described by Garcia-Sánchez et al.[32] Water is modeled using the four-site TIP4P-Ew potential; [33] TIP4P = 4-site transferable intermolecular potential (TIP4P) and Ew = Ewald technique.

The Lorentz-Berthelot mixing rules were applied for calculating the Lennard-Jones parameters describing guest-host interactions

$$\sigma_{guest-host} = \frac{\left(\sigma_{guest} + \sigma_{host}\right)}{2}$$
$$\frac{\varepsilon_{guest-host}}{k_B} = \sqrt{\frac{\varepsilon_{guest}}{k_B} \times \frac{\varepsilon_{host}}{k_B}} \qquad \text{(S15)}$$

The Lennard-Jones potentials are shifted and cut at 12 Å. The pore landscapes are shown in Figure S5.

3.1 CBMC simulations for CO_2/H_2O mixture adsorption

Figure S6a presents the CBMC simulations conducted in this work for unary isotherms for CO_2(1) and H_2O(2) at 298 K. These isotherms are fitted with the dual-site Langmuir-Freundlich model, with fit parameters as specified in Table S4. Figure S6b,c present comparisons of unary CBMC isotherm for CO_2 and H_2O isotherms at 298 K with CBMC simulations of Gopalsamy et al.[22] at 293 K. Also shown are the experimental unary isotherms for CO_2 and H_2O from Lin et al.[18]

Figure S6d shows CBMC simulations of component loadings, q_i, for CO_2(1)/H_2O(2) mixture adsorption in CALF-20 at 298 K at a total fugacity = 15 kPa. The mole fraction of H_2O in the bulk gas mixture, y_2, is varied. In Figure S6d, the loadings are plotted against $\%\text{Relative Humidity} = \frac{f_2}{p_2^{sat}} \times 100$ where f_2 is the partial fugacity of water in the bulk gas phase, and p_2^{sat} is the saturation vapor pressure of water. At 298 K, p_2^{sat} is determined from the Antoine equation: $p_2^{sat} = 3150$ Pa.

The dashed lines in Figure S6d are the IAST estimations; for this purpose the unary isotherm fits used are those provided in Table S4. We note that the CO_2/H_2O binary mixture adsorption exhibits significant departures from thermodynamic idealities. Another way to demonstrate the non-idealities is to plot the mole fraction of CO_2 in the adsorbed phase mixture, x_1, as a function of the

$\%\text{Relative Humidity} = \frac{f_2}{p_2^{sat}} \times 100$, and the mole fraction of H_2O in the bulk gas mixture, y_2; see Figure S6e,f. We note that for $\%\text{Relative Humidity} < 20\%$; $y_2 < 0.05$; $x_1 > 0.3$, the adsorbed phase mixture is richer in CO_2, i.e. poorer in H_2O, than is anticipated by the IAST. On the other hand, for $\%\text{Relative Humidity} > 20\%$; $y_2 > 0.05$; $x_1 < 0.3$, the adsorbed phase mixture is poorer in CO_2, i.e. richer in H_2O, than is anticipated by the IAST. These characteristics mirror those observed in Figure S1b.,c.

Additionally, CBMC simulations of component loadings, q_i, for $CO_2(1)/H_2O(2)$ mixture adsorption in CALF-20 at 298 K were determined for varying total fugacity f_t, maintaining the mole fraction of H_2O in the bulk gas mixture at a constant value $y_2 = f_2 / f_t = 0.05$; see Figure S7a. The dashed lines are the IAST estimations; for this purpose the unary isotherm fits used are those provided in Table S4. Figure S7b plots the mole fraction of CO_2 in the adsorbed phase mixture, x_1, as a function of $\%\text{Relative Humidity} = \frac{f_2}{p_2^{sat}} \times 100$. We again note that for this set of CBMC simulations, two different scenarios hold. We note that for $\%\text{Relative Humidity} < 10\%$; $x_1 > 0.5$, the adsorbed phase mixture is richer in CO_2 than is anticipated by the IAST. On the other hand, for $\%\text{Relative Humidity} > 10\%$; $x_1 < 0.5$, the adsorbed phase mixture is poorer in CO_2 than is anticipated by the IAST.

The results in Figure S6, and Figure S7 are analogous to those presented in Figure S1, and Figure S2. We first seek rationalization and elucidation of the results in Figure S6.

3.2 Radial Distribution Functions

As emphasized in earlier works,[5-7, 9, 10, 34] the applicability of the IAST for quantitative description of mixture adsorption equilibrium relies on two tenets. The first tenet is that all of the adsorption sites within the microporous material are equally accessible to each of the guest molecules, implying a homogeneous distribution of guest adsorbates within the pore landscape, with no preferential locations of any guest

species. The second tenet of the IAST is that the adsorption enthalpies and surface areas of the adsorbed molecules do not change upon mixing with other guests. The occurrence of molecular clustering and hydrogen bonding should be expected to invalidate the second tenet because the surface area occupied by a molecular cluster is different from that of each of the un-clustered guest molecules in the adsorbed phase. We investigate the applicability of both tenets of the IAST.

The first step is to appreciate the preferential location of the guest molecules. Toward this end we determined the Radial Distribution Function (RDF) of guest-to-framework-atom distances of (a) guest CO_2, and (b) guest H_2O for adsorption of $CO_2(1)/H_2O(2)$ mixture adsorption in CALF-20 at 298 K. See Figure S4 and Table S3, for explanation of the labels for the framework atoms. The total fugacity in the bulk gas phase is 15 kPa with partial fugacities f_1 = 14.4 kPa, and f_2 =0.6 kPa. The chosen conditions to the scenario in Figure S6d with $y_2 < 0.05; x_1 > 0.3$, i.e. the adsorbed phase mixture is richer in CO_2 than is anticipated by the IAST. The RDFs were determined by sampling a total of 10^6 equilibrated simulation steps, and monitoring the guest-framework distances. The plotted RDF data has been normalized such that the area under each of the curves is identical to one another; the results are presented in Figure S8a,b. The first peaks of the RDFs for both guests correspond to the guest-oxygen atoms in the CALF-20 framework, indicating that the oxygen atoms of the oxalate groups of the framework serve as the most favorable binding sites for CO_2, and H_2O.

Figure S9 shows computational snapshots CO_2, and H_2O for adsorption of $CO_2(1)/H_2O(2)$ mixture adsorption in CALF-20 at 298 K; the total fugacity in the bulk gas phase is 15 kPa with partial fugacities f_1 = 14.4 kPa, and f_2 =0.6 kPa. The chosen conditions to the scenario in Figure S6c with $y_2 < 0.05; x_1 > 0.3$, i.e. the adsorbed phase mixture is richer in CO_2 than is anticipated by the IAST.

Figure S10 shows computational snapshots CO_2, and H_2O for adsorption of $CO_2(1)/H_2O(2)$ mixture adsorption in CALF-20 at 298 K; the total fugacity in the bulk gas phase is 15 kPa with partial fugacities f_1 = 14.1 kPa, and f_2 =0.9 kPa. The chosen conditions to the scenario in Figure S6c with $y_2 > 0.05; x_1 < 0.3$, i.e. the adsorbed phase mixture is poorer in CO_2 than is anticipated by the IAST.

To investigate the possibility of non-homogeneous distribution of adsorbate guests, CBMC simulation data on the spatial locations of the guest molecules were sampled to determine the inter-molecular distances; these distances are determined from the center of gravity of each guest molecule. By sampling a total of 10^6 simulation steps, the radial distribution function (RDF) were determined for CO_2-CO_2, CO_2-H_2O, and H_2O-H_2O separation distances. Figure S11a,b presents the RDF data for guest pairs determined from CBMC simulations for CO_2(1)/H_2O(2) mixture adsorption in CALF-20 at 298 K. The total fugacity in the bulk gas phase is 15 kPa with partial fugacities: f_1 = 14.4 kPa, and f_2 =0.6 kPa. The simulation box contains a total of $5\times3\times5=75$ unit cells. Under these conditions the number of molecules in the simulation box of 75 unit cells: CO_2 = 119; H_2O = 44. Recall that 10^6 different conformations of the total of 119 + 44 = 163 molecules are analyzed. The samples were taken up to a radial distance of 30 Å, but the *x*-axis has been truncated at 12 Å because only the first few peaks are of interest in the discussions to follow. The plotted RDF data has been normalized such that the area under each of the curves is identical to one another. If we compare the first peaks, it is noteworthy that H_2O-H_2O pairs are close together at typical distances of about 3 Å. The CO_2-CO_2 pairs are typically 6.5 Å apart, occupying adjacent adsorption sites of CALF-20. The CO_2-H_2O pairs are typically 8 Å apart, occupying adjacent adsorption sites. This implies that the CO_2 molecules face a less severe competitive adsorption with H_2O than is anticipated by the IAST. The segregated nature of adsorbate locations are visually observed in Figure S9 . This explains the finding in Figure S6d that for $y_2 < 0.05$, the adsorbed phase mixture is richer in CO_2 than is anticipated by the IAST; this is a direct consequence of the fact that CO_2 faces negligible competition with H_2O.

The proximity of H_2O-H_2O pairs observed in Figure S11a suggest the possibility of hydrogen bonding. To investigate this possibility, CBMC simulation data on the spatial locations of the guest molecules were sampled to determine the $O\cdots H$ distances of H_2O-H_2O and CO_2-H_2O pairs of molecules. By sampling a total of 10^6 simulation steps, the radial distribution functions (RDF) of O···H distances were determined for H_2O-H_2O and CO_2-H_2O pairs.

Figure S12 shows the RDF of O···H distances for H_2O-H_2O and CO_2-H_2O pairs for CO_2(1)/H_2O(2) mixture adsorption in CALF-20 at 298 K. The total fugacity in the bulk gas phase is 15 kPa with partial fugacities: f_1 = 14.4 kPa, and f_2 =0.6 kPa. We note the first peak in the RDFs for H_2O-H_2O pairs occurs at a distance that is slightly less than 2 Å, that is characteristic of hydrogen bonding.[11, 35] The corresponding peak for CO_2-H_2O pairs occurs at a distance of 8.4 Å, negating the possibility of hydrogen bonding between these partner molecules.

To investigate the reasons behind the fact in Figure S6c with $y_2 > 0.05; x_1 < 0.3$, i.e. the adsorbed phase mixture is poorer in CO_2 than is anticipated by the IAST, we determined the RDF for center-to-center and O···H distances for adsorption of CO_2(1)/H_2O(2) mixture adsorption with partial fugacities f_1 = 14.1 kPa, and f_2 =0.9 kPa, with $y_2 = 0.06$. For the simulation box with a total of $5 \times 3 \times 5 = 75$ unit cells, under these conditions the number of molecules: CO_2 = 6; H_2O = 558. Recall that 10^6 different conformations of the total of 564 molecules is analyzed.

Figure S13a presents the data on RDF for center-to-center distances of CO_2-H_2O, and H_2O-H_2O pairs determined from CBMC simulations for adsorption of CO_2(1)/H_2O(2) mixture adsorption in CALF-20 at 298 K with partial fugacities f_1 = 14.1 kPa, and f_2 =0.9 kPa. We note that the first peaks for both CO_2-H_2O, and H_2O-H_2O pairs occurs at distances of about 3 Å. This implies that CO_2 faces stiffer competitive adsorption with partner H_2O molecules because of the preponderance of H_2O within the framework. Observe also the snapshots in Figure S10 . This explains the fact that for $y_2 > 0.05$, the adsorbed phase mixture is poorer in CO_2 than is anticipated by the IAST.

Figure S13b presents the data on RDF for O···H distances of CO_2-H_2O, and H_2O-H_2O pairs determined from CBMC simulations for adsorption of CO_2(1)/H_2O(2) mixture adsorption in CALF-20 at 298 K with partial fugacities f_1 = 14.1 kPa, and f_2 =0.9 kPa. Strong hydrogen bonding manifests for H_2O-H_2O pairs as should be anticipated.

Figure S13c presents the data on RDF for O···H distances of H_2O-H_2O pairs determined from CBMC simulations for adsorption of CO_2(1)/H_2O(2) mixture adsorption in CALF-20 at 298 K, compared with

unary H_2O adsorption at partial fugacity 0.9 kPa. The RDFs for the two data sets overlap, implying that the degree of hydrogen bonding between pairs of water molecules is uninfluenced by the presence or absence of CO_2 molecule in their vicinity.

For further examples on the violation of the tenets of the IAST, watch the presentations titled **Dependence of Adsorption Selectivity on Mixture Composition, Hydrogen Bonding Influences on Adsorption, How Reliable is the IAST?, The Real Adsorbed Solution Theory, Co-operative Mixture Adsorption in Zeolites & MOFs, Azeotropic Adsorption, What is Azeotropic Adsorption, The Spreading Pressure Concept for Microporous Membranes**

on YouTube https://www.youtube.com/@rajamanikrishna250/videos

3.3 List of Tables for Configurational-Bias Monte Carlo (CBMC) simulations

Table S3. Lennard-Jones parameters for host atoms in CALF-20. See Figure S4 for explanation of atom names. The partial charges were provided by kind courtesy of Gopalsamy and Maurin in a personal communication to R. Krishna.[22]

atom	σ_{host} Å	$\frac{\varepsilon_{host}}{k_B}$ K	Charge	Atom count
Zn	4.045	27.680	0.6677	8
N1	3.263	38.953	-0.25823	8
N2	3.263	38.953	-0.14998	4
O	3.033	48.163	-0.51209	8
C1	3.473	47.861	0.11239	8
H	2.846	7.650	0.15033	8
C2	3.473	47.861	0.49748	4

Table S4. Dual-site Langmuir-Freundlich parameters for CO_2 and H_2O determined from fitting unary isotherms determined at 298K from CBMC simulations in CALF-20.

	Site A			Site B		
	$\frac{q_{A,sat}}{\text{mol kg}^{-1}}$	$\frac{b_A}{\text{Pa}^{-\nu_A}}$	ν_A	$\frac{q_{B,sat}}{\text{mol kg}^{-1}}$	$\frac{b_B}{\text{Pa}^{-\nu_B}}$	ν_B
CO_2 $R^2 = 0.999316$	1	4.693E-07	1	2.8	3.507E-04	1
H_2O $R^2 = 0.98238$	10.1	4.854E-29	10.5	1.3	1.888E-04	1.12

Fitted Wilson non-ideality parameters for binary CO_2/H_2O mixture adsorption at 298 K in CALF-20.

	C / kg mol^{-1}	Λ_{12}	Λ_{21}
95/5 CO_2/H_2O mixture, vary f_t	0.762	0.871	0
f_t = 15 kPa, vary y_2	0.313	0.011	0

3.4 List of Figures for Configurational-Bias Monte Carlo (CBMC) simulations

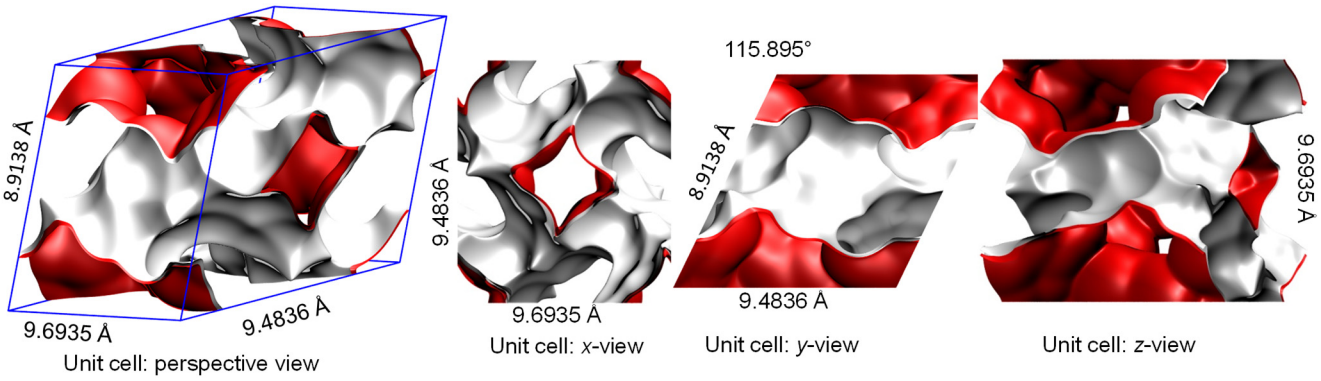

Figure S3. Unit cell of CALF-20.

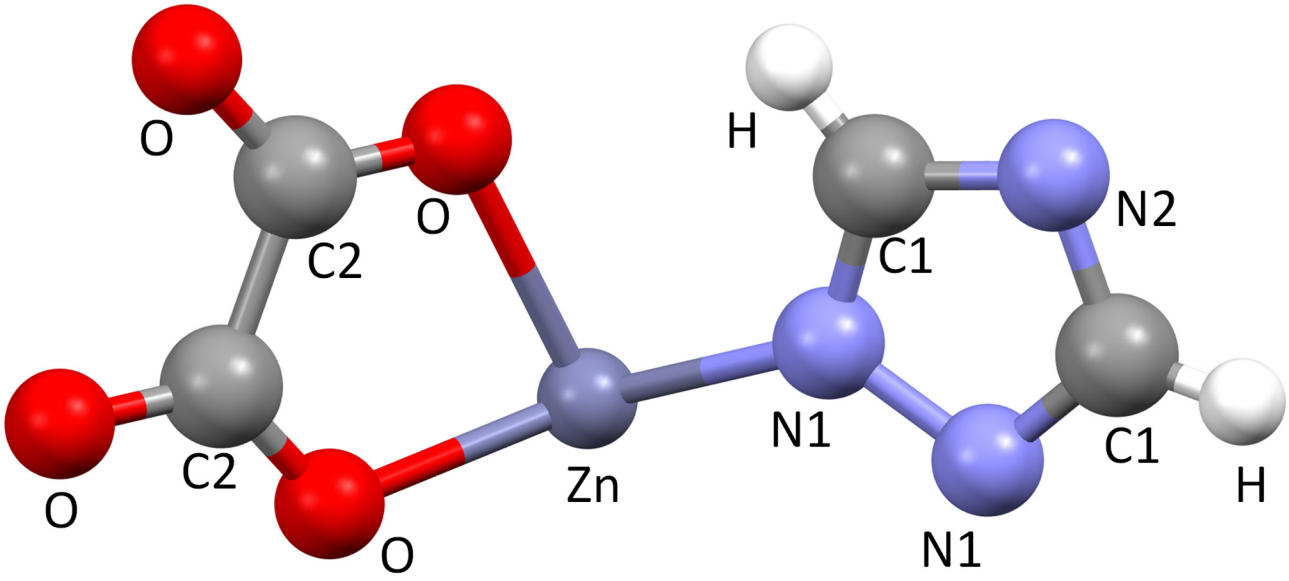

Figure S4. Atom labels used in the force field parameters for the secondary building unit (SBU) for CALF-20.

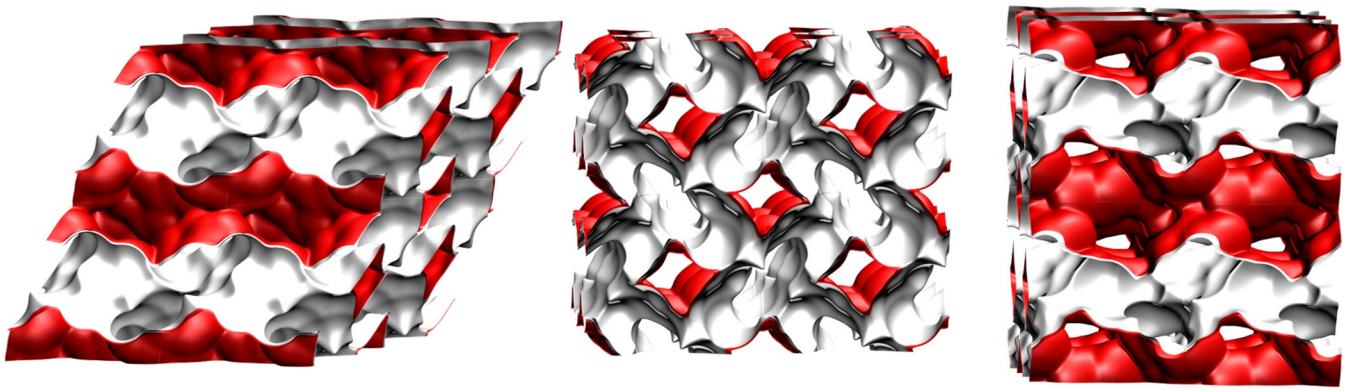

Figure S5. Pore landscapes of CALF-20.

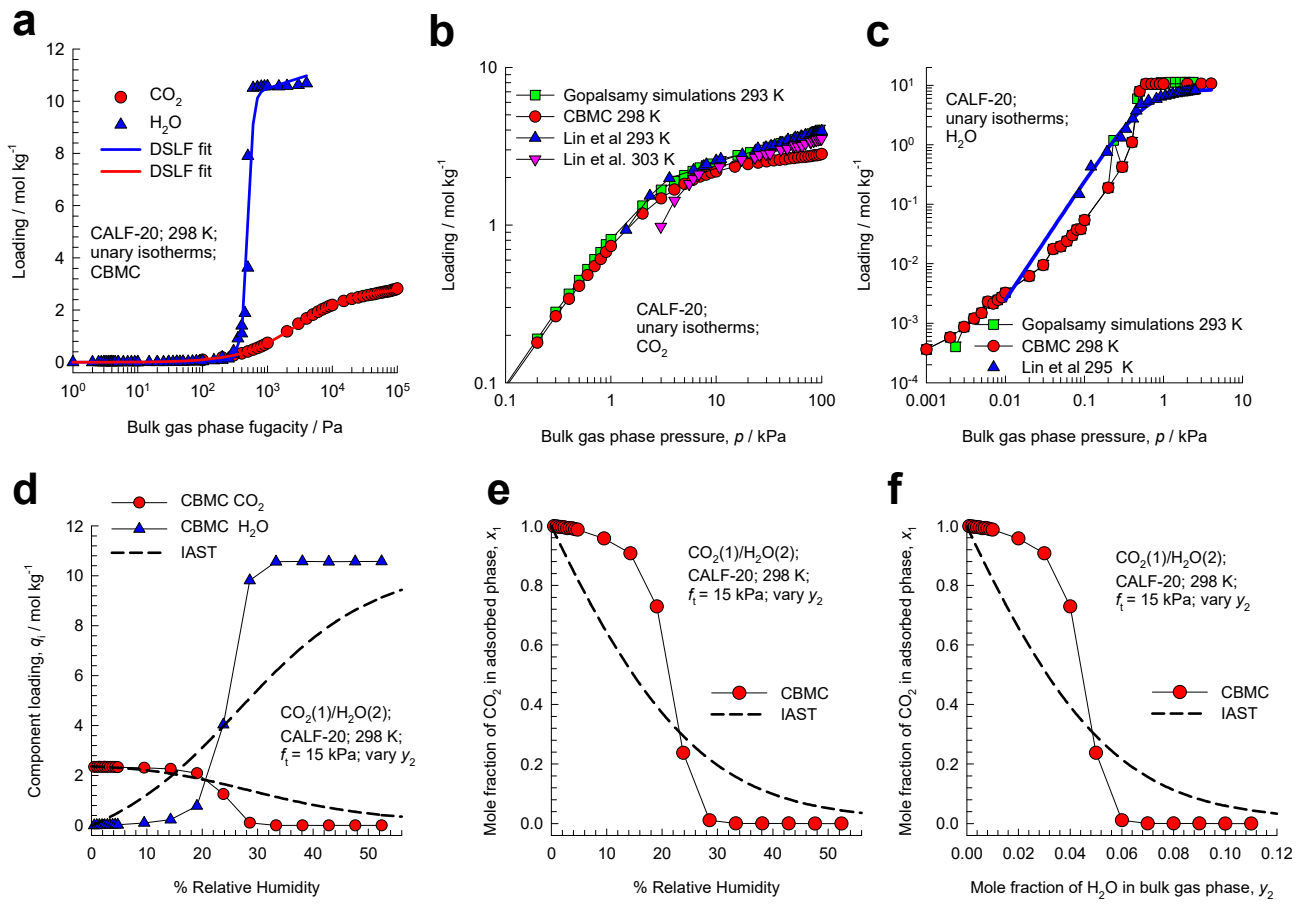

Figure S6. (a) CBMC simulations for unary CO_2 and H_2O isotherms at 298 K. The unary isotherm DSLF fit parameters are provided in Table S4. (b, c) Comparison of unary CBMC isotherm for CO_2 and H_2O isotherms at 298 K with CBMC simulations of Gopalsamy et al.[22] at 293 K. Also shown are the experimental unary isotherms for CO_2 and H_2O from Lin et al.[18] (d) CBMC simulations of component loadings, q_i, for $CO_2(1)/H_2O(2)$ mixture adsorption in CALF-20 at 298 K at a total fugacity f_t = 15 kPa, plotted as a function of $\%\text{Relative Humidity} = \frac{f_2}{p_2^{sat}} \times 100$. The mole fraction of H_2O in the bulk gas mixture, $y_2 = f_2 / f_t$, is varied. (e, f) Plot of the mole fraction of CO_2 in the adsorbed phase mixture, x_1, as a function of (e) $\%\text{Relative Humidity} = \frac{f_2}{p_2^{sat}} \times 100$, and (f) the mole fraction of H_2O in the bulk gas mixture, y_2. The dashed lines are the IAST estimations.

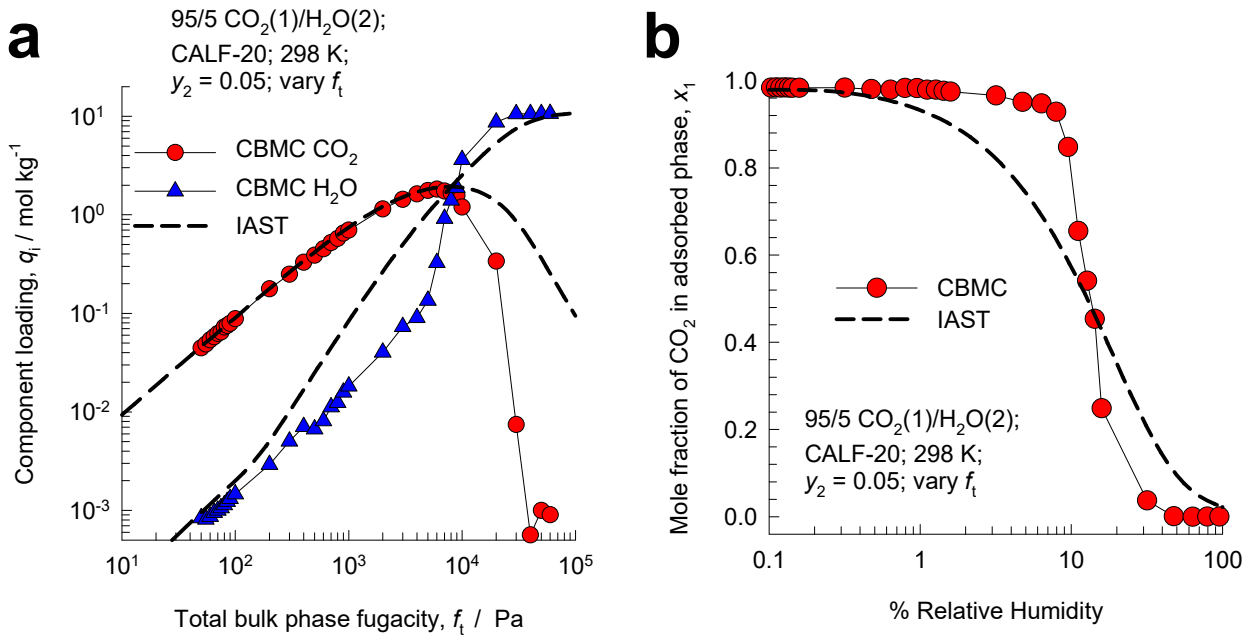

Figure S7. (a) CBMC simulations of component loadings, q_i, for $CO_2(1)/H_2O(2)$ mixture adsorption in CALF-20 at 298 K with varying total fugacity f_t, maintaining the mole fraction of H_2O in the bulk gas mixture at a constant value $y_2 = f_2/f_t = 0.05$. (b) Plot of the mole fraction of CO_2 in the adsorbed phase mixture, x_1, as a function of $\%\text{Relative Humidity} = \frac{f_2}{p_2^{sat}} \times 100$. The dashed lines are the IAST estimations; the unary isotherm DSLF fit parametes are provided in Table S4.

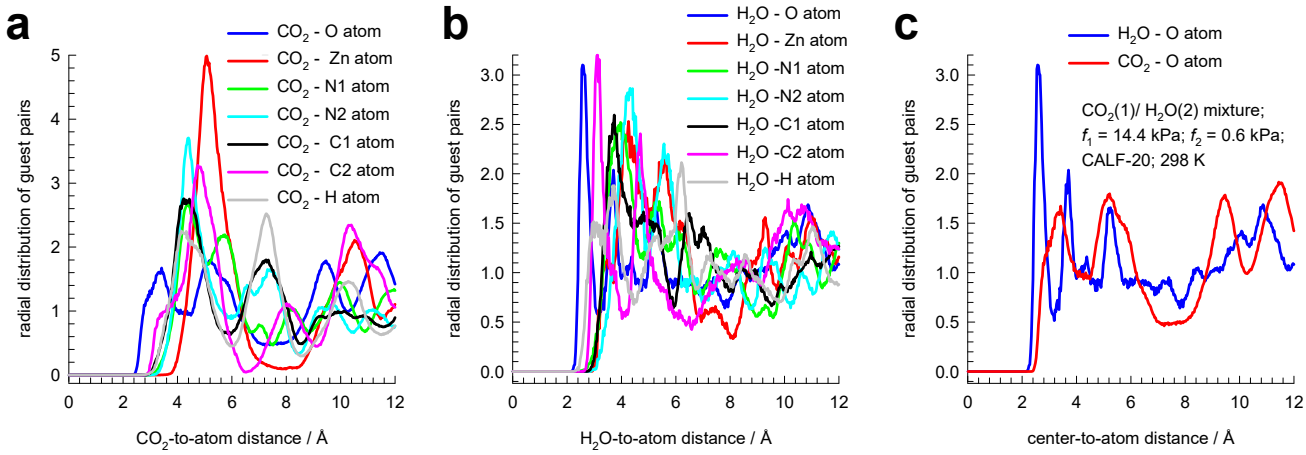

Figure S8. (a, b) Radial Distribution Function (RDF) of guest-to-framework-atom distances of (a) guest CO_2, and (b) guest H_2O for adsorption of CO_2(1)/H_2O(2) mixture adsorption in CALF-20 at 298 K. See Figure S4 and Table S3, for explanation of the labels for the framework atoms. The total fugacity in the bulk gas phase is 15 kPa with partial fugacities f_1 = 14.4 kPa, and f_2 =0.6 kPa. The plotted RDF data has been normalized such that the area under each of the curves is identical to one another. (c) Radial Distribution Function (RDF) of guest-to-oxygen atom distances of CO_2, and H_2O guests.

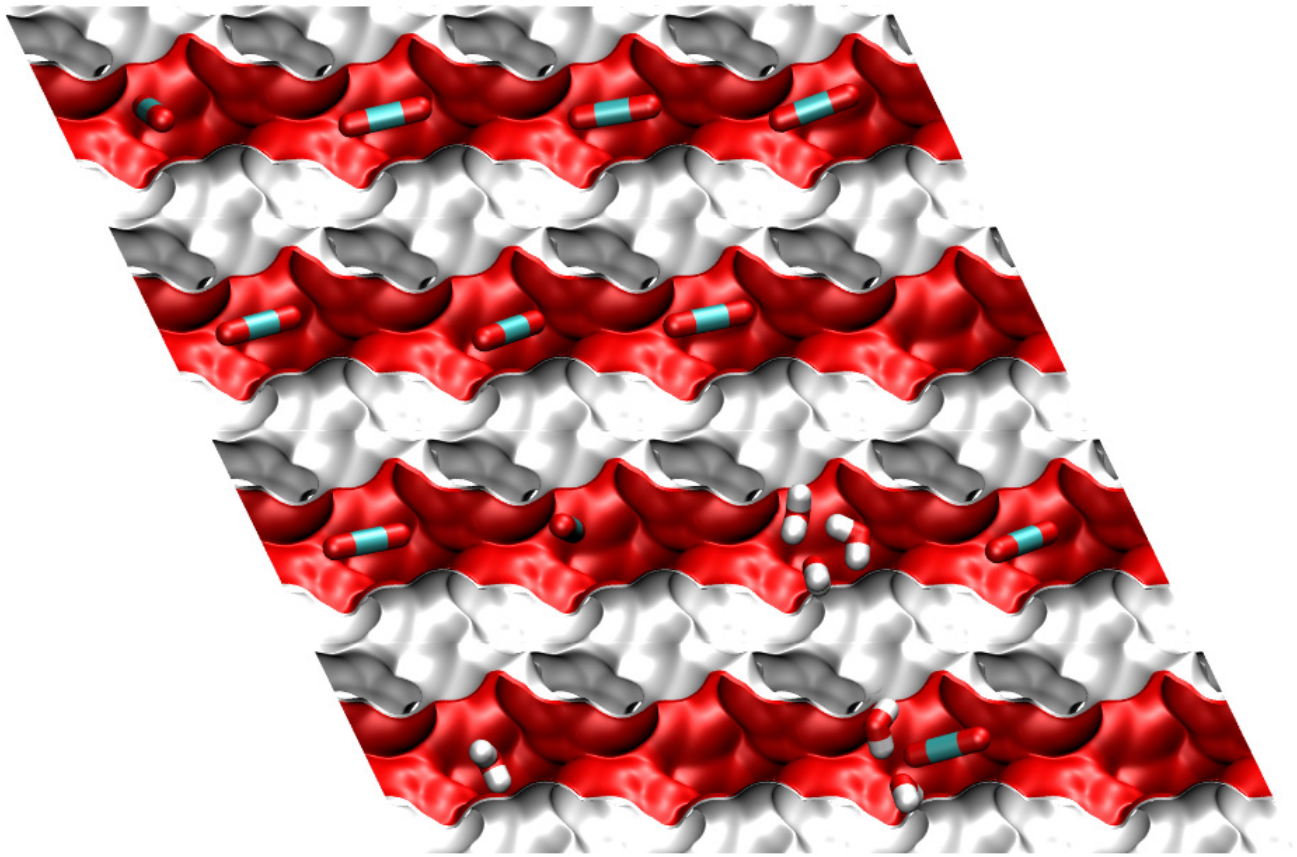

Figure S9. Computational snapshots showing the location of guests CO_2 and H_2O in CALF-20 at 298 K. The total fugacity in the bulk gas phase is 15 kPa with partial fugacities f_1 = 14.4 kPa, and f_2 =0.6 kPa.

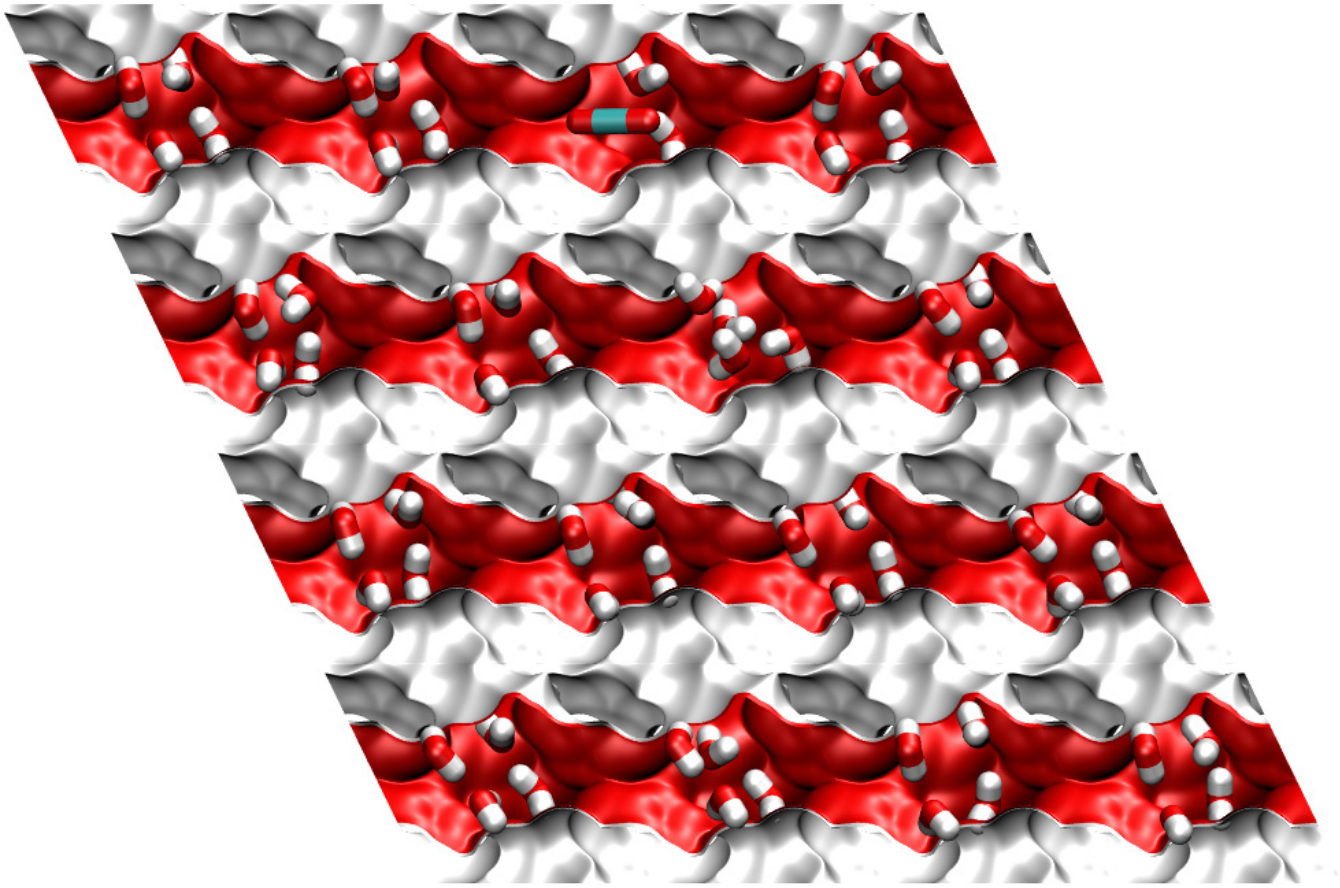

Figure S10. Computational snapshots showing the location of guests CO_2 and H_2O in CALF-20 at 298 K. The total fugacity in the bulk gas phase is 15 kPa with partial fugacities f_1 = 14.1 kPa, and f_2 =0.9 kPa.

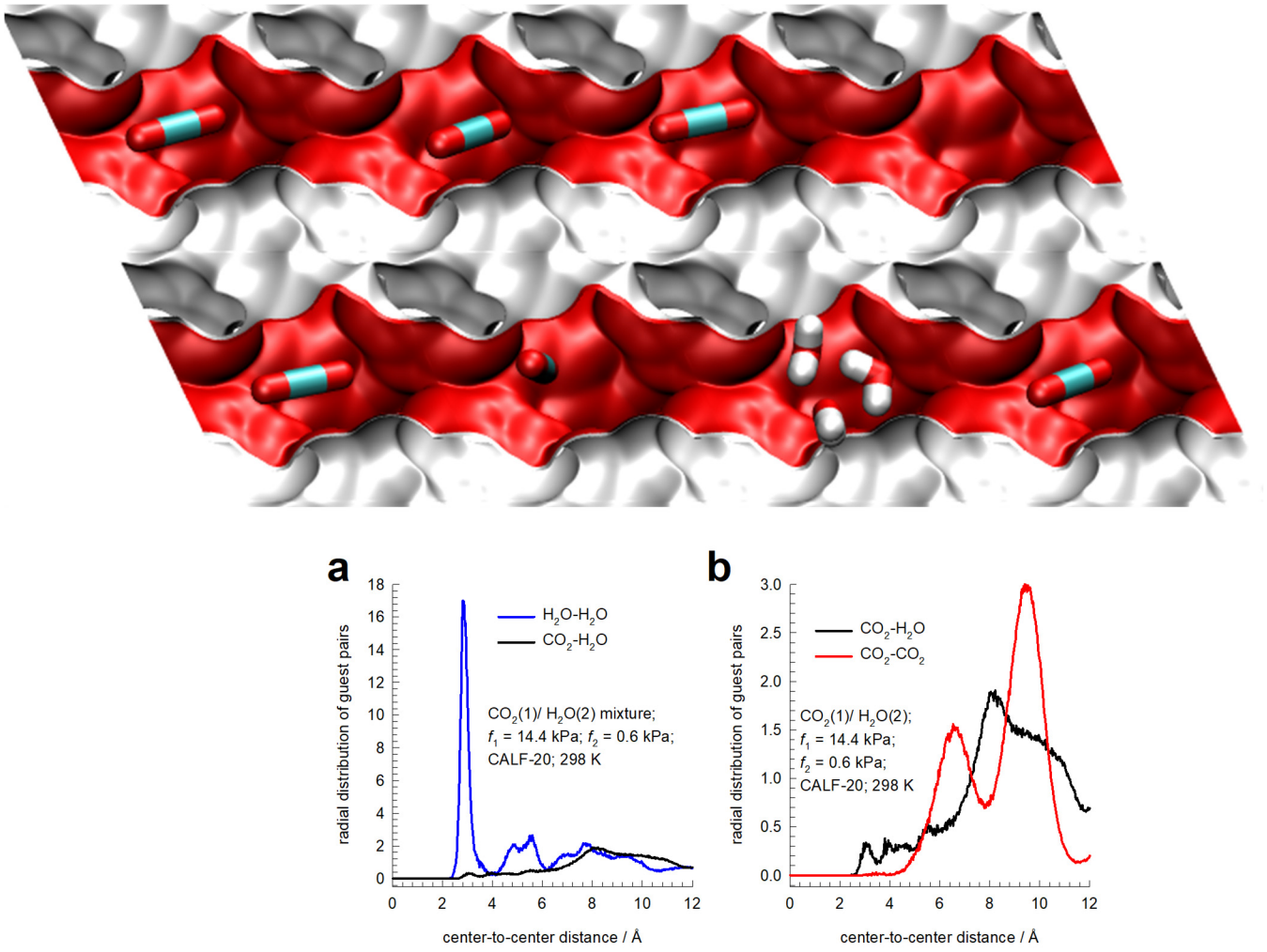

Figure S11. (a, b) Radial Distribution Function (RDF) of center-to-center distances of CO_2-CO_2, CO_2-H_2O, and H_2O-H_2O pairs determined from CBMC simulations for adsorption of CO_2(1)/H_2O(2) mixture adsorption in CALF-20 at 298 K. The total fugacity in the bulk gas phase is 15 kPa with partial fugacities f_1 = 14.4 kPa, and f_2 =0.6 kPa. The plotted RDF data has been normalized such that the area under each of the curves is identical to one another.

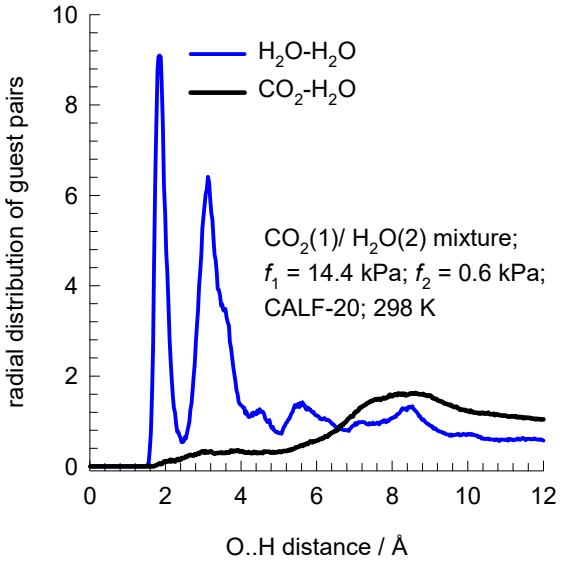

Figure S12. Radial Distribution Function (RDF) of O···H distances of H_2O-H_2O and CO_2-H_2O pairs determined from CBMC simulations for adsorption of CO_2(1)/H_2O(2) mixture adsorption in CALF-20 at 298 K. The total fugacity in the bulk gas phase is 15 kPa with partial fugacities f_1 = 14.4 kPa, and f_2 =0.6 kPa.

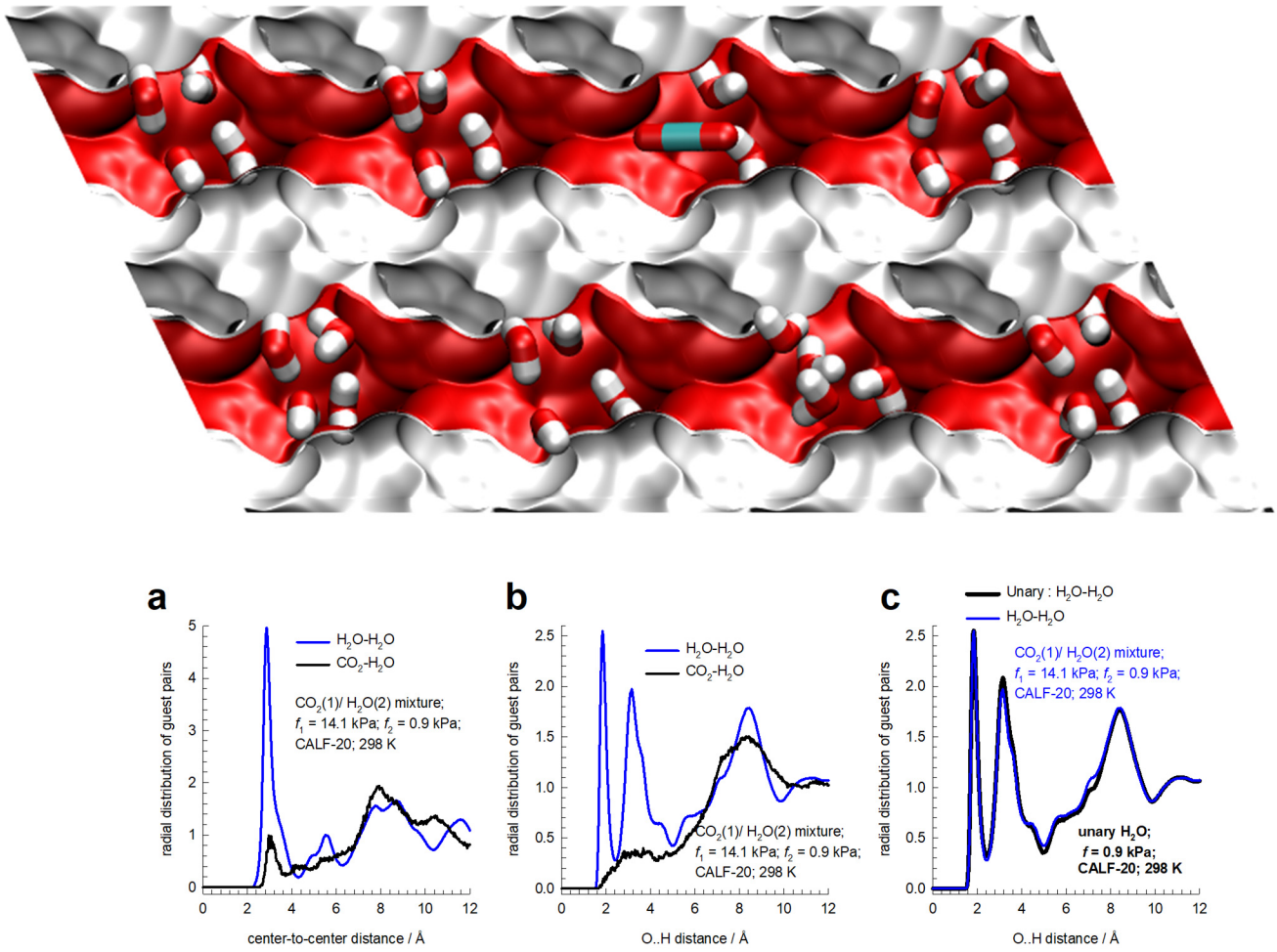

Figure S13. Radial Distribution Function (RDF) of (a) center-to-center distances, and (b) O···H of CO_2-H_2O, and H_2O-H_2O pairs determined from CBMC simulations for adsorption of CO_2(1)/H_2O(2) mixture adsorption in CALF-20 at 298 K. The total fugacity in the bulk gas phase is 15 kPa with partial fugacities f_1 = 14.1 kPa, and f_2 =0.9 kPa. (c) O···H of H_2O-H_2O pairs determined from CBMC simulations for adsorption of CO_2(1)/H_2O(2) mixture adsorption in CALF-20 at 298 K, compared with unary H_2O adsorption at partial fugacity 0.9 kPa. The plotted RDF data has been normalized such that the area under each of the curves is identical to one another.

4 The Real Adsorbed Solution Theory (RAST)

To quantify non-ideality effects in mixture adsorption, we introduce activity coefficients γ_i into eq (S3) as [2, 9, 10]

$$f_i = P_i^0 x_i \gamma_i \tag{S16}$$

Following the approaches of Myers, Talu, and Siperstein[3, 4, 36] we model the excess Gibbs free energy for binary mixture adsorption as follows

$$\frac{G^{excess}}{RT} = x_1 \ln(\gamma_1) + x_2 \ln(\gamma_2) \tag{S17}$$

For calculation of the total mixture loading $q_t = q_1 + q_2$ we need to replace eq (S10) by

$$\frac{1}{q_t} = \frac{x_1}{q_1^0(P_1^0)} + \frac{x_2}{q_2^0(P_2^0)} + \left(\frac{1}{q_t}\right)^{excess} \tag{S18}$$

The excess reciprocal loading for the mixture can be related to the partial derivative of the Gibbs free energy with respect to the surface potential at constant composition

$$\left(\frac{1}{q_t}\right)^{excess} = \left.\frac{\partial\left(\frac{G^{excess}}{RT}\right)}{\partial\Phi}\right|_{T,x} \tag{S19}$$

Models such as those of Wilson, Margules, and NRTL may be used for quantifying the dependence of the activity coefficients on the composition of the adsorbed mixture and the pore occupancy θ.

4.1 Margules model for activity coefficients

The Margules model for activity coefficients in binary liquid mixtures needs to be modified to include the influence of the pore occupancy on the activity coefficients

$$\ln(\gamma_1) = x_2^2\left(A_{12} + 2\left(A_{21} - A_{12}\right)x_1\right)\theta$$
$$\ln(\gamma_2) = x_1^2\left(A_{21} + 2\left(A_{12} - A_{21}\right)x_2\right)\theta \qquad \text{(S20)}$$

The introduction of the multiplier θ will ensure that the activity coefficients tend to unity at vanishingly small pore occupancies $\gamma_i \to 1; \quad \theta \to 0$. In view of eq (S13)

$$\ln(\gamma_1) = x_2^2\left(A_{12} + 2\left(A_{21} - A_{12}\right)x_1\right)\left(1 - \exp\left(-\frac{\Phi}{q_{sat,mix}}\right)\right)$$
$$\ln(\gamma_2) = x_1^2\left(A_{21} + 2\left(A_{12} - A_{21}\right)x_2\right)\left(1 - \exp\left(-\frac{\Phi}{q_{sat,mix}}\right)\right) \qquad \text{(S21)}$$

where the saturation capacity of the mixture $q_{sat,mix}$ is calculated using eq (S14):

$$q_{sat,mix} = \frac{1}{\frac{x_1}{q_{1,sat}} + \frac{x_2}{q_{2,sat}}}; \quad q_{i,sat} = q_{i,A,sat} + q_{i,B,sat}; \quad i = 1,2.$$

In our implementation of the RAST in this work, we adopt a somewhat simplified approach by introducing a constant C that is essentially the inverse of the saturation capacity of the mixture, $C = 1/q_{sat,mix}$, but assumed to be independent of the composition of the adsorbed phase mixture.

From eq (S13), we note that the expression for the fractional pore occupancy is $\theta = 1 - \exp\left(-\frac{\Phi}{q_{sat,mix}}\right)$.

We should therefore expect that the factor C may well be identified with the inverse of the saturation capacity of the mixture $q_{sat,mix} = \frac{1}{\frac{x_1}{q_{1,sat}} + \frac{x_2}{q_{2,sat}}}$. One approach is to estimate C by assuming

$C = \frac{x_1}{q_{1,sat}} + \frac{x_2}{q_{2,sat}}$, assuming, say, $x_1 = x_2 = 0.5$.

The Margules model we use in the RAST calculations is

$$\ln(\gamma_1) = x_2^2\left(A_{12} + 2\left(A_{21} - A_{12}\right)x_1\right)\left(1 - \exp\left(-C\Phi\right)\right)$$
$$\ln(\gamma_2) = x_1^2\left(A_{21} + 2\left(A_{12} - A_{21}\right)x_2\right)\left(1 - \exp\left(-C\Phi\right)\right) \qquad \text{(S22)}$$

In eq (S22) C is a constant with the units kg mol^{-1}. The introduction of $\left(1-\exp\left(-C\Phi\right)\right)$ imparts the correct limiting behaviors $\Phi \to 0;\quad \theta \to 0;\quad \gamma_i \to 1$ for the activity coefficients in the Henry regime, $f_t \to 0;\quad \Phi \to 0$, as the pore occupancy tends to vanishingly small values. As pore saturation conditions are approached, this correction factor tends to unity $\left(1-\exp\left(-C\Phi\right)\right)\to 1$. The Margules coefficients A_{12}, A_{21} may assume either positive or negative values. The choice of $A_{12} = A_{21} = 0$ in eq (S22), yields unity values for the activity coefficients. We note, in passing, that this correction factor $\left(1-\exp\left(-C\Phi\right)\right)$ is often ignored in the RAST implementations in some published works.[19, 37-39]

For calculation of the total mixture loading $q_t = q_1 + q_2$ we need to replace eq (S10) by

$$\frac{1}{q_t} = \frac{x_1}{q_1^0(P_1^0)} + \frac{x_2}{q_2^0(P_2^0)} + x_1 x_2 \left[A_{12}x_2 + A_{21}x_1\right] C\exp\left(-C\Phi\right) \tag{S23}$$

4.2 Wilson model for activity coefficients

The Wilson model for activity coefficients are given for binary mixtures by

$$\begin{aligned}
\ln(\gamma_1) &= \left(1-\ln(x_1\Lambda_{11}+x_2\Lambda_{12}) - \frac{x_1\Lambda_{11}}{x_1\Lambda_{11}+x_2\Lambda_{12}} - \frac{x_2\Lambda_{21}}{x_2+x_1\Lambda_{21}}\right)\left(1-\exp\left(-C\Phi\right)\right) \\
\ln(\gamma_2) &= \left(1-\ln(x_1\Lambda_{21}+x_2\Lambda_{22}) - \frac{x_1\Lambda_{12}}{x_1\Lambda_{11}+x_2\Lambda_{12}} - \frac{x_2\Lambda_{22}}{x_1\Lambda_{21}+x_2\Lambda_{22}}\right)\left(1-\exp\left(-C\Phi\right)\right)
\end{aligned} \tag{S24}$$

In Eq (S24), $\Lambda_{11} \equiv 1;\quad \Lambda_{22} \equiv 1$, and C is a constant with the units kg mol^{-1}. The choice of $\Lambda_{12} = \Lambda_{21} = 1$ in Eq (S24), yields unity values for the activity coefficients.

The excess reciprocal loading for the mixture can be related to the partial derivative of the Gibbs free energy with respect to the surface potential at constant composition

$$\left(\frac{1}{q_t}\right)^{excess} = \left.\frac{\partial\left(\frac{G^{excess}}{RT}\right)}{\partial\Phi}\right|_{T,x} = \left[-x_1\ln(x_1+x_2\Lambda_{12}) - x_2\ln\left(x_2+x_1\Lambda_{21}\right)\right] C\exp\left(-C\Phi\right) \tag{S25}$$

For calculation of the total mixture loading we need to replace Eq (S10) by

$$\frac{1}{q_t} = \frac{x_1}{q_1^0(P_1^0)} + \frac{x_2}{q_2^0(P_2^0)} + \left[-x_1 \ln(x_1 + x_2\Lambda_{12}) - x_2 \ln\left(x_2 + x_1\Lambda_{21}\right)\right] C \exp\left(-C\Phi\right) \quad \text{(S26)}$$

The parameters C; Λ_{12}; Λ_{21} are fitted to match the experimental or CBMC data on mixture adsorption.

The implementation of the activity coefficients is termed as the Real Adsorbed Solution Theory (RAST).

With the introduction of activity coefficients, the expression for the adsorption selectivity for binary mixtures is

$$S_{ads} = \frac{q_1/q_2}{y_1/y_2} = \frac{q_1/y_1}{q_2/y_2} = \frac{x_1/f_1}{x_2/f_2} = \frac{P_2^0\gamma_2}{P_1^0\gamma_1} \quad \text{(S27)}$$

Since the activity coefficients are composition dependent, the adsorption selectivity is also composition dependent, and S_{ads} is not uniquely related to the surface potential, Φ.

For further details of the RAST calculations and the need for inclusion of the $\left(1-\exp\left(-C\Phi\right)\right)$ correction factor watch the presentations titled **Dependence of Adsorption Selectivity on Mixture Composition, Hydrogen Bonding Influences on Adsorption, How Reliable is the IAST?, The Real Adsorbed Solution Theory, Co-operative Mixture Adsorption in Zeolites & MOFs, Azeotropic Adsorption, What is Azeotropic Adsorption, Water/Alcohol Azeotropic Adsorption, Segregation and Congregation Effects in CO_2 capture, Thermodynamic Non=Idealities in CO_2 capture, CO_2 capture with CALF-20**

on YouTube https://www.youtube.com/@rajamanikrishna250/videos

4.3 RAST modelling of CO_2/H_2O adsorption in CALF-20

In order to highlight the need for including the correction factor $\left(1-\exp\left(-C\Phi\right)\right)$, we analyze the Configurational-Bias Monte Carlo (CBMC) simulations presented earlier in Figure S7 for CO_2(1)/H_2O(2)

mixture adsorption in CALF-20 at 298 K for varying total fugacity f_t, maintaining the mole fraction of H_2O in the bulk gas mixture at a constant value $y_2 = f_2/f_t = 0.05$.

The mole fractions of the adsorbed phase, $x_1 = \frac{q_{1,CBMC}}{q_{t,CBMC}}; x_2 = \frac{q_{2,CBMC}}{q_{t,CBMC}}; q_{t,CBMC} = q_{1,CBMC} + q_{2,CBMC}$ are determined. The sorption pressures P_1^0, P_2^0, each of which satisfying eq (S5), can be determined from using the unary isotherm fits for each of the components in the binary mixture.

The activity coefficients of the two components $\gamma_{1,CBMC}; \gamma_{2,CBMC}$ are determined from eq (S16):

$$\gamma_{1,CBMC} = \frac{f_1}{P_1^0 x_{1,CBMC}}; \gamma_{2,CBMC} = \frac{f_2}{P_2^0 x_{2,CBMC}} \tag{S28}$$

The set of three Wilson parameters C; Λ_{12}; Λ_{21} that yield the minimum value for the objective function calculated as the sum of the mean-squared deviations between the CBMC simulated component loadings, and those predicted using RAST

$$\text{Objective Function} = \sum \left(q_{1,CBMC} - q_{1,RAST} \right)^2 + \left(q_{2,CBMC} - q_{2,RAST} \right)^2 \tag{S29}$$

The values of the fitted Wilson parameters C; Λ_{12}; Λ_{21} are tabulated in Table S4. The continuous solid lines in Figure S14 are the RAST model calculations with these Wilson parameters; the agreement with the CBMC data (indicated by symbols) is excellent as should be expected.

Also noteworthy is that the activity coefficients $\gamma_i \to 1$ as the surface potential Φ attains vanishingly small values, $\Phi \to 0$; see Figure S14b. Such limiting behaviors can only be captured by inclusion of the correction $\left(1 - \exp\left(-C\Phi\right)\right)$ in the RAST modelling. It is noteworthy that the correction factor $\left(1 - \exp\left(-C\Phi\right)\right)$ has been omitted in the RAST implementation of Kaur and Marshall.[19]

Figure S15a,b,c compares RAST model calculations with fitted Wilson parameters, tabulated in Table S4, with the CBMC simulations for CO_2(1)/H_2O(2) mixture adsorption in CALF-20 at 298 K at a total fugacity f_t = 15 kPa, varying the mole fraction of H_2O in the bulk gas mixture, $y_2 = f_2/f_t$, is varied. The agreement with the CBMC data (indicated by symbols) is excellent as should be expected. Figure S15d

plots the activity coefficients in the adsorbed phase mixture, γ_i, as a function of the mole fraction of CO_2 in the adsorbed phase mixture, x_1.

Figure S16a compares the RAST model, with fitted Margules parameters specified in Table S2 with the molecular simulations data of Gopalsamy et al.[22] for CO_2(1)/H_2O(2) mixture adsorption in CALF-20 at 293 K. The match between RAST and molecular simulations is good, as should be expected. The corresponding experimental data on the adsorbed phase CO_2 mole fraction is compared with the RAST and IAST estimations in Figure S16c.

Figure S16b compares the RAST model, with fitted Margules parameters specified in Table S1, with the component loadings were determined from breakthrough experiments in structured CALF-20 (80% MOF:20% polysulfone).[18-21]

The RAST calculations for the component loadings for CO_2/H_2O mixture adsorption in structured CALF-20, determined from breakthrough experiments, are indicated by the continuous solid lines in Figure S16b. For %RH = 73%, and 87%, the experimental H_2O loadings for mixture adsorption are in excess of the unary loadings; this characteristic cannot be modeled using the RAST. Noteworthily, RAST implementations of Kaur and Marshall,[19] using either the NRTL or Margules models also experience similar limitations at high values of %RH.

The corresponding experimental data on the adsorbed phase CO_2 mole fraction is compared with the RAST and IAST estimations in Figure S16d.

4.4 List of Figures for The Real Adsorbed Solution Theory (RAST)

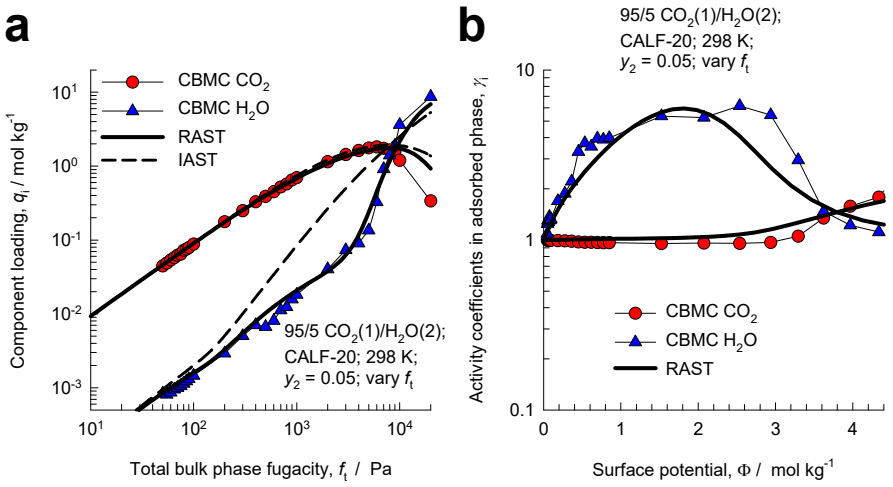

Figure S14. (a) CBMC simulations of component loadings, q_i, for $CO_2(1)/H_2O(2)$ mixture adsorption in CALF-20 at 298 K with varying total fugacity f_t, maintaining the mole fraction of H_2O in the bulk gas mixture at a constant value $y_2 = f_2/f_t = 0.05$. (b) Plot of the activity coefficients in the adsorbed phase mixture, γ_i, as a function of the surface potential Φ. The continuous solid lines are the RAST calculations; for this purpose the unary isotherm fits used are those provided in Table S4. The dashed lines are the IAST estimations.

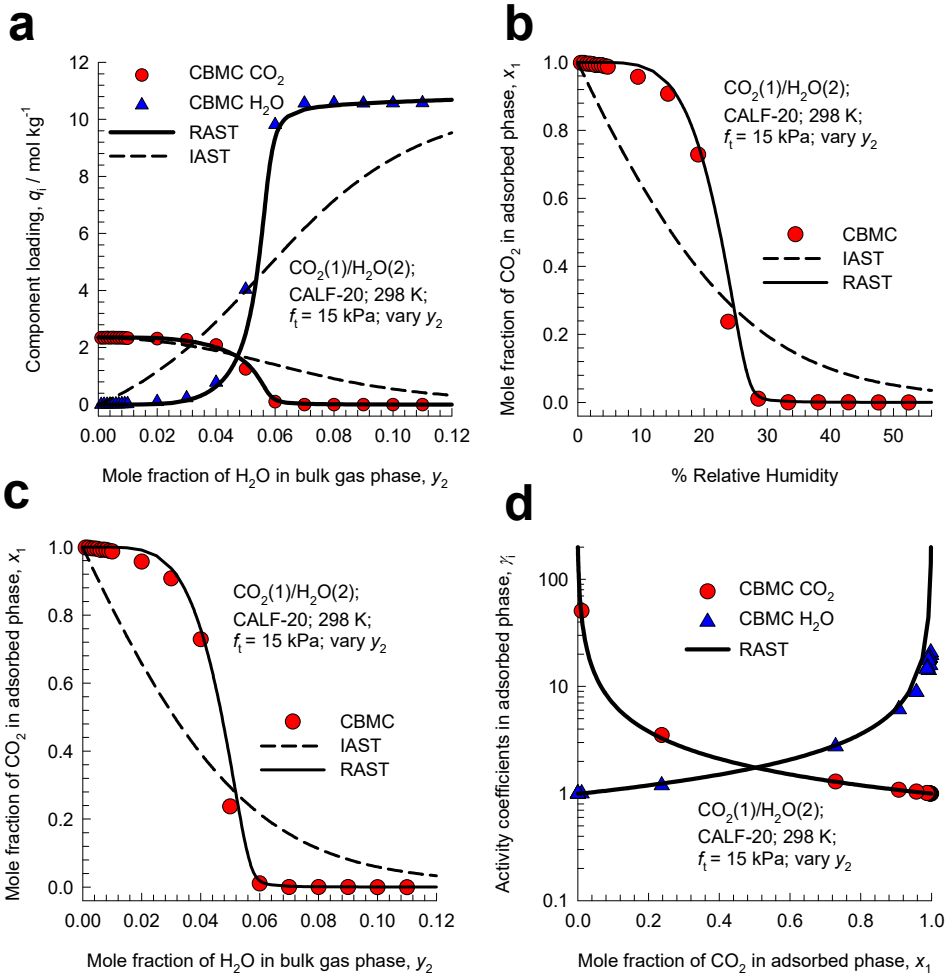

Figure S15. (a) CBMC simulations of component loadings, q_i, for CO2(1)/H2O(2) mixture adsorption in CALF-20 at 298 K at a total fugacity f_t = 15 kPa, plotted as a function of %Relative Humidity $= \frac{f_2}{p_2^{sat}} \times 100$. The mole fraction of H2O in the bulk gas mixture, $y_2 = f_2 / f_t$, is varied. (b, c) Plot of the mole fraction of CO2 in the adsorbed phase mixture, x_1, as a function of (b) %Relative Humidity $= \frac{f_2}{p_2^{sat}} \times 100$, and (c) the mole fraction of H2O in the bulk gas mixture, y_2. (d) Plot of the activity coefficients in the adsorbed phase mixture, γ_i, as a function of the mole fraction of CO2 in the adsorbed phase mixture, x_1, The continuous solid lines are the RAST calculations; the inputs are provided in Table S4. The dashed lines are the IAST estimations.

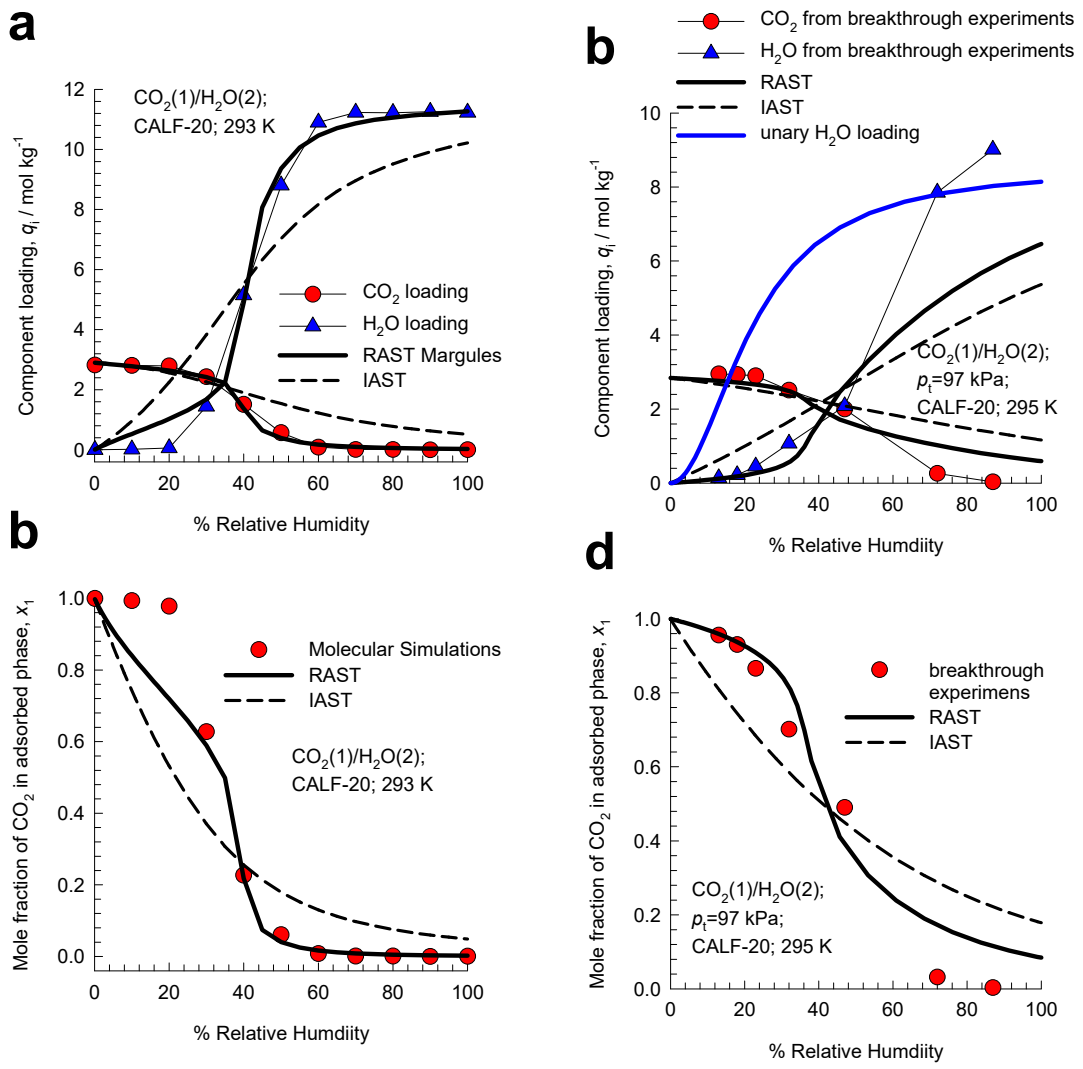

Figure S16. (a, c) Molecular simulation data of Gopalsamy et al.[22] (indicated by symbols) on (a) component loadings, (c) adsorbed phase CO_2 mole fraction for $CO_2(1)/H_2O(2)$ mixture adsorption in CALF-20 at 293 K. The continuous solid lines are the RAST estimations; for this purpose the unary isotherm fits and Margules parameters used are those provided in Table S2. (b, d) Experimental data of Lin et al.[18] (indicated by symbols) on (b) component loadings, (d) adsorbed phase CO_2 mole fraction for $CO_2(1)/H_2O(2)$ mixture adsorption in structured CALF-20 (80% MOF:20% polysulfone) at 295 K. The total pressure in the bulk gas phase is 97 kPa with varying % relative humidity. The continuous solid lines are the RAST estimations; for this purpose, the unary isotherm fits and Margules parameters used are those provided in Table S1.

5 Modelling Experimental CO_2/H_2O Breakthroughs

Nguyen et al. [21] have presented experimental data on the influence of %Relative Humidity on transient breakthroughs in a laboratory scale fixed bed. In order to demonstrate that the experimental breakthroughs are strongly influenced by thermodynamic non-idealities for the reasons described in the foregoing Chapters, we undertake transient breakthrough simulations of their experiments.

We summarize below the simulation methodology used to perform transient breakthrough calculations for fixed bed adsorbers. The simulation methodology is the same as described by Krishna. [40-43] In an *n*-component gas mixtures in plug flow through a fixed bed maintained under isothermal conditions, the molar concentrations in the gas phase at any position and instant of time are obtained by solving the following set of partial differential equations for each of the species *i* in the gas mixture

$$\frac{\partial c_i(t,z)}{\partial t}+\frac{\partial\left(v(t,z)c_i(t,z)\right)}{\partial z}+\frac{\left(1-\varepsilon\right)}{\varepsilon}\rho\frac{\partial \bar{q}_i(t,z)}{\partial t}=0;\quad i=1,2,...n \tag{S30}$$

In eq (S30), t is the time, z is the distance along the adsorber, ρ is the framework density, ε is the bed voidage, v is the interstitial gas velocity, and $\bar{q}_i(t,z)$ is the *spatially averaged* molar loading within the crystallites of radius r_c, monitored at position z, and at time t. At time, $t = 0$, the inlet to the adsorber, $z = 0$, is subjected to a step input of the *n*-component gas mixture and this step input is maintained till the end of the adsorption cycle when steady-state conditions are reached.

$$t\geq 0;\quad p_i(0,t)=p_{i0};\quad u(0,t)=u_0 \tag{S31}$$

The *interstitial* gas velocity is related to the *superficial* gas velocity by

$$v=\frac{u}{\varepsilon} \tag{S32}$$

where $u_0=v\varepsilon$ is the superficial gas velocity at the inlet to the adsorber. The superficial gas velocity is calculated from the flow rate of the gas mixture entering the breakthrough tube.

The radial distribution of molar loadings, q_i, within a ZIF-8 crystallite, of radius r_c, is obtained from a solution of a set of differential equations describing the uptake

$$\rho \frac{\partial q_i(r,t)}{\partial t} = -\frac{1}{r^2}\frac{\partial}{\partial r}\left(r^2 N_i\right) \tag{S33}$$

The intra-crystalline fluxes N_i in eq (S33) are related to gradients in the molar gradients of the loadings [28, 29, 40, 44]

$$N_i = -\rho Đ_i \frac{\partial q_i}{\partial r}; \qquad i = 1,2,..n \tag{S34}$$

In eqs (S33) and (S34), R is the gas constant, T is the temperature, ρ represents the framework density of the microporous crystalline material, r is the radial distance coordinate, and the component loadings q_i are defined in terms of moles per kg of framework. The $Đ_i$ characterize and quantify the interaction between species i and pore walls. The M-S diffusivity $Đ_i$ equals the corresponding diffusivity for a unary system, determined at the same pore occupancy.[44] Furthermore, the M-S diffusivity $Đ_i$ for any species i in a mixture remains invariant to choice of the partner(s) species.[44]

At any time, t, during the transient approach to thermodynamic equilibrium, the spatial-averaged component loading within the crystallites of radius r_c is calculated using

$$\bar{q}_i(t) = \frac{3}{r_c^3}\int_0^{r_c} q_i(r,t) r^2 dr \tag{S35}$$

Summing eq (S35) over all n species in the mixture allows calculation of the *total average* molar loading of the mixture within a ZIF-7 crystallite

$$\bar{q}_t(t,z) = \sum_{i=1}^{n} \bar{q}_i(t,z) \tag{S36}$$

The term $\frac{\partial \bar{q}_i(t,z)}{\partial t}$ in eq (S30) is determined by solving the set of eqs (S33), (S34), (S35), and (S36). At any time t, and position z, the component loadings at the outer surface of the particle $q_i(r_c,t,z)$ is in equilibrium with the bulk phase gas mixture with partial pressures $p_i(t,z)$ in the bulk gas mixture. the component loadings at the surface of the crystallites $q_i(r_c,t,z)$ where r_c is the radius of the crystallites are

calculated using the RAST. To demonstrate the influence of thermodynamic non-idealities, we also perform simulations using the IAST.

In the simulations, the value of $Đ_i/r_c^2$ is assumed to be large enough to ensure that intra-crystalline gradients are absent and the entire crystallite particle can be considered to be in thermodynamic equilibrium with the surrounding bulk gas phase at that time *t*, and position *z* of the adsorber

$$\bar{q}_i(t,z) = q_i(t,z) \tag{S37}$$

Further details of the numerical procedures used in solving the partial differential equations, are provided by Krishna and co-workers.[40-43] For further explanation, including video animations of breakthroughs, watch the presentations titled **Diffusional Influences on Breakthroughs, Transient Breakthrough Simulations, Modeling of Fixed Bed Adsorbers** on YouTube https://www.youtube.com/@rajamanikrishna250/videos

We describe below the details of the experimental set-up used by Nguyen et al.[21]

Inside diameter of tube: d = 28.2 mm

Effective length of packed column: L = 78.6 mm

The mass of the CALF-20 composite in the packed tube: m_{ads} = 16.7 g

The particle density of CALF-20 composite ρ = 570 kg m^{-3}.

In Figure 9a,b,c of Nguyen et al. [21] the breakthrough experimental results are presented. The total pressure of feed gas mixture, p_t = 97 kPa. The experiments were carried out with the values %Relative Humidity = 87%, 73%, 47%, 32%, 23%, 18%, and 13%. Figure 9c of Nguyen et al.[21] presents the transient development of temperatures during breakthrough experiments. During a short initial time interval $30 < \tau = \frac{tv}{L} < 100$, temperature peaks are observed, but for the large majority of the breakthrough time interval $100 < \tau = \frac{tv}{L} < 40\times10^3$ essentially isothermal conditions prevail, and T = 295 K. Indeed, the breakthrough experimental data on the equilibrated component loadings in the adsorbed phase as presented in Figure 11 of Nguyen et al.[21] are reported as being at a "constant" temperature of 295 K. For

these reasons, the assumption of isothermal conditions is invoked in our breakthrough simulations taking the temperature as being constant at 295 K.

At 295 K, p_2^{sat} is determined from the Antoine equation: $p_2^{sat} = 2628$ Pa . The partial pressures of H_2O in the feed mixture is calculated using $\%\text{Relative Humidity} = \frac{p_2}{p_2^{sat}} \times 100$.

The total flow rate of the gas mixture at the entrance to the tube Q_0 = 10 mL min^{-1}.

The parameters in the breakthrough simulations of the experiments are determined as follows: $(1-\varepsilon) = \frac{m_{ads}/\rho}{\pi d^2 L/4}$ and $\varepsilon = 1 - \frac{m_{ads}/\rho}{\pi d^2 L/4}$.

The superficial gas velocity at the inlet to the adsorber $u = \frac{Q_0}{\pi d^2/4}$.

The interstitial velocity $v = \frac{u}{\varepsilon}$. The unary isotherm fits are as specified in Table S1. For description of thermodynamic non-idealities, we use a set of Margules parameters as specified in Table S1: $C = 0.05$ kg mol^{-1}; $A_{12} = 1.962$; $A_{21} = 4.836$.

Figure S17 compares breakthrough simulations using RAST (continuous colored lines) and IAST (dashed lines) for CO_2/H_2O mixtures with seven different values of $\%\text{Relative Humidity}$; the dimensionless concentrations, c_i/c_{i0} are plotted as function of the dimensionless time, $\tau = \frac{tv}{L}$. Even a visual inspection reveals that there are two scenarios prevalent: (i) 32% < %RH < 13%, and (ii) 87% < %RH < 32%.

Figure S18a,b present calculations of mole fraction of CO_2, and $\%\text{Relative Humidity}$ of the gas mixture exiting the fixed bed determined from the breakthrough simulations with the RAST implementation, along with experimental breakthroughs (indicated by symbols), as reported in Figure 9a,b of Nguyen et al. [21] The agreement between simulations and experiment is good for %RH = 13, 18, 23, 32, 47. For %RH = 73 and 87, the agreement is poorer because at these high humidity values, the RAST is unable to capture equilibrated uptakes as witnessed also in Figure S16b,d.

Figure S19 presents a comparison of the RAST breakthrough simulations with the corresponding breakthroughs determined from the assumption of IAST for mixture adsorption equilibrium.

Figure S19c,d present the corresponding calculations of mole fraction of CO_2, and %Relative Humidity of the gas mixture exiting the fixed bed determined from the breakthrough simulations with the IAST implementation. Even a visual inspection of the IAST simulation results will lead us to conclude that these simulations do not reflect the experimental breakthroughs even in a quantitative manner.

Figure S20a compares the component uptakes determined from breakthrough simulations using RAST and IAST for $CO_2(1)/H_2O(2)$ mixture adsorption equilibrium in structured CALF-20 (80% MOF:20% polysulfone) at 295 K. The results are analogous to those presented in Figure S16b providing validation of the breakthrough simulation methodology. Figure S20b compares the adsorbed phase CO_2 mole fraction, y_1, breakthrough simulations using RAST and IAST. These results are directly comparable to those presented in Figure S16b.

5.1 List of Figures for Modelling Experimental CO2/H2O Breakthroughs

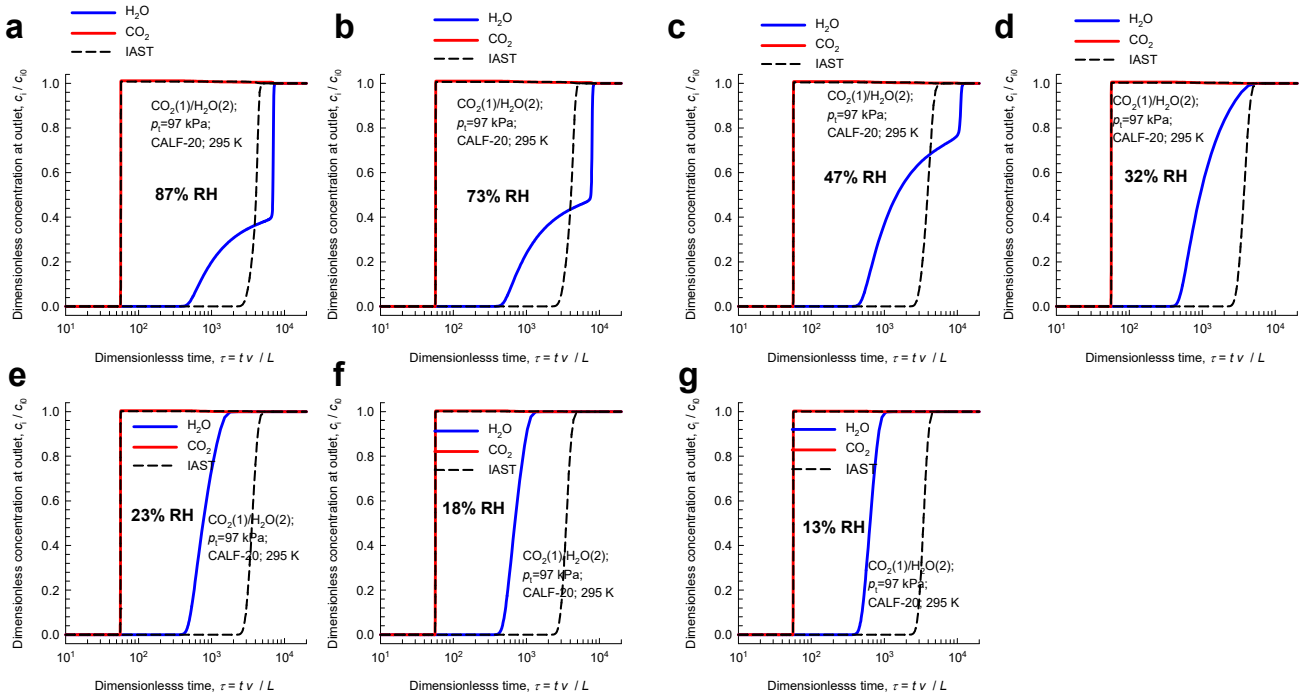

Figure S17. Comparison of breakthrough simulations using RAST (continuous colored lines) and IAST (dashed lines) for CO_2/H_2O mixtures at a total pressure = 97 kPa, and temperature 295 K. seven different values of %Relative Humidity are considered.

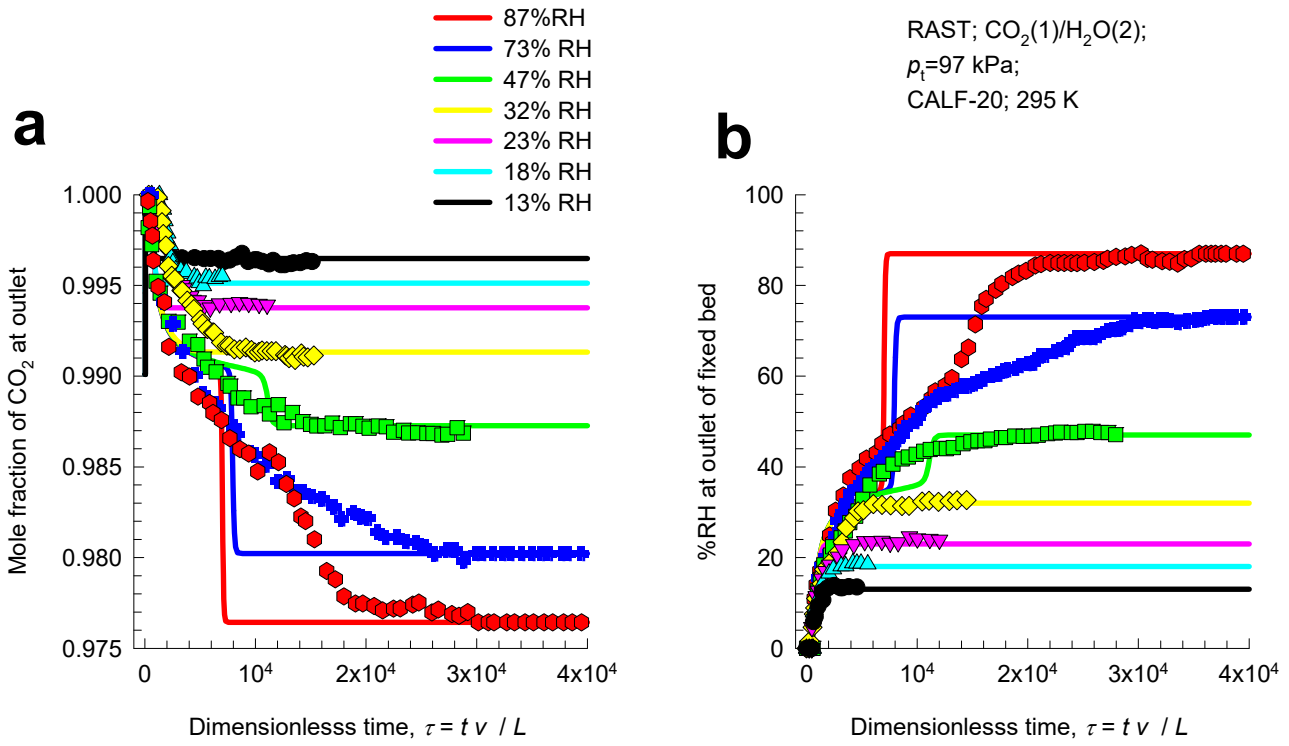

Figure S18. Comparison of (a) mole fraction of CO_2, and (b) %Relative Humidity of the gas mixture exiting the fixed bed determined from the RAST breakthrough simulations (continuous solid lines) and experimental breakthroughs (indicated by symbols) of Nguyen et al.[21]

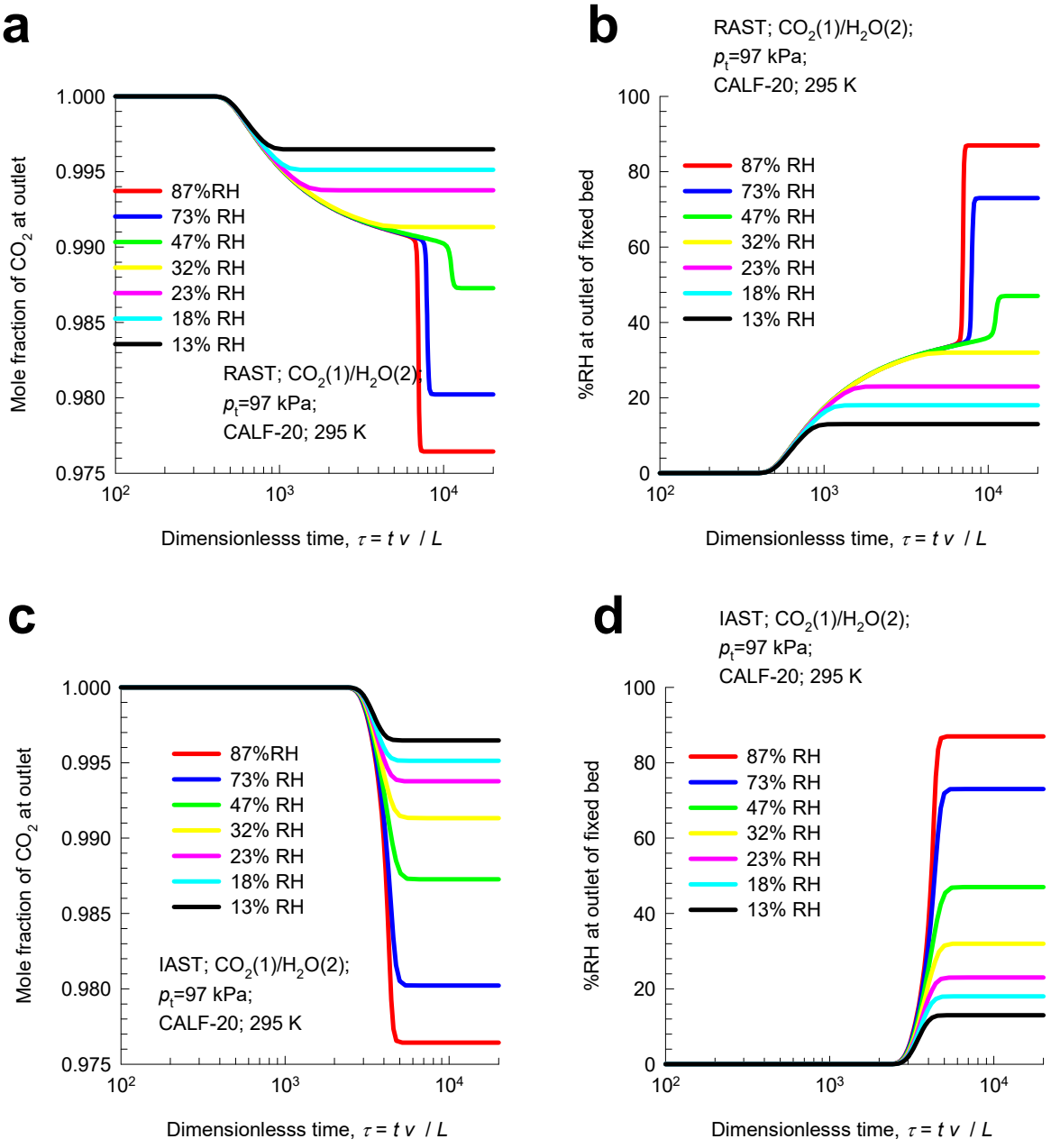

Figure S19. Comparison of (a, c) mole fraction of CO_2, and (b, d) %Relative Humidity of the gas mixture exiting the fixed bed determined from the breakthrough simulations using (a, b) RAST and (c, d) IAST.

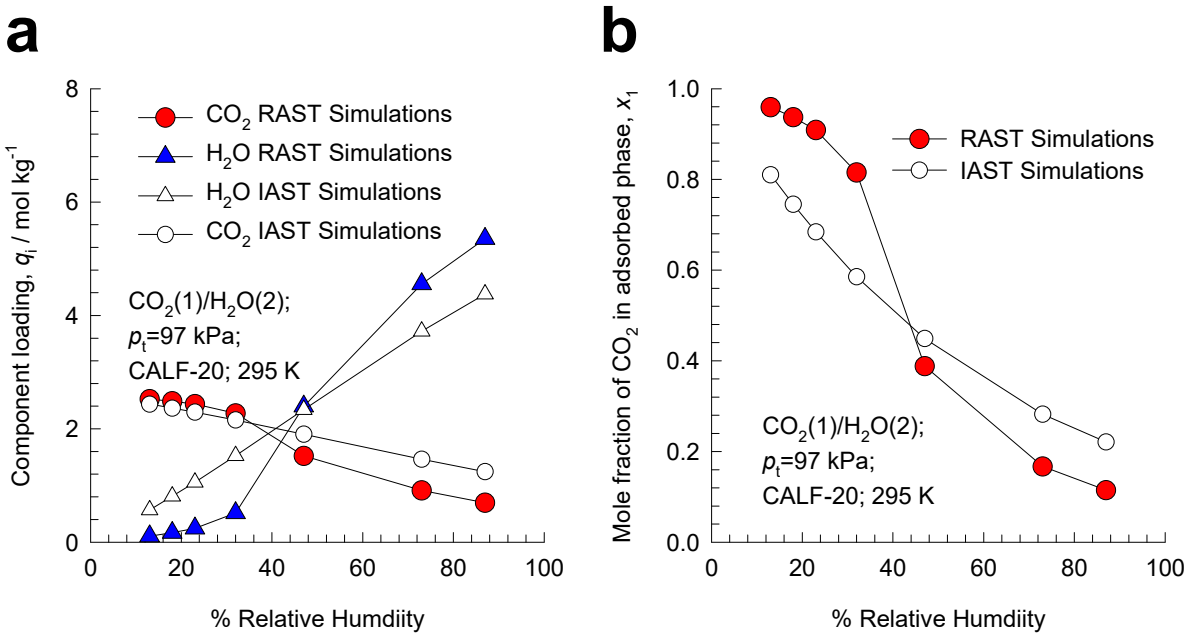

Figure S20. Comparison of the (a) component loadings and (b) adsorbed phase CO_2 mole fraction, determined from breakthrough simulations using RAST and IAST for $CO_2(1)/H_2O(2)$ mixture adsorption equilibrium in structured CALF-20 (80% MOF:20% polysulfone) at 295 K. The total pressure in the bulk gas phase is 97 kPa with varying % relative humidity. The unary isotherm fits and Margules parameters used are those provided in Table S1.

6 CBMC for CO_2/N_2 and N_2/H_2O Mixture Adsorption

CBMC simulations were also undertaken to investigate adsorption of $CO_2(1)/N_2(2)$, and $N_2(1)/H_2O(2)$ mixtures at 298 K in CALF-20. The CBMC simulations for unary isotherms for N_2 at 298 K are fitted with excellent accuracy using the single-site Langmuir model; the fit parameters are provided in Table S5. Figure S21a compares CBMC simulations for unary CO_2 and N_2 isotherms at 298 K with the isotherm fits.

Figure S21b presents CBMC simulations of component loadings, q_i, for $CO_2(1)/N_2(2)$ mixture adsorption in CALF-20 at a total pressure of 100 kPa and 298 K; the mole fraction of $CO_2(1)$ in the bulk gas phase mixture, y_1, is varied from 0 to 1. The CBMC simulated loadings are in good agreement with the IAST estimations, indicated by the dashed lines. Figure S21c compares $CO_2(1)/N_2(2)$ adsorption selectivity from CBMC simulations with IAST estimates. The agreement is good, implying that none of the tenets demanded by the IAST are violated. The guest adsorbates are homogeneously distributed within the pore landscape, as is evident from the computational snapshot in Figure S22. In the experiments reported by Nguyen et al.[45] for $CO_2(1)/N_2(2)$ mixture adsorption in structured CALF-20 at 295 K, the experimental data for the N_2 loadings in their Figure S5 indicate small deviations from the IAST estimates. This deviation could be due to the fact that the mixture adsorption data of Nguyen et al.[45] are determined from breakthrough experiments that are not conducted under strict isothermal conditions.

Figure S23a presents CBMC simulations of component loadings, q_i, for $CO_2(1)/N_2(2)$ mixture adsorption in CALF-20 at 298 K with varying total fugacity f_t, maintaining the mole fraction of CO_2 in the bulk gas mixture at a constant value $y_2 = f_2/f_t = 0.05$. The dashed lines are the IAST estimations. We again note that the CBMC data for component loadings are in good agreement with the IAST estimates. Also, the CBMC simulations for $CO_2(1)/N_2(2)$ adsorption selectivity from CBMC simulations agree well with IAST estimates; see Figure S23b.

CBMC simulations were also conducted for N_2(1)/H_2O(2) mixtures in order to establish thermodynamic non-idealities, analogous to those observed earlier for CO_2(1)/H_2O(2) mixture adsorption in CALF-20 at 298 K.

Figure S24a presents the CBMC simulations for unary N_2(1), and H_2O(2) isotherms at 298 K. The unary fit parameters are provided in Table S5.

Figure S24b shows CBMC simulations of component loadings, q_i, for N_2(1)/H_2O(2) mixture adsorption in CALF-20 at 298 K at a total fugacity = 100 kPa. The mole fraction of H_2O in the bulk gas mixture, y_2, is varied. The loadings are plotted against $\%\text{Relative Humidity} = \frac{f_2}{p_2^{sat}} \times 100$ where f_2 is the partial fugacity of water in the bulk gas phase, and p_2^{sat} is the saturation vapor pressure of water. At 298 K, p_2^{sat} is determined from the Antoine equation: $p_2^{sat} = 3150$ Pa.

The dashed lines in Figure S24b are the IAST estimations; for this purpose the unary isotherm fits used are those provided in Table S5. We note that the N_2/H_2O binary mixture adsorption exhibits significant departures from thermodynamic idealities. Another way to demonstrate the non-idealities is to plot the mole fraction of N_2 in the adsorbed phase mixture, x_1, as a function of the $\%\text{Relative Humidity} = \frac{f_2}{p_2^{sat}} \times 100$; see Figure S24c. We note that for $\%\text{Relative Humidity} < 15\%$; $x_1 > 0.3$, the adsorbed phase mixture is richer in N_2, i.e. poorer in H_2O, than is anticipated by the IAST. On the other hand, for $\%\text{Relative Humidity} > 15\%$; $x_1 < 0.3$, the adsorbed phase mixture is poorer in N_2, i.e. richer in H_2O, than is anticipated by the IAST. These characteristics mirror those observed in Figure S15. The rationalization of the failure of the IAST is precisely analogous to those established for CO_2(1)/H_2O(2) mixture adsorption, established on the basis of RDFs, involving non-compliance with the tenets of the IAST.

The continuous solid lines are RAST calculations with fitted Margules parameters specified in Table S5.

Figure S25 shows computational snapshots showing the location of guest N_2 and H_2O in CALF-20 at 298 K. The total fugacity in the bulk gas phase is 100 kPa with partial fugacities f_1 = 99.985 kPa, and f_2 =0.015 kPa. The chosen conditions correspond to the scenario in Figure S24c with %Relative Humidity < 15%; $x_1 > 0.3$, i.e. the adsorbed phase mixture is richer in N_2 than is anticipated by the IAST.

Figure S26 shows Computational snapshots showing the location of guests N_2 and H_2O in CALF-20 at 298 K. The total fugacity in the bulk gas phase is 100 kPa with partial fugacities f_1 = 99.4 kPa, and f_2 =0.6 kPa. The chosen conditions to the scenario in Figure S24c with %Relative Humidity > 15%; $x_1 < 0.3$, i.e. the adsorbed phase mixture is poorer in N_2 than is anticipated by the IAST.

6.1 List of Tables for CBMC for CO2/N2 and N2/H2O Mixture Adsorption

Table S5. Dual-site Langmuir-Freundlich parameters for CO_2, H_2O, and N_2 determined from fitting unary isotherms determined at 298 K from CBMC simulations in CALF-20.

	Site A			Site B		
	$\frac{q_{A,sat}}{\text{mol kg}^{-1}}$	$\frac{b_A}{\text{Pa}^{-\nu_A}}$	ν_A	$\frac{q_{B,sat}}{\text{mol kg}^{-1}}$	$\frac{b_B}{\text{Pa}^{-\nu_B}}$	ν_B
CO_2 $R^2 = 0.999316$	1	4.693E-07	1	2.8	3.507E-04	1
H_2O $R^2 = 0.98238$	10.1	4.854E-29	10.5	1.3	1.888E-04	1.12
N_2 $R^2 = 0.999123$	2.8	2.849E-06	1			

Fitted Margules non-ideality parameters for binary N_2/H_2O mixture adsorption at 298 K in CALF-20.

	C / kg mol^{-1}	A_{12}	A_{21}
f_t = 100 kPa, vary y_2	0.155	8.874	2.948

6.2 List of Figures for CBMC for CO2/N2 and N2/H2O Mixture Adsorption

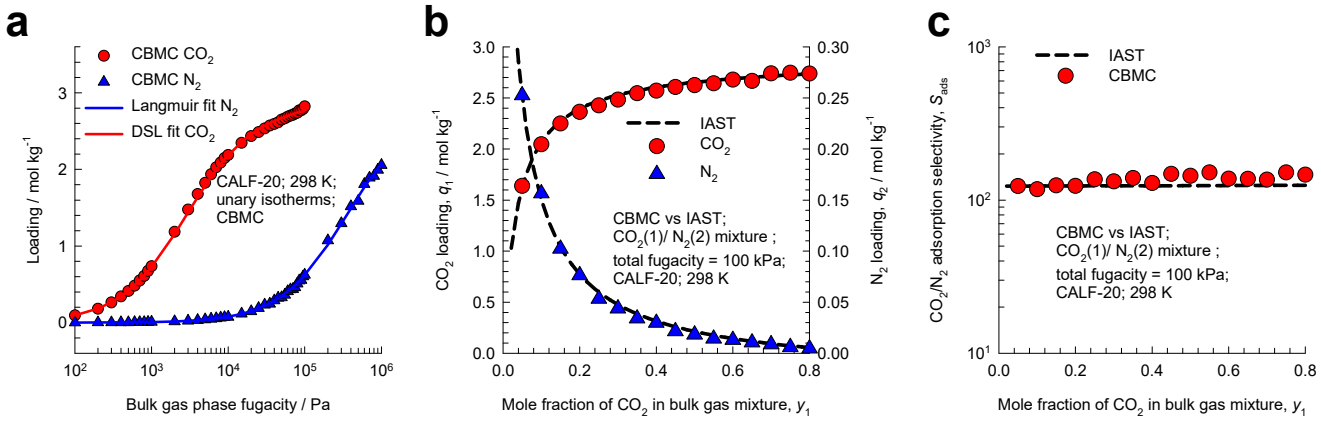

Figure S21. (a) CBMC simulations for unary CO_2 and N_2 isotherms at 298 K. The unary fit parameters are provided in Table S5. (b) CBMC simulations of component loadings, q_i, for $CO_2(1)/N_2(2)$ mixture adsorption in CALF-20 at a total pressure of 100 kPa and 298 K; the mole fraction of $CO_2(1)$ in the bulk gas phase mixture, y_1, is varied from 0 to 1. The dashed lines are the IAST estimations. (c) Plot of $CO_2(1)/N_2(2)$ adsorption selectivity from CBMC simulations with IAST estimates.

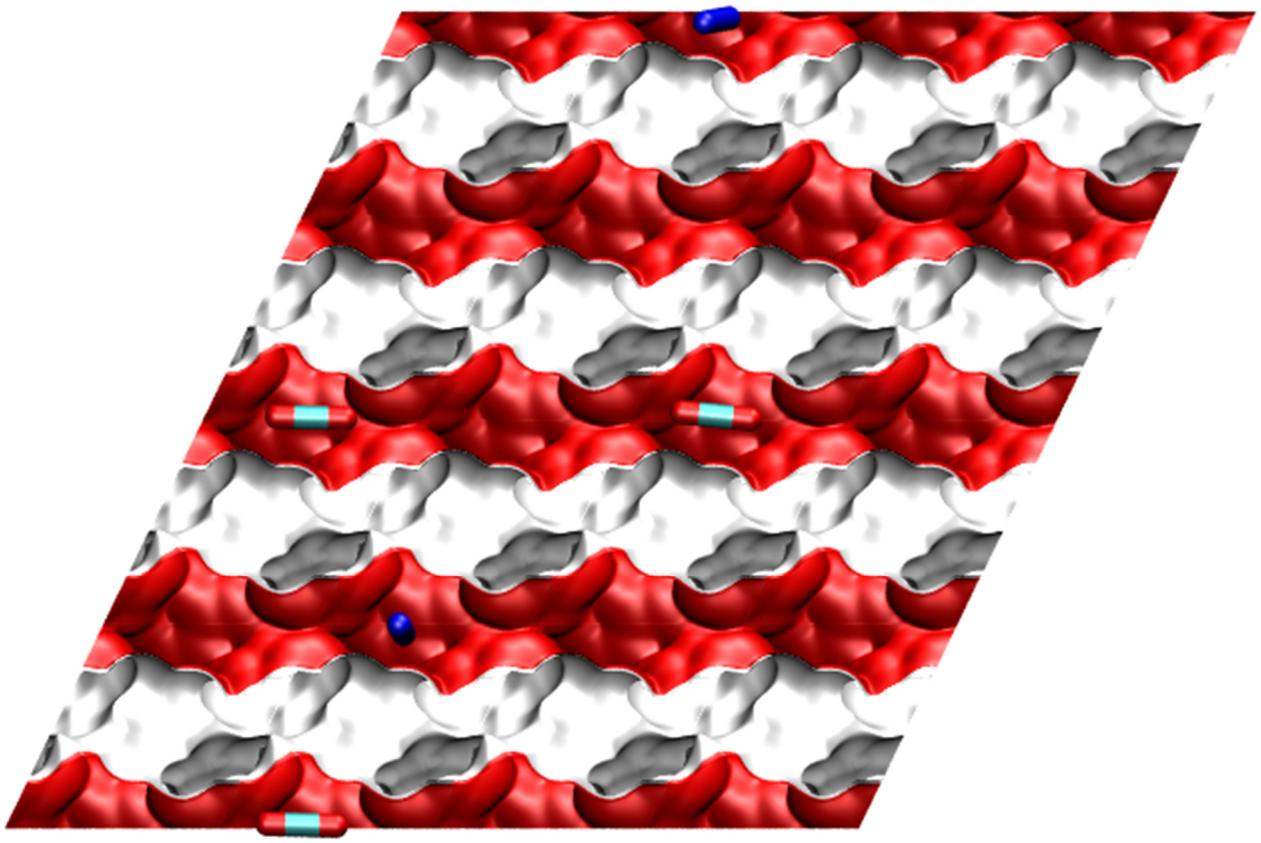

Figure S22. Computational snapshots showing the location of guest CO_2 and N_2 (blue pencil like molecule) in CALF-20 at 298 K. The total fugacity in the bulk gas phase is 100 kPa with partial fugacities f_1 = 5 kPa, and f_2 =95 kPa.

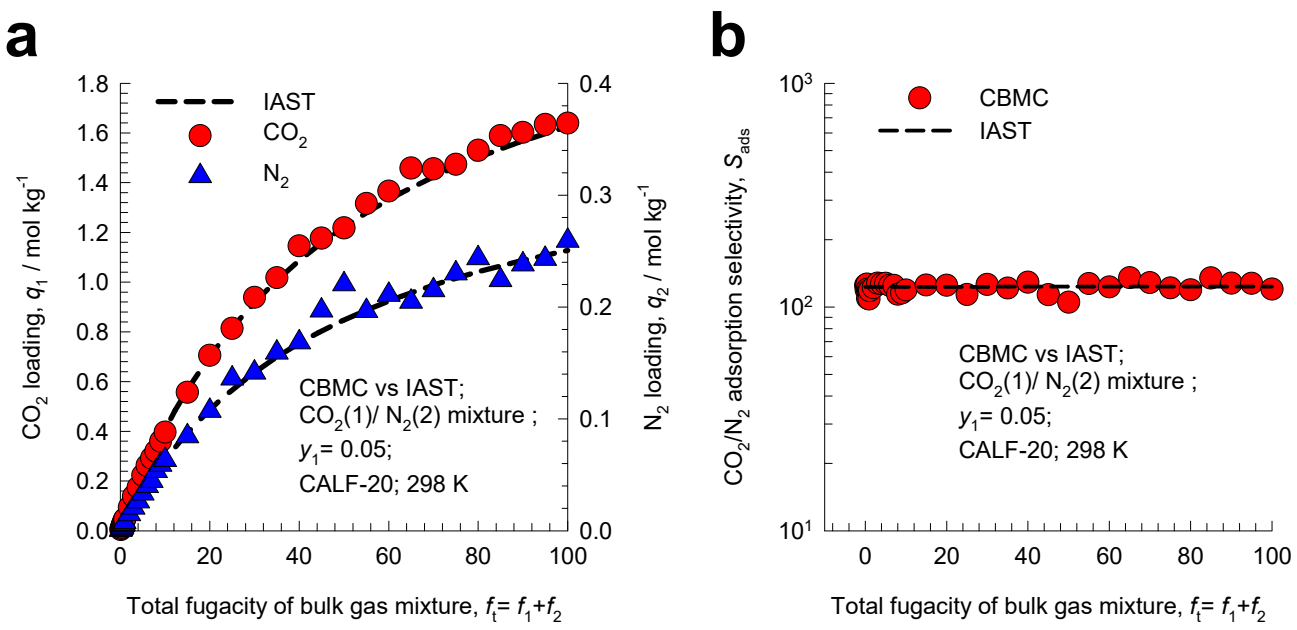

Figure S23. (a) CBMC simulations of component loadings, q_i, for CO2(1)/N2(2) mixture adsorption in CALF-20 at 298 K with varying total fugacity f_t, maintaining the mole fraction of CO2 in the bulk gas mixture at a constant value $y_2 = f_2/f_t = 0.05$. The dashed lines are the IAST estimations. (b) Plot of CO2(1)/N2(2) adsorption selectivity from CBMC simulations with IAST estimates.

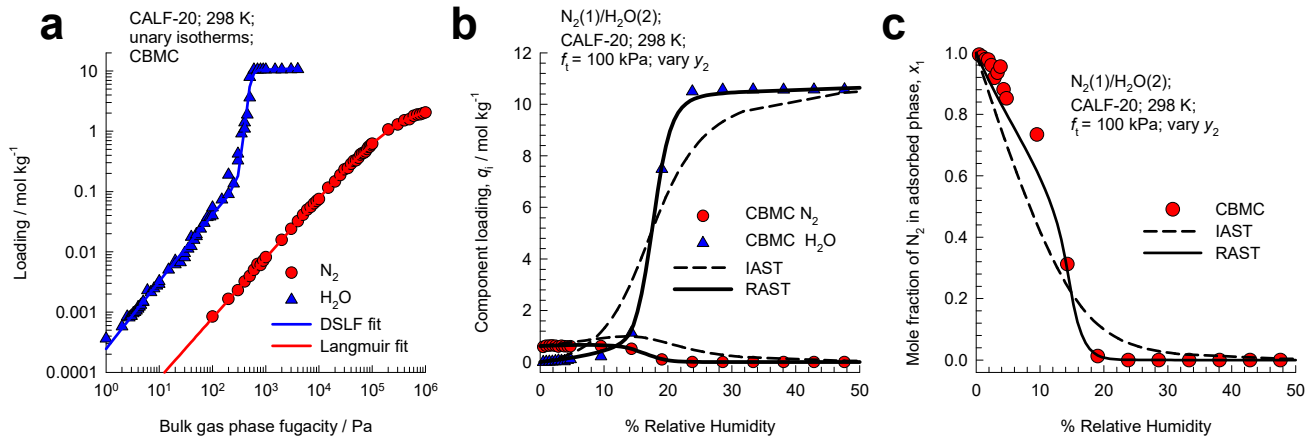

Figure S24. (a) CBMC simulations for unary $N_2(1)$, and $H_2O(2)$ isotherms at 298 K. The unary fit parameters are provided in Table S5. (b) CBMC simulations of component loadings, q_i, for $N_2(1)/H_2O(2)$ mixture adsorption in CALF-20 at 298 K at a total fugacity f_t = 100 kPa, plotted as a function of $\%\text{Relative Humidity} = \frac{f_2}{p_2^{sat}} \times 100$. The mole fraction of H_2O in the bulk gas mixture, $y_2 = f_2 / f_t$, is varied. (c) Plot of the mole fraction of CO_2 in the adsorbed phase mixture, x_1, as a function of the $\%\text{Relative Humidity} = \frac{f_2}{p_2^{sat}} \times 100$. The continuous solid lines are the RAST calculations using the Margules model for activity coefficients; the dashed lines are the IAST estimations.

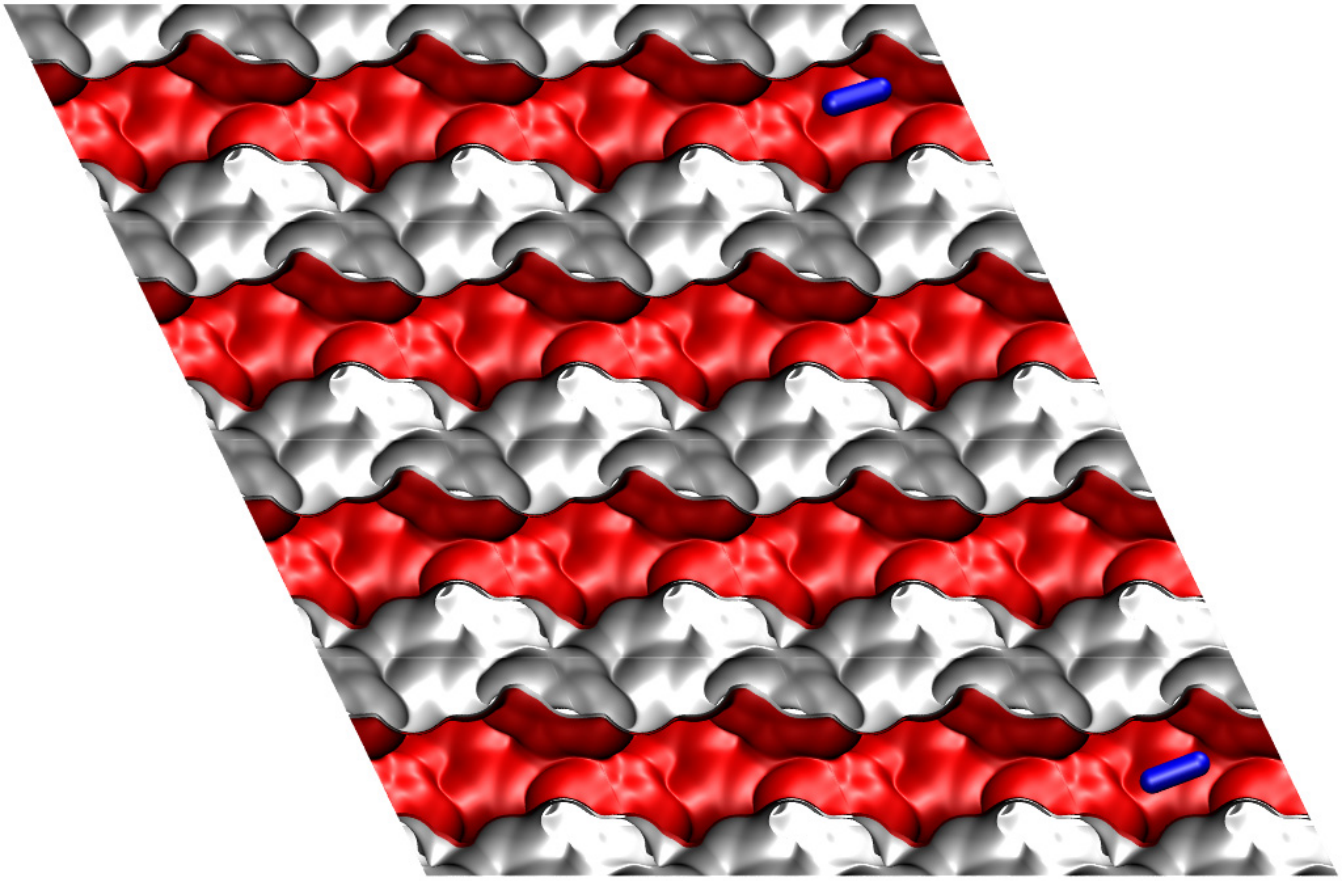

Figure S25. Computational snapshots showing the location of guest N_2 and H_2O in CALF-20 at 298 K. The total fugacity in the bulk gas phase is 100 kPa with partial fugacities f_1 = 99.985 kPa, and f_2 =0.015 kPa.

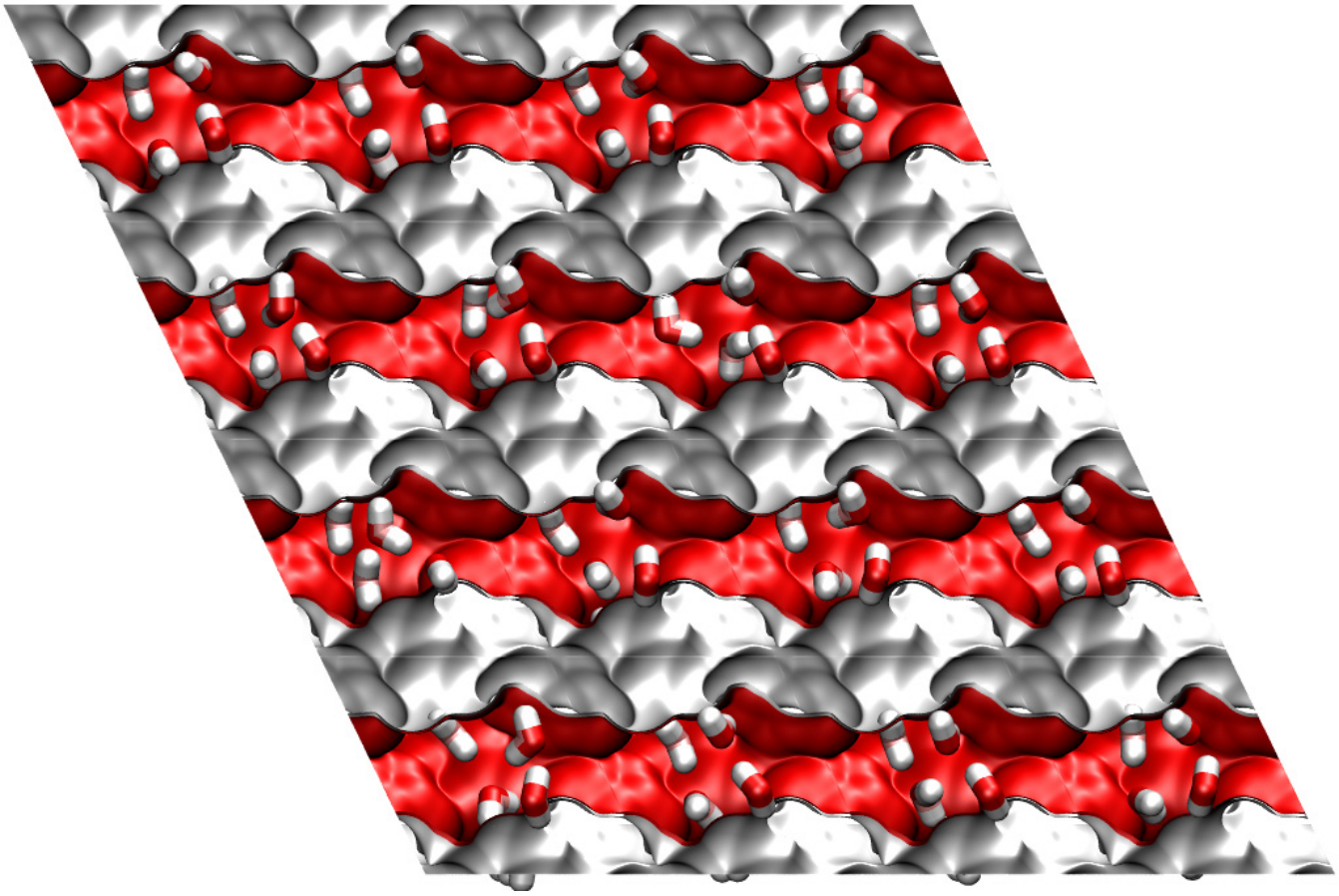

Figure S26. Computational snapshots showing the location of guest N_2 and H_2O in CALF-20 at 298 K. The total fugacity in the bulk gas phase is 100 kPa with partial fugacities f_1 = 99.4 kPa, and f_2 =0.6 kPa.

7 Nomenclature

Latin alphabet

A	surface area per kg of framework, $m^2\ kg^{-1}$
A_{12}, A_{21}	Margules parameters, dimensionless
b_i	Langmuir-Freundlich parameter, $Pa^{-\nu}$
c_i	molar concentration of species i, mol m^{-3}
c_{i0}	molar concentration of species i in fluid mixture at inlet to adsorber, mol m^{-3}
c_t	total molar concentration in mixture, mol m^{-3}
C	constant used in eq (S22), kg mol^{-1}
$Đ_i$	Maxwell-Stefan diffusivity for molecule-wall interaction, $m^2\ s^{-1}$
f_i	partial fugacity of species i, Pa
f_t	total fugacity of bulk phase mixture, Pa
L	length of packed bed adsorber, m
m_{ads}	mass of adsorbent in packed bed, kg
n	number of species in the mixture, dimensionless
N_i	molar flux of species i with respect to framework, mol $m^{-2}\ s^{-1}$
p_i	partial pressure of species i in mixture, Pa
p_t	total system pressure, Pa
p_2^{sat}	saturation vapor pressure of water, Pa
P_i^0	sorption pressure, Pa
q_i	component molar loading of species i, mol kg^{-1}
$q_{i,sat}$	molar loading of species i at saturation, mol kg^{-1}

q_t	total molar loading in mixture, mol kg^{-1}
$\bar{q}_i(t)$	spatial-averaged component uptake of species *i*, mol kg^{-1}
$q_{sat,mix}$	saturation capacity of mixture, mol kg^{-1}
Q_0	volumetric flow rate of gas mixture at inlet to fixed bed, m^3 s^{-1}
r	radial direction coordinate, m
r_c	radius of crystallite, m
R	gas constant, 8.314 J mol^{-1} K^{-1}
S_{ads}	adsorption selectivity, dimensionless
%RH	% relative humidity, dimensionless
t	time, s
T	absolute temperature, K
u	superficial gas velocity in packed bed, m s^{-1}
v	interstitial gas velocity in packed bed, m s^{-1}
x_i	mole fraction of species *i* in adsorbed phase, dimensionless
y_i	mole fraction of species *i* in the bulk fluid phase, dimensionless
z	distance along the adsorber, m

Greek alphabet

ε	voidage of packed bed, dimensionless
γ_i	activity coefficient of component *i* in adsorbed phase, dimensionless
Λ_{ij}	Wilson parameters, dimensionless
μ_i	molar chemical potential, J mol^{-1}
θ	fractional pore occupancy, dimensionless
ν	Freundlich exponent, dimensionless
π	spreading pressure, N m^{-1}

ρ	framework density, kg m^{-3}
τ	dimensionless time $\tau \equiv vt/L$, dimensionless
Φ	surface potential, mol kg^{-1}

Subscripts

i	referring to component *i*
t	referring to total mixture
sat	referring to saturation conditions
0	referring to conditions at inlet to fixed bed

8 References

(1) Ruthven, D. M. *Principles of Adsorption and Adsorption Processes*. John Wiley: New York, 1984; pp 1-433.

(2) Myers, A. L.; Prausnitz, J. M. Thermodynamics of Mixed Gas Adsorption. *A.I.Ch.E.J.* **1965**, *11*, 121-130. https://doi.org/10.1002/aic.690110125.

(3) Talu, O.; Myers, A. L. Rigorous Thermodynamic Treatment of Gas-Adsorption. *A.I.Ch.E.J.* **1988**, *34*, 1887-1893.

(4) Siperstein, F. R.; Myers, A. L. Mixed-Gas Adsorption. *A.I.Ch.E.J.* **2001**, *47*, 1141-1159.

(5) Krishna, R.; Van Baten, J. M. Elucidation of Selectivity Reversals for Binary Mixture Adsorption in Microporous Adsorbents. *ACS Omega* **2020**, *5*, 9031-9040. https://doi.org/10.1021/acsomega.0c01051.

(6) Krishna, R.; Van Baten, J. M. Using Molecular Simulations for Elucidation of Thermodynamic Non-Idealities in Adsorption of CO_2-containing Mixtures in NaX Zeolite. *ACS Omega* **2020**, *5*, 20535-20542. https://doi.org/10.1021/acsomega.0c02730.

(7) Krishna, R.; Van Baten, J. M. Water/Alcohol Mixture Adsorption in Hydrophobic Materials: Enhanced Water Ingress caused by Hydrogen Bonding. *ACS Omega* **2020**, *5*, 28393-28402. https://doi.org/10.1021/acsomega.0c04491.

(8) Krishna, R.; Van Baten, J. M. Investigating the Non-idealities in Adsorption of CO_2-bearing Mixtures in Cation-exchanged Zeolites. *Sep. Purif. Technol.* **2018**, *206*, 208-217. https://doi.org/10.1016/j.seppur.2018.06.009.

(9) Krishna, R.; van Baten, J. M. Fundamental Insights into the Variety of Factors that Influence Water/Alcohol Membrane Permeation Selectivity *J. Membr. Sci.* **2024**, *698*, 122635. https://doi.org/10.1016/j.memsci.2024.122635.

(10) Krishna, R.; Van Baten, J. M. How Reliable is the Ideal Adsorbed Solution Theory for Estimation of Mixture Separation Selectivities in Microporous Crystalline Adsorbents? *ACS Omega* **2021**, *6*, 15499–15513. https://doi.org/10.1021/acsomega.1c02136.

(11) Krishna, R.; van Baten, J. M. Hydrogen Bonding Effects in Adsorption of Water-alcohol Mixtures in Zeolites and the Consequences for the Characteristics of the Maxwell-Stefan Diffusivities. *Langmuir* **2010**, *26*, 10854-10867. https://doi.org/10.1021/la100737c.

(12) Krishna, R.; van Baten, J. M.; Baur, R. Highlighting the Origins and Consequences of Thermodynamic Nonidealities in Mixture Separations using Zeolites and Metal-Organic Frameworks. *Microporous Mesoporous Mater.* **2018**, *267*, 274-292. http://dx.doi.org/10.1016/j.micromeso.2018.03.013.

(13) Wilkins, N. S.; Rajendran, A. Measurement of competitive CO_2 and N_2 adsorption on Zeolite 13X for post-combustion CO_2 capture. *Adsorption* **2019**, *25*, 115-133. https://doi.org/10.1007/s10450-018-00004-2.

(14) Hefti, M.; Marx, D.; Joss, L.; Mazzotti, M. Adsorption Equilibrium of Binary Mixtures of Carbon Dioxide and Nitrogen on Zeolites ZSM-5 and 13X. *Microporous Mesoporous Mater.* **2015**, *215*, 215-228.

(15) van Zandvoort, I.; Ras, E.-J.; de Graaf, R.; Krishna, R. Using Transient Breakthrough Experiments for Screening of Adsorbents for Separation of C_2H_4/CO_2 Mixtures *Sep. Purif. Technol.* **2020**, *241*, 116706. https://doi.org/10.1016/j.seppur.2020.116706.

(16) van Zandvoort, I.; van der Waal, J. K.; Ras, E.-J.; de Graaf, R.; Krishna, R. Highlighting non-idealities in C_2H_4/CO_2 mixture adsorption in 5A zeolite. *Sep. Purif. Technol.* **2019**, *227*, 115730. https://doi.org/10.1016/j.seppur.2019.115730.

(17) Wang, Y.; LeVan, M. D. Adsorption Equilibrium of Binary Mixtures of Carbon Dioxide and Water Vapor on Zeolites 5A and 13X. *J. Chem. Eng. Data* **2010**, *55*, 3189-3195. https://doi.org/10.1021/je100053g.

(18) Lin, J.-B.; Nguyen, T. T. T.; Vaidhyanathan, R.; Burner, J.; Taylor, J. M.; Durekova, H.; Akhtar, F.; Mah, R. K.; Ghaffari-Nik, O.; Marx, S.; Fylstra, N.; Iremonger, S. S.; Dawson, K. W.; Sarkar, P.; Hovington, P.; Rajendran, A.; Woo, T. K.; Shimizu, G. K. H. A scalable metal-organic framework as a durable physisorbent for carbon dioxide capture. *Science* **2021**, *374*, 1464-1469. https://www.science.org/doi/abs/10.1126/science.abi7281.

(19) Kaur, H.; Marshall, B. D. Real adsorbed solution theory model for the adsorption of CO_2 from humid gas on CALF-20. *ChemRxiv* **2023**, 1-18. https://doi.org/10.26434/chemrxiv-2023-2cp2c.

(20) Nguyen, T. T. T. *Humid Post-Combustion CO_2 capture By Vacuum Swing Adsorption Using CALF-20*. Ph.D. Thesis, University of Alberta, Alberta, 2021. https://era.library.ualberta.ca/items/a5615f1a-b04a-453f-bfad-2a3776b5dd24.

(21) Nguyen, T. T. T.; Balasubramaniam, B. M.; Fylstra, N.; Huynh, R. P. S.; Shimizu, G. K. H.; Rajendran, A. Competitive CO_2/H_2O Adsorption on CALF-20. *Ind. Eng. Chem. Res.* **2024**, *63*, 3265-3281. https://doi.org/10.1021/acs.iecr.3c04266.

(22) Gopalsamy, K.; Fan, D.; S., N.; Magnin, Y.; Maurin, G. Engineering of an Iso-Reticular Series of CALF-20 MOF for CO_2 Capture. *ACS Appl. Eng. Mater.* **2024**, *2*, 96-103. https://doi.org/10.1021/acsaenm.3c00622.

(23) Krishna, R.; van Baten, J. M. In silico screening of metal-organic frameworks in separation applications. *Phys. Chem. Chem. Phys.* **2011**, *13*, 10593-10616. https://doi.org/10.1039/C1CP20282K.

(24) Krishna, R.; van Baten, J. M. In Silico Screening of Zeolite Membranes for CO_2 Capture. *J. Membr. Sci.* **2010**, *360*, 323-333. https://doi.org/10.1016/j.memsci.2010.05.032.

(25) Krishna, R.; van Baten, J. M. Describing Mixture Diffusion in Microporous Materials under Conditions of Pore Saturation. *J. Phys. Chem. C* **2010**, *114*, 11557-11563.

(26) Krishna, R.; van Baten, J. M. Diffusion of alkane mixtures in zeolites. Validating the Maxwell-Stefan formulation using MD simulations. *J. Phys. Chem. B* **2005**, *109*, 6386-6396.

(27) Krishna, R.; van Baten, J. M. Insights into diffusion of gases in zeolites gained from molecular dynamics simulations. *Microporous Mesoporous Mater.* **2008**, *109*, 91-108.

(28) Krishna, R. Describing the Diffusion of Guest Molecules inside Porous Structures. *J. Phys. Chem. C* **2009**, *113*, 19756-19781. https://doi.org/10.1021/jp906879d.

(29) Krishna, R. Diffusion in Porous Crystalline Materials. *Chem. Soc. Rev.* **2012**, *41*, 3099-3118. https://doi.org/10.1039/C2CS15284C.

(30) Oktavian, R.; Goeminne, R.; Glasby, L. T.; Song, P.; Huynh, R.; Qazvini, O. T.; Ghaffari-Nik, O.; Masoumifard, N.; Cordiner, J. L.; Hovington, P.; Van Speybroeck, V.; Moghadam, P. Z. Gas adsorption and framework flexibility of CALF-20 explored via experiments and simulations. *Nat. Commun.* **2024**, *15*, 3898. https://doi.org/10.1038/s41467-024-48136-0.

(31) Mayo, S. L.; Olafson, B. D.; Goddard, W. A. DREIDING: A Generic Force Field for Molecular Simulations. *J. Phys. Chem.* **1990**, *94*, 8897-8909.

(32) García-Sánchez, A.; Ania, C. O.; Parra, J. B.; Dubbeldam, D.; Vlugt, T. J. H.; Krishna, R.; Calero, S. Development of a Transferable Force Field for Carbon Dioxide Adsorption in Zeolites. *J. Phys. Chem. C* **2009**, *113*, 8814-8820. https://doi.org/10.1021/jp810871f.

(33) Horn, H. W.; Swope, W. C.; Pitera, J. W.; Madura, J. D.; Dick, T. J.; Hura, G. L.; Head-Gordon, T. Development of an improved four-site water model for biomolecular simulations: TIP4P-Ew. *J. Chem. Phys.* **2004**, *120*, 9665-9578. https://doi.org/10.1063/1.1683075.

(34) Krishna, R.; Van Baten, J. M. Highlighting the Anti-Synergy between Adsorption and Diffusion in Cation-Exchanged Faujasite Zeolites. *ACS Omega* **2022**, *7*, 13050-13056. https://doi.org/10.1021/acsomega.2c00427.

(35) Zhang, C.; Yang, X. Molecular dynamics simulation of ethanol/water mixtures for structure and diffusion properties. *Fluid Phase Equilib.* **2005**, *231*, 1-10.

(36) Talu, O.; Zwiebel, I. Multicomponent Adsorption Equilibria of Nonideal Mixtures. *A.I.Ch.E.J.* **1986**, *32*, 1263-1276.

(37) Sochard, S.; Fernandes, N.; Reneaume, J.-M. Modeling of Adsorption Isotherm of a Binary Mixture with Real Adsorbed Solution Theory and Nonrandom Two-Liquid Model. *A.I.Ch.E.J.* **2010**, *56*, 3109-3119.

(38) Mittal, N.; Bai, P.; Siepmann, I.; Daoutidis, P.; Tsapatsis, M. Bioethanol Enrichment using Zeolite Membranes: Molecular Modeling, Conceptual Process Design and Techno-Economic Analysis. *J. Membr. Sci.* **2017**, *540*, 464-476.

(39) Calleja, G.; Jimenez, A.; Pau, J.; Domínguez, L.; Pérez, P. Multicomponent Adsorption Equilibrium of Ethylene, Propane, Propylene and CO_2 on 13X Zeolite. *Gas Sep. Purif.* **1994**, *8*, 247-256.

(40) Krishna, R. Highlighting the Influence of Thermodynamic Coupling on Kinetic Separations with Microporous Crystalline Materials. *ACS Omega* **2019**, *4*, 3409-3419. https://doi.org/10.1021/acsomega.8b03480.

(41) Krishna, R. Metrics for Evaluation and Screening of Metal-Organic Frameworks for Applications in Mixture Separations. *ACS Omega* **2020**, *5*, 16987−17004. https://doi.org/10.1021/acsomega.0c02218.

(42) Krishna, R. Synergistic and Antisynergistic Intracrystalline Diffusional Influences on Mixture Separations in Fixed Bed Adsorbers. *Precision Chemistry* **2023**, *1*, 83-93. https://doi.org/10.1021/prechem.2c00003.

(43) Krishna, R. Fundamental Insights into Intra-Crystalline Diffusional Influences on Mixture Separations in Fixed Bed Adsorbers. *Chem Bio Eng.* **2024**, *1*, 53-66. https://doi.org/10.1021/cbe.3c00057.

(44) Krishna, R. Occupancy Dependency of Maxwell−Stefan Diffusivities in Ordered Crystalline Microporous Materials. *ACS Omega* **2018**, *3*, 15743-15753. https://doi.org/10.1021/acsomega.8b02465.

(45) Nguyen, T. T. T.; Lin, J.-B.; Shimizu, G. K. H.; Rajendran, A. Separation of CO_2 and N_2 on a hydrophobic metal organic framework CALF-20. *Chem. Eng. J.* **2022**, *442*, 136263. https://doi.org/10.1016/j.cej.2022.136263.